

Sol-gel and nano-suspension electrolyte layers for high performance solid oxide fuel cells

Feng Han



Forschungszentrum Jülich GmbH Institute of energy and climate research (IEK) Materials Synthesis and Processing (IEK-1)

Sol-gel and nano-suspension electrolyte layers for high performance solid oxide fuel cells

Feng Han

Schriften des Forschungszentrums Jülich Reihe Energie & Umwelt / Energy & Environment Bibliographic information published by the Deutsche Nationalbibliothek. The Deutsche Nationalbibliothek lists this publication in the Deutsche Nationalbibliografie; detailed bibliographic data are available in the Internet at http://dnb.d-nb.de.

Publisher and Forschungszentrum Jülich GmbH

Distributor: Zentralbibliothek

52425 Jülich

Phone +49 (0) 24 61 61-53 68 · Fax +49 (0) 24 61 61-61 03

e-mail: zb-publikation@fz-juelich.de Internet: http://www.fz-juelich.de/zb

Cover Design: Grafische Medien, Forschungszentrum Jülich GmbH

Printer: Grafische Medien, Forschungszentrum Jülich GmbH

Copyright: Forschungszentrum Jülich 2011

Schriften des Forschungszentrums Jülich

Reihe Energie & Umwelt / Energy & Environment Band / Volume 100

D 294 (Diss., Bochum, Univ., 2010)

ISSN 1866-1793 ISBN 978-3-89336-694-1

Neither this book nor any part of it may be reproduced or transmitted in any form or by any means, electronic or mechanical, including photocopying, microfilming, and recording, or by any information storage and retrieval system, without permission in writing from the publisher.

Kurzfassung

Festelektrolyt-Brennstoffzellen (SOFC) werden als eine der effizientesten und umweltfreundlichsten Einheiten zur Direktumsetzung von chemischer Energie in Elektrizität betrachtet. Für die Kommerzialisierung von SOFCs müssen sowohl die Langzeitstabilität als auch die Systemzuverlässigkeit gewährleistet werden sowie die Herstellungskosten reduziert werden. Dies kann durch die Verringerung der Betriebstemperatur auf 650 °C bei gleichzeitiger Beibehaltung einer angemessenen Leistungsabgabe des Systems realisiert werden.

In Rahmen dieser Arbeit wurden kostengünstige nasschemische Fertigungstechniken zur Herstellung von dünnen, gasdichten Elektrolytschichten für Hochleistungsbrennstoffzellen eingesetzt. Der Fokus dieser Arbeit ist dreigeteilt: (1) Herstellung von feinpartikulären Solen mit nanoskaliger Partikelgrößenverteilung und exzellenten Schichtbildungseigenschaften, (2) Beschichtung von dünnen, gasdichten Elektrolytschichten mit einer Dicke von ca. 1 μm und einer geringen Heliumleckrate von unter 2.0x10⁻⁵ (hPa·dm³)/(s·cm²), (3) Herstellung und Charakterisierung von SOFCs mit hoher elektrochemischer Leistung.

Die hergestellten Einzelzellen mit dünnen, gasdichten Elektrolytschichten zeigten exzellente elektrochemische Kenndaten. Bei einer Zellspannung von 0,7 V erreichten die Zellen hohe Stromdichten von über 3 A/cm², 1.5 A/cm² and 1.0 A/cm² bei jeweils 800 °C, 650 °C and 600 °C und stellen somit SOFCs mit den höchsten bisher in der Literatur berichteten Leistungsdichten dar. Bei Untersuchung mittels elektrochemischer Impedanzspektroskopie liegt der spezifische Flächenwiderstand einer Einzelzelle um mehr als 80 % niederiger als die vom Forschungszentrum Jülich hergestellten Zellen mit den herkömmlich 10 μm dicken Elektrolyten.

Aufgrund der exzellenten Performance wird eine verbesserte Lebensdauer und Stabilität der SOFCs durch den Betrieb der Zellen bei reduzierten Temperaturen (650 °C bis 700 °C) und höherer Zellspannung erwartet. Die Herstellungskosten des SOFC-Systems können zusätzlich effektiv reduziert werden.

Abstract

Solid oxide fuel cell (SOFC) is regarded as one of the most efficient and environmental-friendly devices for direct conversion of chemical energy into electricity. For commercialization of SOFCs, the long-term stability and as well as reliability of the system have to be guaranteed, and the manufacturing cost has to be reduced. This can be realized by reducing the operation temperature down to 650 °C, while maintaining adequate system power output.

In this work, low-cost wet-chemical processing techniques have been applied to fabricate thin gas-tight electrolyte layers for high performance SOFC applications. The focus of this work is threefold: (1) to prepare sols with nano-scaled particle size distribution and excellent layer formation properties, (2) to deposit thin gas-tight electrolyte with thickness of about 1 μ m and a rather low helium leak rate under $2.0 \times 10^{-5} \, (h \, Pa \cdot dm^3)/(s \cdot cm^2)$, (3) to manufacture and characterize SOFCs with high electrochemical performance.

The as-prepared single cells with thin gas-tight electrolyte layers showed excellent electrochemical performance. At a cell voltage of 0.7 V, the cells reached high current densities of more than 3 A/cm^2 , 1.5 A/cm^2 and 1.0 A/cm^2 at $800 \,^{\circ}\text{C}$, $650 \,^{\circ}\text{C}$ and $600 \,^{\circ}\text{C}$, respectively, which are the SOFCs with the highest power density ever since reported. According to the electrochemical impedance spectroscopy investigation, the area specific ohmic resistances of the single cells are more than 80% lower than the cells with conventional $10 \, \mu \text{m}$ thick electrolytes manufactured by Forschungszentrum Jülich.

Due to the excellent performance, the life time and stability of the SOFCs is expected to be improved by operating the cells at reduced temperature (650 °C to 700 °C) and increased cell voltage. Additionally, the manufacturing cost of the SOFC system can be effectively reduced.

Content

1	Intro	oduction	1
	1.1	Economic and ecologic demand for electricity	
	1.2	Aims of SOFC research and development	1
	1.3	Objectives of this work and outline	
2	Fun	damentals and background	
_			_
	2.1	Fuel cells	3
	2.1.1	Different types of fuel cells	4
	2.1.2	Operation principle of SOFC	6
	2.1.3 2.1.4	Thermodynamics Electrochemical efficiency of SOFC Flectrolytes	
	2.1.4	Electrochemical efficiency of SOFC	8 11
	2.1.5	Dietarof tes	11 14
	2.1.0	Anodes Cathodes	14
	2.1.8	CathodesCell design	15
	2.2	Sol-gel processing	
	2.2.1	Colloidal particle system	18
	2.2.2	Polymeric and colloidal sols	20
	2.2.3	Spin-coating	22
	2.2.4	Dip-coating	23
	2.2.5	Sintering of thin ceramic layers	25
3	Exp	erimental	27
	3.1	Electrolyte preparation strategies	27
	3.2	Synthesis and sample preparations	27
	3.2.1	A two-step polymeric zirconia sol-gel process	27
	3.2.2	Synthesis of colloidal sol	28
	3.2.3	Preparation of commercial colloidal zirconia and ceria nano-suspension	29
	3.2.4	Synthesis of CGO, LSM and LSFC polymeric sols from inorganic metal salts	29
	3.2.5	Preparation of powders	30
	3.2.6	Preparation of substrate and anode	30
	3.2.7	Preparation of YSZ electrolyte layer	31
	3.2.8	Preparation of CGO barrier layer	32
	3.2.9	Preparation of cathode	32
	3.3	Characterizations	32
	3.3.1	Particle size distribution	32
	3.3.2	Adsorption	33
	3.3.3	Surface topography and deflection measurement	33
	3.3.4	Dilatometry	33
	3.3.5	Helium leak rate test	34
	3.3.6	X-ray diffraction (XRD)	34
	3.3.7	SEM and TEM	34
	3.3.8	Electrochemical impedance spectroscopy (EIS)	
	3.3.9	Electrochemical single cell test	37
4	Resi	ults and discussion	38
	4.1	Fundamental characterization of materials	38
	4.1.1	YSZ polymeric sols and derived powders	38
	4.1.2	CGO, LSM and LSCF polymeric sols and derived powders	45
	112	9VS7 colloidal sals and derived newdors	

i

Content

	4.1.4	Nano-suspensions made of commercial oxide particles	51
	4.1.5	Results of dilatometric measurements	56
4	.2	Characterization of layers	58
	4.2.1	Substrates	58
	4.2.2	Layers deposited with polymeric sols	60
	4.2.3	Layers deposited with nano-suspensions	64
4	.3	Electrochemical characterization of single cells	78
	4.3.1		LSCF
	cathod	e (Group 1-1)	80
	4.3.2	e (Group 1-1)	e
	(Group	2-1 and Group 2-2)	83
	4.3.3		
	(Group	3-1, Group 3-2 and Group 3-3)	92
	4.3.4	Electrochemical impedance spectroscopy (EIS)	106
		Single cells with co-sintered multi-layered electrolyte, CGO layer and LSC catho	
	(Group	94-1)	112
	4.3.6		118
5	Sumn	nary	121
6		rences	123
7	Ackn	owledgements	129

List of abbreviations

AFC Alkaline fuel cell

AFL Anode functional layer
APU Auxiliary power unit
ASC Anode-supported cells
ASR Area specific resistance

ASQ Area specific heat dissipation rate

BSE Back-scattered electrons

Cermet Ceramic-metal

CGO Gadolinium doped ceria
CHP Combined heat and power

CNLS Complex nonlinear least-squares
CTE Coefficient of thermal expansion

DEA Diethonolamine

DMFC Direct methanol fuel cell

DRTs Distribution function of relaxation times

ECC Electrochemical single cell test

EDX Energy dispersive X-rays scattering

EIS Electrochemical Impedance spectroscopy

ESC Electrolyte-supported cells
FFT Fast Fourier transform

FG02 Tape-cast substrate without pore-former
FG31 Tape-cast substrate with pore-former
FZJ Forschungszentrum Jülich GmbH
IEF Institute of Energy Research

IFF Institute of Solid State Research

IWE Institute of Materials for Electrical and Electronic Engineering

i-V curve Curve of current density plotted over cell voltage

KIT Karlsruhe Institute of Technology
LSC Lanthanum strontium cobaltite
LSCF Lanthanum strontium cobalt ferrite
LSGM Mg²⁺ substituted lanthanum gallate

List of abbreciations

LSM Lanthanum strontium manganite

MCFC Molten carbonate fuel cell
OCV Open circuit voltage
PAFC Phosphoric acid fuel cell

PEMFC Proton exchange membrane / Polymer electrolyte membrane fuel cell

PSD Particle size distribution

PVA Polyvinyl alcohol

RCF Relative centrifugal force

RT Room temperature

SCCM Standard cubic centimeters per minute

ScSZ Scandia-stabilized zirconia

SE Secondary electrons

SEM Scanning electron microscopy

SOFC Solid oxide fuel cell

TEM Transmission electron microscopy

TPB Triple phase boundary
XRD X-rays diffractometry

8YSZ 8 mol% yttria stabilized zirconia 3YSZ 3 mol% yttria stabilized zirconia

1 Introduction

1.1 Economic and ecologic demand for electricity

Since 1980s, environment and energy issues have become worldwide concerned topics. As more and more populated developing countries industrialized, the demand for electricity generation capacity has been remarkably increasing. Fuel cells as energy conversion systems with high efficiency and low gas emissions, such as CO₂, CO, SO₂ and NO_x, are promising clean energy solutions. Among all types of fuel cells, solid oxide fuel cells are receiving significant attention as alternative way for stationary power generation systems, auxiliary power units (APU) for mobile application [1-3] and micro SOFCs [4] as battery replacement.

1.2 Aims of SOFC research and development

The important aims of SOFC development are to improve efficiency, realize long-term stability and reduce manufacturing cost in order to realize a successful commercialization. The reduction of operating temperature is believed to be one of the most promising approaches to fulfill these goals. Furthermore, the reduction of the operating temperature can also bring many other advantages, including the reduction of material requirements and simplification of the sealing of the SOFC system. As disadvantages, the operating temperature reduction decrease the thermally activated transport processes leading to an increase in ohmic and electrode polarization losses [5]. When using hydrocarbon fuels, a significant carbon deposition on the anode and a delamination of anode may occur at low operation temperature [6-10].

The main approach to reduce the operating temperature is to increase the power density by developing more efficient electrolyte and catalytically effective electrodes [11, 12]. Thin-film electrolytes, typically 10 µm thick, in anode-supported cells (ASC) can substantially reduce the ohmic losses in comparison to electrolyte-supported cells (ESC). Additionally, new materials with high oxygen-diffusion properties and

1

electrolytes with tailored microstructures provide further possibilities to enhance the efficiency and performance of the SOFCs.

1.3 Objectives of this work and outline

The aim of this work is to develop thin-film electrolyte layers for high performance SOFCs, which are suitable for the operation at temperatures below 700 °C, via low-cost wet-chemical processing techniques. By reducing the thickness of the gas-tight electrolyte to less than 2 μm, the power output of the single cells with active cathode size of 4x4 cm² could reach 1.5 A/cm² or 1 W/cm² at a cell voltage of 0.7 V and operating temperature of 650 °C. The success of this work could lead to manufacturing of SOFCs with high efficiency and low degradation. The cost efficient wet-chemical coating techniques, such as dip-coating method, can also ensure the low manufacturing cost for the electrolyte.

The fundamentals of the fuel cells technology and sol-gel science are reviewed in chapter 2. The processing as well as the characterization of the nano-scaled materials and layers is described in chapter 3. The results of the performed experiments, especially the electrochemical performance of the as-prepared single cells, are presented and discussed in detail in chapter 4. Finally, a brief summary of this work is given in chapter 5.

2 Fundamentals and background

2.1 Fuel cells

Fuel cells are electrochemical conversion devices generating electricity through chemical reaction without any thermal-mechanical step. The buildup of fuel cells is similar to the build-up of batteries, normally consisting of an ionic conductive electrolyte separating two electrical conductive electrodes, i.e. the anode and the cathode. Different from the batteries as energy storage device, the fuel cells are supplied continuously with fuels, such as hydrogen, methane or natural gas, and oxidants, for example air during the operation. In the presence of an electrolyte, the fuels on the anode side react with the oxidant on the cathode side producing electricity. This process is also recognized as the reverse reaction of electrolysis. As long as the necessary fuel and oxidant flows are maintained, fuel cells can generate electricity continuously.

Fuel cells are also considered as environmental-friendly energy solution thank to their high efficiency and low emissions. The efficiency of electricity generation by heat engines through combustion fossil fuel is limited by the Carnot cycle, which describes the thermodynamic processes occurring during the expansion of a gas in order to do work [13]. Direct conversion of fuel energy into electricity is the key characteristic of fuel cell operation. The fuel cells do not operate on a thermal cycle and directly convert the chemical energy into electrical energy through chemical reaction without any thermal-mechanical steps, therefore, they are not restricted by Carnot efficiency limitations, and their electrical efficiency in converting chemical energy to electrical energy can be significantly enhanced. The higher operating temperature make SOFCs suitable candidates for application with heat engine energy recovery devices or combined heat and power (CHP) systems, which further increases overall fuel efficiency to over 70% [14, 15].

2.1.1 Different types of fuel cells

Since the principle of the fuel cell had been demonstrated by Sir William Grove in 1839 [16], many investigators had investigated and experimented with various types of fuel cells. As listed in Table 2.1, the fuels cells are classified by the applied electrolytes, which also determine the operation temperature, material choice, efficiency and application of the fuel cells. The different fuel cell types with information about operation temperature, fuel and oxidation gases, as well as conductive ions are schematically demonstrated in Figure 2.1.

Fuel Cell Type	Abbr.	Electrolyte	Operating
			Temperature
Solid oxide fuel cell	SOFC	O ₂ /H ₂ -conducting ceramic oxide	650-1100 °C
Molten carbonate fuel cell	MCFC	Molten alkaline carbonate	600-650 °C
Phosphoric acid fuel cell	PAFC	Molten phosphoric acid (H ₃ PO ₄)	150-200 °C
Direct methanol fuel cell	DMFC	Polymer membrane	90-120 °C
Proton exchange membrane fuel cell	PEMFC	Polymer membrane	50-220 °C
Alkaline fuel cell	AFC	Aqueous alkaline solution	<80 °C

Table 2.1 Types of fuel cells

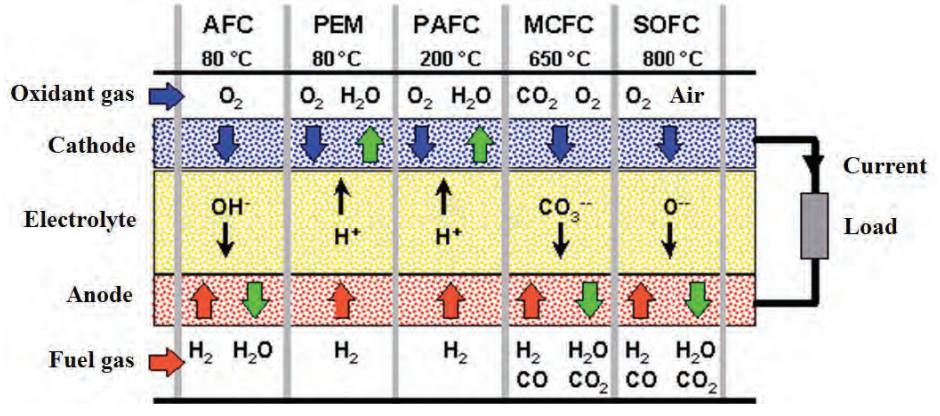


Figure 2.1 Schematic demonstration of different fuel cell types

Alkaline fuel cells (AFC) have been used to provide electrical power for Apollo spacecraft Shuttles and drinking water for the astronauts since the 1960s by NASA. AFCs operate on compressed hydrogen and oxygen and generally use a aqueous solution of potassium hydroxide retained in a porous stabilized matrix as their electrolyte, generating electricity with efficiency of approximately 70% [17]. The

concentration of KOH can be varied with the fuel cell operating temperature, which ranges from 65 to 220 °C with cell output ranges from 300 W to 5 kW. They require pure hydrogen fuel to avoid expensive platinum electrode catalysts from poisoning. Possible leak of potassium hydroxide solution is another disadvantage of AFCs [18].

Proton Exchange Membrane fuel cells (PEMFC) are operated with a permeable proton-conducting polymer membrane deposited with a platinum catalyst as electrolyte. The efficiency of PEMFC is about 40-50% with a power output up to 250 kW. The oxidant and fuel gases with high purity are needed for the operation of the cells to avoid platinum catalysts from poisoning. Since platinum catalyst is used on both sides of the membrane, the fabrication cost of PEMFC is relatively high. As advantages, the solid flexible polymer membrane electrolytes do not crack and operate at low temperature. The water management and poisoning of the catalyst by carbon monoxide are the main issues to be solved [19, 20].

Phosphoric Acid Fuel Cells (PAFC) use liquid phosphoric acid (H₃PO₄) as an electrolyte and operate in the temperature range of 150 to 200 °C with electricity generating efficiency of around 40% or with a combined heat and power (CHP) efficiency as high as 85%. Although the PAFC systems have demonstrated impressive reliability and satisfied performance, the commercialization in the distributed CHP market has been restrained by high production cost and harsh operation conditions of the acid electrolyte [21-24].

Molten Carbonate Fuel Cells (MCFC) operate at high-temperature (600~650 °C) using electrolytes composed of a molten carbonate salt mixture suspended in a porous, chemically inert ceramic matrix. One of the most important advantages of MCFCs is the insensitivity to fuel impurities due to high operating temperatures. Methane can be internally converted to hydrogen and used as fuel [25]. The disadvantage of MCFCs is the relative short cell life time resulting from the highly corrosive operation media [26]. Combined to a steam turbine, MCFCs can reach overall efficiencies approaching 60% and power output up to 100 MW [27].

Solid oxide fuel cells (SOFC) are characterized by operating on gas-tight proton or oxygen ionic conductive ceramic electrolytes[28, 29]. High temperatures over 600 °C

are required for SOFC operations in order to achieve efficient catalytic activation of the electrodes and sufficient ionic conductivity of the electrolyte. Advantages of SOFCs include compatibility to hydrocarbon fuels, high efficiency and long-term stability. The electrical efficiency of SOFC systems can reach 50-60%. The high operating temperature is the main disadvantage of SOFCs, which results in longer start-up time, mechanical and chemical compatibility issues [24, 30].

2.1.2 Operation principle of SOFC

In the operation of a SOFC, the electricity generation mechanism is based on two electrochemical reactions separated at the anode and cathode. It produces electricity and heat from fuel and an oxidant which react in the presence of an electrolyte. At the operation temperature, the electrochemical transformation of the reactants in the SOFC is directly activated by the available Gibbs free enthalpy in the fuel.

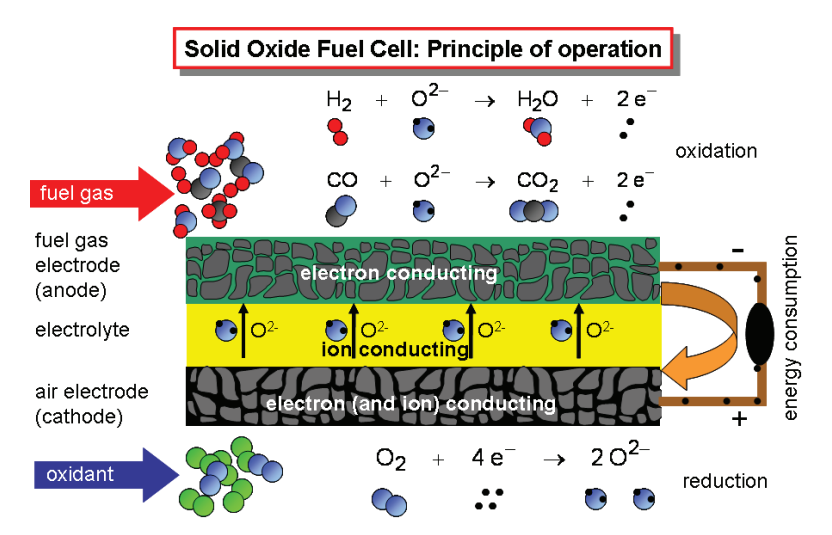


Figure 2.2 Schematic of solid oxide fuel cell (L.G.J. de Haart, IEF-3, Forschungszentrum Jülich)

As shown in Figure 2.2, a SOFC contains a solid electrolyte layer made from ceramic compounds such as yttria-stabilized zirconia (YSZ) which functions as a conductor of oxide ions at temperature higher than 600 °C. This ceramic layer allows oxygen atoms to be reduced at the cathode/electrolyte interface by electrons, forming oxide ions, which are then transported through the ceramic electrolyte layer to the fuel-rich porous anode where the oxide ions reacts with the fuel gas, such as hydrogen or

carbon monoxide. A SOFC are normally consisted of five components providing electrons to an external circuit, including electrolyte, anode, cathode, and current collectors at the electrodes.

2.1.3 Thermodynamics

For SOFC with an oxygen-ion-conducting electrolyte, the reactions in the fuel cell involve the oxidation of fuel at anode and reduction of oxygen at the cathode. The driving force of the electrochemical process is the oxygen partial pressure difference between the cathode and anode [13, 30]. The electrochemical reactions at the interfaces of the electrolyte and the electrodes are shown in Figure 2.3. At the cathode, the reduction of oxygen in a SOFC based on an oxygen-ion-conducting electrolyte is given:

$$O_{2(c)} + 4e^- \rightarrow 2O_{(e)}^{-2}$$
 Equation 2.1

where the subscript (c) and (e) represent the state at the cathode and in the electrolyte, respectively. At the anode side, the reverse reaction of Equation 2.1 can be regarded as thermodynamically as the primary electromotive reactions, i.e.:

$$2O_{(e)}^{-2} \to O_{2(e)} + 4e^{-}$$
 Equation 2.2

The subscript (a) is the state at the anode. The SOFC is therefore considered as an oxygen concentration cell, and the electromotive force (emf) or open circuit voltage (OCV) voltage, E_o , is given by Nernst equation [13, 30]:

$$E_o = \frac{RT}{zF} \ln \frac{pO_{2(c)}}{pO_{2(a)}}$$
 Equation 2.3

where R is the molar gas constant, T the temperature, F the Faraday constant, and pO_2 the partial pressure of the oxygen at the electrodes.

As the oxygen ions are transported through the cathode and the electrolyte to the anode side driven by the oxygen partial pressure difference, the fuel gas will be oxidized into water and CO_2 at the anode,

$$H_2 + O^{2-} \rightarrow H_2O + 2e^-$$
 Equation 2.4

$$CO + O^{2-} \rightarrow CO_2 + 2e^-$$
 Equation 2.5

$$CH_4 + 4O^{2-} \rightarrow 2H_2O + CO_2 + 6e^-$$
 Equation 2.6

The electrochemical reaction takes place at the triple phase boundary (TPB) inside the cathode and anode, which serves as the connecting point of the gas phase (H₂, CO, CH₄ and O₂), the oxygen ion conductor and electron conductor. A large area of the TPB is favourable for a better electrochemical performance [11, 12]. The produced oxygen ions diffuse through the solid electrolyte from the cathode to the anode side, while the electrons flow from anode to the cathode via current collectors through the external circuit and produces direct-current (DC) electricity powering the electrical apparatus connected to external circuit, as demonstrated in Figure 2.3.

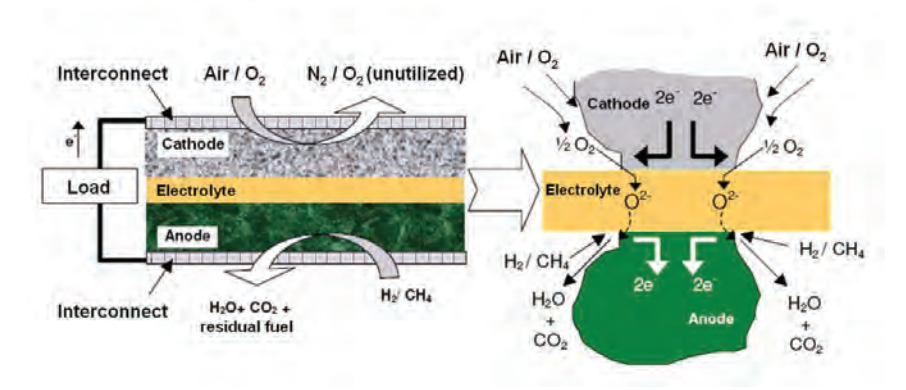


Figure 2.3 Schematic diagram of the SOFCs with reactants and reaction products.

2.1.4 Electrochemical efficiency of SOFC

The electrochemical efficiency of a SOFC is mainly determined by thermodynamic efficiency depended on intrinsic fuel properties and voltage efficiency referring the ability of the SOFCs to realize ideal voltage.

2.1.4.1 Thermodynamic Efficiency

In all types of fuel cells, the Gibbs free energy change of the cell reaction may be completely converted into electrical energy. Thus, a fuel cell has an intrinsic (maximum) thermodynamic efficiency defined as:

$$\varepsilon_T = \frac{\Delta G}{\Delta H} = 1 - \frac{T\Delta S}{\Delta H}$$
 Equation 2.7

Where, ΔH is the enthalpy of the reaction, ΔS is the entropy change and ΔG is the Gibbs free energy change during the reaction.

2.1.4.2 Voltage Efficiency

The operating voltage of a SOFC is always less than the theoretical maximum reversible voltage. As drawn in a typical current density-voltage (*i*-V) plot in Figure 2.4, the voltage falls due to varied losses. The reduction in the cell voltage under current load depends on current density, temperature, pressure, gas flow rate, cell material composition and so on. The voltage efficiency can be defined as [13]:

$$\varepsilon_V = \frac{E}{E}$$
 Equation 2.8

Where, E is the operating cell voltage and E_r the reversible voltage or so-called equilibrium voltage, often referred to open circuit voltage (OCV). Note that E_r may be greater than the OCV if there are losses caused by gas leak, side reactions, etc.

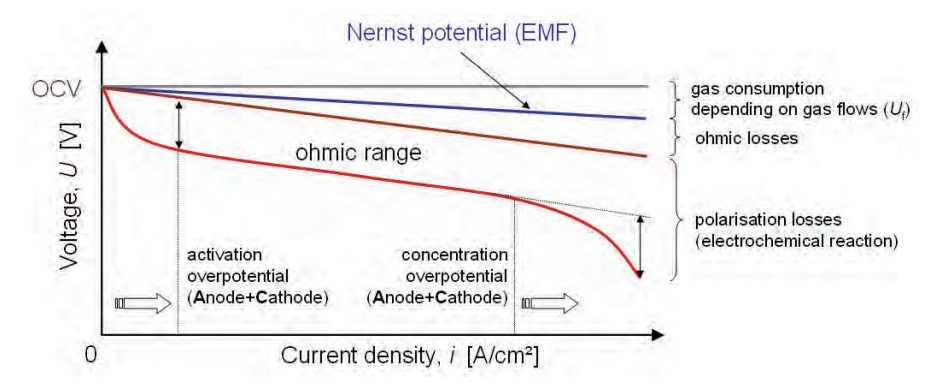


Figure 2.4 Theoretical SOFC *i*-V curve of SOFC showing different types of polarizations: activation polarization is usually dominant at low current densities, and concentration polarization is dominant at high current densities when the transport of reactive species to the electrolyte/electrode interface becomes a limiting factor for the cell reaction (image source: Dr. Robert Mücke, Large SOFC Summer School, Ancona, 2009)

The difference between the operating voltage (which includes reaction kinetics) and the reversible voltage is termed polarization, over voltage, or over potential and is noted as η :

$$\eta = E_r - E$$
 Equation 2.9

The total polarization of the cell is consisted of four components: charge transfer or activation polarization (η_A), diffusion or concentration polarization (η_D) and resistance or ohmic polarization (η_Ω):

$$\eta = \eta_A + \eta_D + \eta_\Omega$$
 Equation 2.10

It is the polarization characteristics which determine the shape of the *i*-V curve of a cell. In reality, though none of these effects can be eliminated, all can be minimized by appropriate choice of materials, microstructure, geometry and operating conditions.

Charge transfer or activation polarization ($\eta_{\scriptscriptstyle A}$)

This loss is due to the energy barrier, which must be overcome in order for the electrochemical reaction to occur. The activation potential can be considered to be the extra potential required to reduce the activation energy barrier of the rate-limiting step to a value such that the electrode reaction proceeds at the desired rate. Generally, electrode reaction rates are relatively faster at the high operation temperatures and hence activation polarization is usually small.

Diffusion or concentration polarization (η_D)

This loss is due to concentration gradient of reactants and products through the cell layers. It is most significant when the rate of supply of reactants and/or rate of removal of products is less than that required by the discharge current. Experimentally the effect is marked by a sharp drop in cell voltage. Concentration polarization is dependent on the mass transport properties of the system. Concentration polarization is most significant at high fuel conversion and current density which result in decreased fuel concentration [13].

Resistance polarization (η_{Ω})

It is caused by resistance to the flow of ions through the electrolyte and electrons through electrodes and current collectors, and by contact resistance between cell components. It is given by:

$$\eta_{\Omega} = iR_i$$
 Equation 2.11

Where, R_i represents total cell area specific resistance (ASR) and includes both ionic and electronic resistances, i is the current density. By minimizing the component thickness, for example as what has been done in this work, the η_{Ω} of the cell can be significantly reduced.

2.1.5 Electrolytes

The electrolyte has two main functions in an SOFC. Firstly, it should be gas-tight to separates fuel and oxidant gases and prevent gases diffuse through the electrolyte. Secondly, it must have good ionic conductivity at the SOFC operating temperature. The electrolyte most commonly used is yttria-stabilized zirconia (YSZ), in which Zr_2O is stabilized by substitution of divalent or trivalent cations for the host lattice cation of Zr^{4+} . This substitution creates a high concentration of oxygen vacancies by charge compensation. Ionic conductivity of the electrolyte can be described by defect chemistry using the Kröger-Vink notation.

$$Y_2O_3 \xrightarrow{Zr_2O} 2Y_{Zr}^{'} + V_O^{"} + 3_O^{\times}$$
 Equation 2.12

The high oxygen vacancy concentration results in high oxygen-ion mobility and ionic conductivity. The key specific requirements for the electrolyte in SOFC applications have been discussed intensively elsewhere [31, 32] and are summarized here.

- Stability: The electrolyte must be stable in chemical composition, morphology and dimensions under dual atmosphere (reducing atmosphere at anode side and oxidizing atmosphere at cathode side).
- Conductivity: The electrolyte must have sufficient and long-term stable ionic
 conductivity to minimized ohmic losses and negligible electronic conductivity to
 avoid voltage losses under dual atmosphere at cell operation temperature.
- 3. Compatibility: The electrolyte must be chemically compatible with the other cell components at both cell operating temperature and cell fabrication temperature. Minimal reaction between cell components is an important requirement for a SOFC electrolyte. Undesired side reactions may poison electrodes and electrolytes, introducing insulating phase or significant electronic conductivity to the electrolyte, which could reduce the performance of the cell.
- 4. Thermal expansion: Thermal expansion of the electrolyte must be compatible with all the other cell components from room temperature to cell operation and fabrication temperature. Failure to match the expansion or contraction of the cell components during heating or cooling can result in poor sealing and mechanical failure.
- Gas-tightness: The electrolyte must be gas-tight to prevent gas leak through the electrolyte.

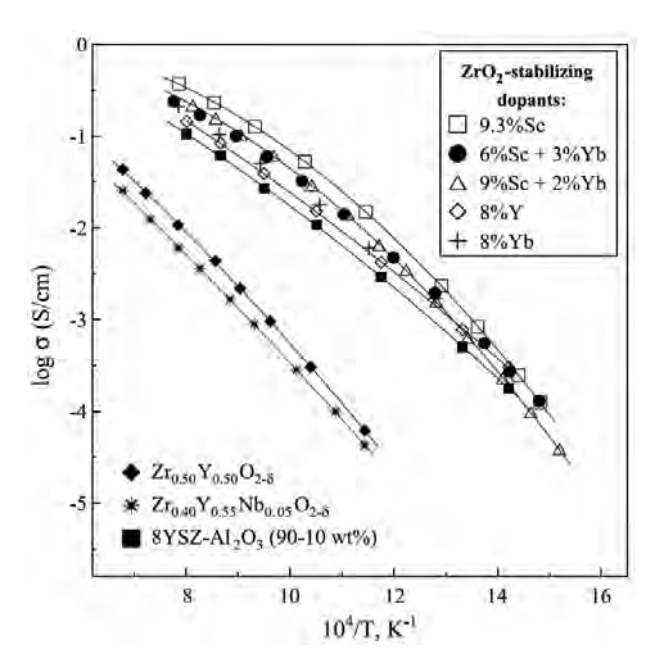


Figure 2.5 Total conductivity of ZrO₂-based solid electrolytes in air -[28, 33-36]

Up to now, researchers have extensively investigated many oxide formulations searching for candidate electrolyte materials for SOFC applications. Zirconia-based ceramics are the most widely used electrolytes due to their good ionic conductivity, low electronic conductivity and outstanding chemical stability at the anode side. The maximum ionic conductivity in ZrO₂-based systems is observed when the concentration of acceptor-type dopants is close to the minimum necessary to completely stabilize the cubic fluorite-type phase. In addition, stabilized zirconia ceramics exhibit a minimum electronic contribution to total conductivity in comparison with other solid electrolytes [37-39].

Yttria-stabilized zirconia and scandia-stabilized zirconia (ScSZ) are suitable for anode-supported SOFCs operating above 650 °C and below 650 °C, respectively. Figure 2.5 compares the conductivity of selected ZrO₂-based electrolytes, including one YSZ-Al₂O₃ composite [28, 33-36]. As shown in Figure 2.5, yttria stabilized zirconia shows an ionic conductivity of about 0.04 S/cm for 8mol% YSZ at 800 °C while that scandia stabilized zirconia is about and 0.14 S/cm for 9.3mol% ScSZ at 800 °C[39]. In this work, we choose conventional 8YSZ as the electrolyte material due to its balanced properties.

For SOFCs operated at temperature below 550 °C, ceria based electrolyte could be a promising candidate. Among ceria-based phases, the highest level of oxygen ionic transport is characteristic of the solid solutions Ce_{1-x}Gd_xO_{2-δ} and Ce_{1-x}Sm_xO_{2-δ}. The ionic conductivity obtained for Ce_{0.9}Gd_{0.1}O_{1.95} is 0.01 S/cm at 500 °C, respectively [28, 40, 41]. The main disadvantage in using ceria based materials as SOFC electrolyte resulted from the partial reduction of Ce⁴⁺ to Ce³⁺ under the reducing conditions at the anode side [42-45], which gives rise to negative effects: (1) it introduces n-type electronic conductivity which causes a partial internal electronic short circuit in a cell; (2) it generates nonstoichiometry (with respect to normal valency in air) and expansion of the lattice which can lead to mechanical failure [28].

Perovskite materials are also promising for SOFCs, especially for the applications in the intermediate temperature range. High ionic conduction and relatively low thermal expansion is achieved by substituting the perovskite (ABO₃) with lower valence cations on the A or B sites, including the substitution of La with alkaline-earth cations (Sr, Ca, Ba) and Ga with bivalent metal cations such as Mg [46-51]. In oxidizing conditions LSGM ceramics exhibit an almost pure oxygen ionic conduction; however, significant A-site cation deficiency leads to a minor decrease of the ionic conduction and to a considerably higher n-type electronic transport in reducing atmospheres [52, 53]. Although the proton conductors, such as SrCeO₃, SrZrO₃ or BaCeO₃ substituted with Y or Yb, provide other possibilities, the reaction with the CO₂ remains as an unsolved issue [30, 54].

With the high ionic conductivity, bismuth oxide based material is another candidate with fluorite structure for SOFC application [55]. Substitution with rare earth elements such as Er^{3+} , Nb^{3+} and Dy^{3+} will transform $\delta\text{-Bi}_2O_3$ to an excellent ionic conductor. The $Bi_{0.8}Er_{0.2}O_{1.5}$ and $Bi_{0.88}Dy_{0.08}W_{0.04}O_{1.5}$ compounds that shares almost the same ionic conductivity of approximately 0.31 S/cm at 750 °C [56]. However the substitution of Sr^{3+} , Nb^{3+} and Ga^{3+} to the Bi sites, decreases the ionic conductivity to 0.01 S/cm also at 750 °C [57]. A stabilized $\gamma\text{-Bi}_4V_2O_{11}$ modified with Cu metals possesses 0.18 S/cm also at 750 °C [58]. The disadvantages of Bi_2O_3 -based materials limited the their application in SOFC, which include: (1) thermodynamic instability in

reducing atmospheres, (2) volatilization of bismuth oxide at moderate temperatures, (3) a high corrosion activity and (4) low mechanical strength.

2.1.6 Anodes

The anode of SOFC has a primary function to provide reaction sites for electrochemical oxidation of the fuel. Fuel is oxidized at the anode by oxygen ions producing water, CO₂ and electrons. In anode-supported SOFCs, the anode provides mechanical support for the other cell component. Anode-supported SOFCs have the potential for higher current and power densities than electrolyte-supported SOFCs [54, 55]. The anode material must be stable in reducing atmosphere and have adequate electronic conductivity and catalytic activity for the fuel reaction at operation temperatures. The chemical and thermal expansion compatibilities with the other cell components from room temperature to cell fabrication temperature, which are normally higher than operation temperature, are very important properties for anode of SOFCs.

2.1.7 Cathodes

The cathode of SOFC has a main function to provide reaction sites for electrochemical oxidation of the oxidant. Oxygen molecules are disassociated at the cathode with the aid of electrons from the anode reaction. The cathode material must be stable in oxidizing atmosphere and have adequate electronic conductivity and catalytic activity for the oxidant gas reaction at operation temperatures. The SOFC cathode is usually made of YSZ and lanthanum strontium manganite (LSM) or lanthanum strontium cobalt ferrite (LSCF). Much work has been done on techniques to coat the cathode onto the electrolyte [59].

The perovskite-structured strontium substituted lanthanum cobaltite ($La_{1-x}Sr_x$)_sCoO₃₋₈ (LSC) is another important candidate for SOFC cathode material, which possesses high electronic and ionic conductivity as well as high catalytic activity for oxygen reduction. LSC has been known to exhibit a higher cathodic performance than LSCF and the polarization at a LSC cathode on yttria-stabilized zirconia was very small [60-66].

2.1.8 Cell design

The planar and tubular cell geometries are most commonly used designs in cell and stack designs. In practice, many SOFCs need to be mounted into stacks in order to generated sufficient voltage and power output. The engineering issues involved SOFC stacks can be complex. Maintenance of seals at high temperature is of crucial importance to ensure reasonable electrical connections between components and channel the thermal flows in the stack.

2.1.8.1 Planar SOFC

Cell components of planar SOFC are configured as thin plates which are connected in electrical series[13, 67]. A typical example for components of a planar SOFC is demonstrated in Figure 2.6. Planar systems require many gas tight seals; gas leaks decrease potential and cell efficiency. Cells are connected in series using interconnects placed between the cells to separate fuel and oxidant gases and to provide electrical connection. According to supporting mode, planar SOFCs can be classified into five types: anode supported, electrolyte supported, interconnect supported and porous metal substrate supported.

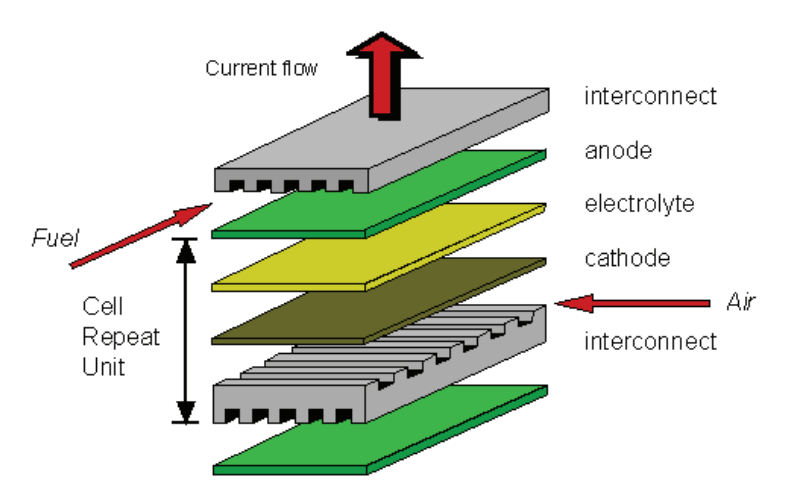


Figure 2.6 Cell repeat unit of planar SOFC design (image source: Craig Fisher, 2001)

The structural configurations of anode-supported and electrolyte-supported cells are compared in Figure 2.7. With a mechanically stable thick electrolyte ($100 \mu m$),

electrolyte-supported cells offer a relatively strong structural support as advantage and require a high operating temperature of about 800 to 1000 °C to minimize the electrolyte ohmic losses. Anode-supported cells with thin electrolytes (5-20 μ m) allow operating temperatures lower than 800 °C. Anode cermets with high conductivity have been preferred as substrates, although they have a lower stability due to re-oxidation [68].



Figure 2.7 Planar cell configurations: (a) anode-supported cell, (b) electrolyte-supported cell.

The main advantage of planar designs over other concepts is the potential to achieve higher power densities due to the short transport paths across the cell. Additionally, low-cost processes, such as screen-printing or tape-casting, can be applied for a large-scale production of SOFCs [69]. The disadvantage of the design includes the need of a high-temperature sealing. Furthermore, the ceramic layers show a lower tolerance to thermally induced stresses that will initiate cracking of the cells upon thermal cycling. The advantages of reduced operating temperature include a wider choice of materials, especially low-cost metallic materials for interconnects, reduced thermal stresses, improved reliability and longer cell life, and reduced cell costs. Main disadvantages are slow electrode reaction kinetics and reduced thermal energy.

2.1.8.2 Tubular SOFC

Tubular SOFC designs are normally with diameter larger than 15 mm or smaller 5 mm. The interconnect provides only an electrical connection between cells instead of separating fuel and oxidant gases in planar systems. Large diameter tubular designs were developed in the first place by the company Westinghouse [70], as shown in Figure 2.8. During the cell operation of tubular SOFC systems, air flows in the centre channel of the cell and fuel is fed in chamber outside the cells. The advantages of this design includes that it does not require a high-temperature seal to separate the oxidant from the fuel. This provides a long-term reliability to the system. Disadvantages are

the large current and gas path lengths through the cells, which enhance the cells resistance and limit the power density of the system. Furthermore the Electrochemical Vapour Deposition (EVD) electrolyte deposition technology is expensive and difficult to upscale. Siemens Westinghouse Power reported the successful long-term operation over 30,000 h using cathode-supported tubular SOFCs, confirming that cathode-supported tubular cells with a cell size of 22 mm diameter and an active length of 150 cm have excellent durability and reliability [71, 72].

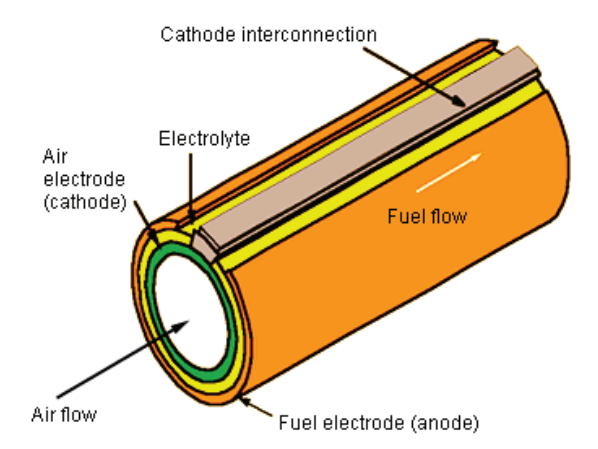


Figure 2.8 Schematic illustration of a Siemens Westinghouse tubular SOFC [73] (image source: www.energy.siemens.com)

2.2 Sol-gel processing

The sol-gel processing is one of the most widely studied methods for preparation of ceramic layers and proven to be an attractive method for fabrication of multi-component oxide ceramic thin layers [74-80]. Besides the achieved homogeneity and purity of the products, the sol-gel method often enables a lower phase-formation and sintering temperature in comparison to the conventional methods for preparation of ceramic materials [81].

The sol-gel process usually occurs in liquid solution of precursors, which lead to the formation of a new phase (sol) by means of hydrolysis and condensation reactions. A sol is a colloidal suspension of solid particles in a liquid phase and can be used for fabricate polymers or particles from which ceramic materials can be prepared. The

dispersed particles in the sol condense in a new phase (gel) in which a solid macromolecule is immersed in a liquid phase (solvent) [82].

There are two typical sol-gel processes for making ceramic layers, the colloidal sol-gel route and the polymeric sol-gel route, which are demonstrated schematically in Figure 2.9 [82, 83]. In the colloidal route, colloids form in aqueous media and the particles do not agglomerate due to mutual repulsion of same charges at the surface of the separated particles. In the polymeric sol-gel route, organometallic precursors form fine particles in alcoholic media, which also do not agglomerate with each other or segregate from the solution due to their small particle size.

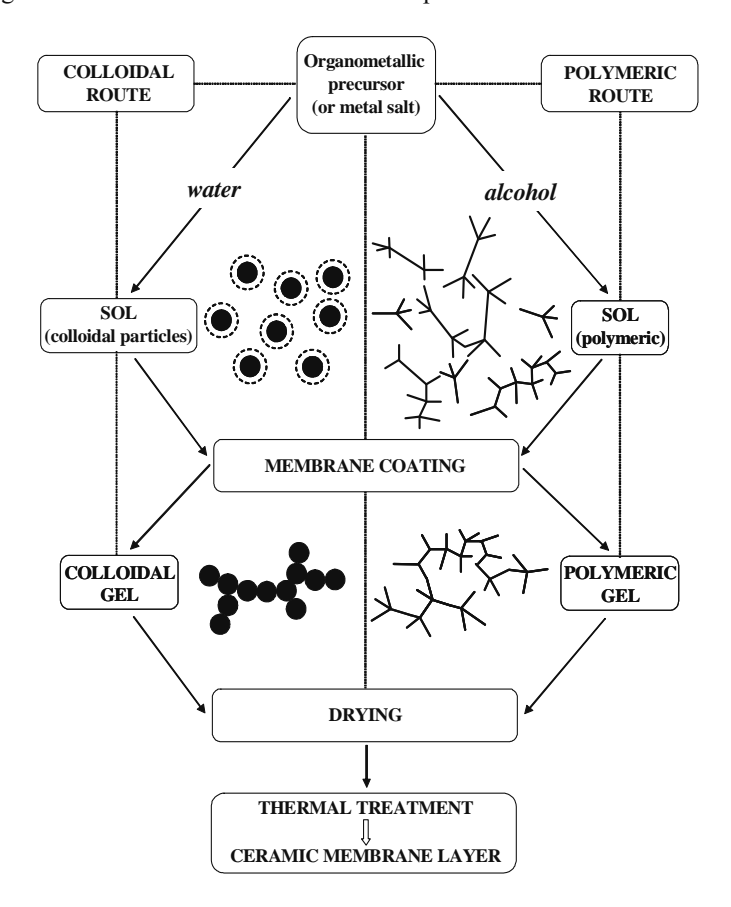


Figure 2.9 Diagram of two sol-gel processing routes for preparing ceramic layers [83]

2.2.1 Colloidal particle system

A colloid is a suspension in which the dispersed phase is so small that (~1-1000 nm) that the gravitational force is negligible and interactions are dominated by short-range

forces, such as van der Waals attraction and surface charges. A colloidal system consists of two separate phases: a dispersed phase, distributed in a finely divided state in dispersion media, the continuous phase. A colloidal system may be solid, liquid, or gaseous. Colloidal dispersions consist of fine particles in a liquid medium. If the dimensions of the dispersed phase lie in the range of 1-1000 nm, the system could possess properties of a colloidal character.

Since a colloidal system is a state of higher free energy, the particles in a colloidal dispersion may adhere to one another and form aggregates, which may settle out under the influence of gravity. An initially formed aggregate is called a floc and the process of its formation flocculation. The floc may or may not separate out. If the aggregate changes to a much denser form, it is said to undergo coagulation. Usually coagulation is irreversible whereas flocculation can be reversed by the process of deflocculation.

A stable colloidal system is one in which the particles resist flocculation or aggregation. This will depend on the balance of the repulsive and attractive forces that exist between particles as they approach one another. If all the particles have a mutual repulsion then the dispersion will remain stable. However, if the particles have little or no repulsive force then some instability mechanism will eventually take place e.g. flocculation, aggregation etc.

The van der Waals' attractive forces and the electrostatic repulsive forces are the most main factors that contribute to the total interaction free energy curve of electrostatically stabilized systems. The basic concept of colloidal stability be known as the DLVO theory, after Derjaguin and Landau's [84] and Verwey and Overbeek's [85] work. If the colloidal particles are coated with compact layers consist of long-chain polymeric molecules, the layers can prevent the particles from getting close to each other by the steric effect stabilization, which is very important for alcoholic system, where the electrostatic stabilization is hardly possible.

The DLVO theory of colloid stability proposes a balance of the repulsive electric double layer forces (positive) and the attractive van der Waals' forces (negative) that exist between particles. These two forces were found to be of similar range and magnitude. The electrical forces increase exponentially as particles approach one

another and the attractive forces increase as an inverse power of separation. Consequently, these additive forces may be expressed as a potential energy versus separation curve. A positive resultant (Figure 2.10a) corresponds to an energy barrier and repulsion, while a negative resultant (Figure 2.10b) corresponds to attraction and hence aggregation. It is generally considered that the basic theory and its subsequent modifications provide a sound basis for understanding colloid stability.

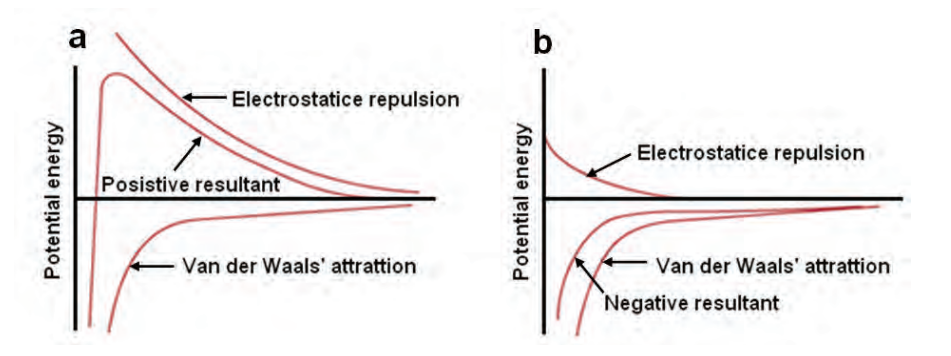


Figure 2.10 Potential energy curves for stable and unstable colloidal system

2.2.2 Polymeric and colloidal sols

The polymeric system is defined as having no dense particle larger than 1 nm, where as colloidal particulate system have identifiable primary particles lager than 1 nm. In the colloidal route, the hydrolysis rate is fast during the reaction of the precursors with excessive water and a precipitate of gelatinous hydroxide particles is formed which is peptized in a subsequent step to a stable colloidal suspension. The primary particle size ranges, depending on the system and the processing, from 1 to 20 nm and these particles can form loosely bound agglomerates with sizes ranging from 5 to 200 nm.

In the polymeric route, the hydrolysis rate is kept low by adding small amounts of water. The precursor is partly hydrolyzed and OH-groups attached to metal atoms. These hydroxyl groups give rise to condensation reactions yielding a viscous solution of inorganic-organic polymeric molecules. A complete condensation and polymerization can lead to the formation of an interlinked gel network, which contains a certain percentage of organic material.

In details, the preparation of zirconia particles in a solvent normally starts from organometallic compound precursors, such as $Zr(OC_3H_7)_4$. The chemical process can be described in the following reaction equations.

(a) Partial hydrolysis:

$$Zr(OR)_4 + H_2O \rightarrow HO-Zr(OR)_3 + ROH$$

Equation 2.13

(b) Complete hydrolysis:

$$Zr(OR)_4 + 4H_2O \rightarrow Zr(OH)_4 + 4ROH$$

Equation 2.14

(c) Condensation (formation) ZrO₂:

$$(OR)_3Zr$$
-OH + HO- $Zr(OR)_3 \rightarrow (OR)_3Zr$ -O- $Zr(OR)_3$ + H₂O

Equation 2.15

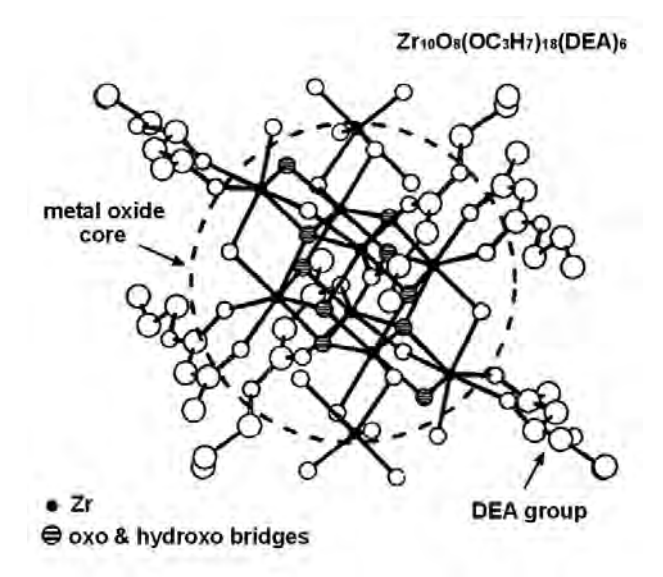


Figure 2.11 Example of a zirconium oxide cluster showing how DEA groups can form an organic shell preventing interpenetration of clusters and leading to individual zirconia nanoparticles [86]

Additives, such as diethonolamine (DEA), can be added and serve as a strong complexing ligand to modify the reactivity of alkoxides and to prevent the precipitation of inhomogeneous hydroxide particles. During the hydrolysis, DEA reacts with the alkoxides to form mixed complexes with different physical and chemical properties, which are more difficult to hydrolyze than alkoxy groups [87]:

$$Zr(OC_3H_7)_4+DEA \rightarrow Zr(OC_3H_7)_3(DEA)+C_3H_7OH$$
 Equation 2.16

The ligands also act as a functionality blocker when substoichiometric hydrolysis ratios are used. Consequently, a DEA:Zr molar ratio greater than 1 was used to prevent precipitation and led to formation of stable sol. The stability of nanoparticles in the sol was achieved through the interacting organic shells formed with the DEA groups, as shown in Figure 2.11.

2.2.3 Spin-coating

A typical spin coating process can be broken down into the four stages as shown in Figure 2.12. The deposition, spin up, and spin off stages occur sequentially while the evaporation stage occurs throughout the process. The deposition process involves the loading of an excessive amount of sol onto a stationary or slowly spinning substrate. The sol is deposited through a nozzle or pipette at the centre of the substrate. An excessive amount of sol is used to prevent layer discontinuities. In the spin up stage, the substrate is accelerated to the final spin speed. The rotational force is transferred through the sol during this process and the sol flows to the substrate edge by the centrifugal force forming a fairly uniform layer. The spin off stage is the spin coating stage where the excess solvent is flung off the substrate surface as it rotates at high speeds (800 to 2000 rpm). The sol is being thinned primarily by centrifugal forces until enough solvent has been removed to increase viscosity to a level where flow ceases. Evaporation is the complex process by which a portion of the excess solvent is absorbed into the atmosphere.

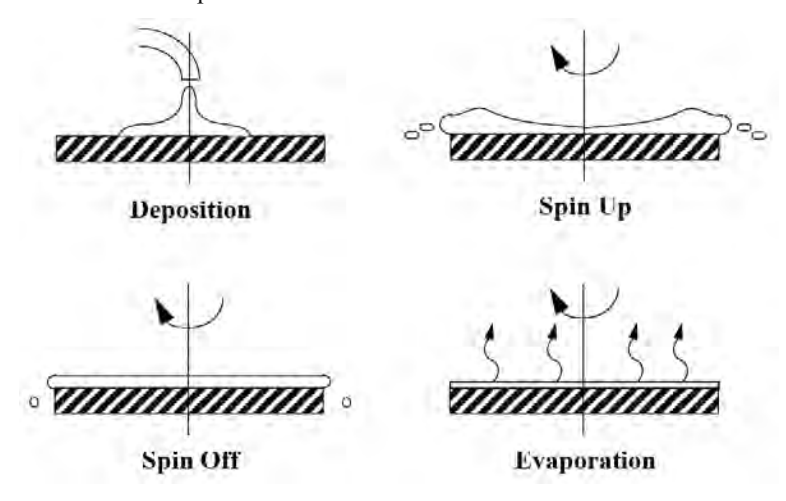


Figure 2.12 The four stages of spin coating process [88]

The physics behind spin coating involve a balance between centrifugal forces controlled by spin speed and viscous forces which are determined by solvent viscosity. The film-forming process is primarily driven by two independent parameters: viscosity and spin speed. In general, higher spin speeds and longer spin times create thinner films. For thicker films, high material viscosity, low spin speed, and a short spin time are needed. However, these parameters can affect the uniformity of the deposited layer. Usually, repeating the coating process is preferred for a deposition of a thick film.

A separate drying step is sometimes added after the high speed spin step to further dry the film without substantially thinning it. This can be advantageous for thick films since long drying times may be necessary to increase the physical stability of the film before handling. A moderate spin speed of about 25% of the high speed spin will generally suffice to aid in drying the film without significantly changing the film thickness. The spun layers reach the final thickness by evaporation stage, after which the layers become so viscous and thin that the flow stops.

2.2.4 Dip-coating

Dip-coating refers to the immersing of a substrate into a tank containing coating material, removing the sample from the tank, and allowing it to drain. The coated sample can then be dried. It is a popular way of creating thin film coated materials along with the spin coating procedure.

Scriven [89] extensively reviewed the dip coating process and proposed five stages: immersion, start-up, deposition, drainage and evaporation. In the immersion stage, a substrate or membrane support is immersed in a liquid sol (coating bath) followed by the start-up stage which results in liquid adhering the substrate surface. As the substrate is withdrawn from the coating bath, thin layers are deposited. Drainage and evaporation of the coating sol occurs during and after withdrawal of the substrate from the coating bath.

Dip-coating techniques have been widely applied in many industrial branches, such as car glass industry. The concept of dip coating is often associated with sol-gel process.

Hereby it is refers to a method to fabricate inorganic layers on planar or tubular surface [90]. The advantage of dip-coating process lies in its simple technical equipment design and the substrate can be easily coated in large size and in different shape. Precondition is that the surface of substrates can be homogeneously wetted during the dipping. Moreover, the coating can be carried out in air at room temperature. Successive thermal treatment is normally necessary. In the 1980s, glass plates were industrially dip-coated with solar-reflection layers in the size of 3x4 m² [91].

One main concern of the dip-coating method is to avoid film cracking during drying, due to the stresses caused by capillary forces associated with the gas-liquid interfaces[92, 93]. Consequently, there is a limit for the film thickness that can be obtained free of cracks in a single dip-coating step (critical thickness notion). However, crack-free and thicker coatings can be obtained by repeating the dip-coating, drying, and sintering processes know as multilayer dip-coating [94, 95].

In the case of vertical dip coating process, the theoretic relationship between the layer thickness and the properties of suspension, solution and the equipment parameters were firstly described by Levich and Landau in 1942 [96]. And the theory was extended by the works of Scriven [89], Brinker [97], and Kistler [98] in 1990s. Based on these works, the following equation between the layer thickness h, the withdraw speed v_0 , and the surface tension of the liquid γ_{LV} , the density of the liquid ρ , the viscosity of the liquid η and the acceleration of gravity g were described:

$$h = 0.94 \frac{(\eta \nu_0)^{2/3}}{(\rho g)^{1/2} \cdot \gamma_{LV}^{1/6}}$$
 Equation 2.17

This equation is based on ideal continuous process, in which a dense and smooth substrate is withdrawn with a constant speed out of the solution. By discontinuous coating process, the coefficient in the equation should be adjusted to the specific system. According to Landau und Levich [96], a pure Newtonian solution is the precondition of applying this equation. After the evaporation of the solvents, a dry layer was formed on the substrate.

2.2.5 Sintering of thin ceramic layers

Sintering is a process of densification driven by interfacial energy. The free-energy change that results in densification is originated from the decrease in surface area and reduction of surface free energy by viscous flow and diffusion. For sintering of crystalline materials, grain growth and phase transformation are often involved. According to Brinker and Mukherjee's work [82, 97, 99], a thin gel layer densifies faster than a bulk gel made from the same preparation. It is suggested the thin layer is chemically or microstructurally different from bulk gels. In fact, the thin layer is denser than bulk gels because the pores collapsed by capillary pressure during rapid evaporation and drying.

Matter transport in polycrystalline materials involves several mechanisms. According to densification mechanism, matter is transported in the process of the grain boundary and lattice diffusion between grain boundaries. During sintering, the initiation of new grain boundary area (ΔA_{gb}) is associated with a change in the surface area (ΔA_{SV}), which results in a change in surface energy:

$$\Delta E = \gamma_{sv} \Delta A_{SV} + \gamma_{gb} \Delta A_{gb}$$
 Equation 2.18

The specific surface energy of the solid-vapour interface and grain boundary is noted as γ_{SV} and γ_{gb} , respectively. In Equation 2.18, ΔA_{SV} is negative because free surface area decreases. Typically $\gamma_{SV} > \gamma_{gb}$, therefore, a transformation from solid-vapour interface or surface into grain boundary reduces the free energy.

The densification of ceramic is accompanied by coarsening the microstructure, involving growth of grains and pores. Grain growth occurs in porous materials, as well as in fully dense materials, as long as the temperature is sufficiently high. The interactions between grains and pores during grain growth complicate the microstructure evolution. The grain boundary is a region with highly disordered arrangement of atoms. The atoms transport from the convex surface of the vicinity of grain boundary to the concave surface of the adjacent grains. For polymeric sol-gel derived thin layers, oversintering may occur easily because of two factors: (1) a relatively low green density of the layer may cause discontinuity when the inhomogeneous or abnormal grain growth happens; (2) high reactivity of the nano-

scaled particles (less than 10 nm) gives rise to a reduced sintering temperature, as well as a reduced oversintering temperature, which may be less than 1000 $^{\circ}$ C.

3 Experimental

3.1 Electrolyte preparation strategies

The multi-layered electrolyte deposition concept is illustrated in Figure 3.1. A sequence of zirconia layers is deposited on the top of a macroporous anode substrate. The substrate provided the deposited layers with mechanical strength to withstand pressure without breaking or collapsing. Intermediate layers first deposited on the macroporous substrate to reduce the pore size into mesoporous range. Finally very thin microporous top layer is deposited, which are then co-sintered together with intermediate layers into a dense electrolyte.

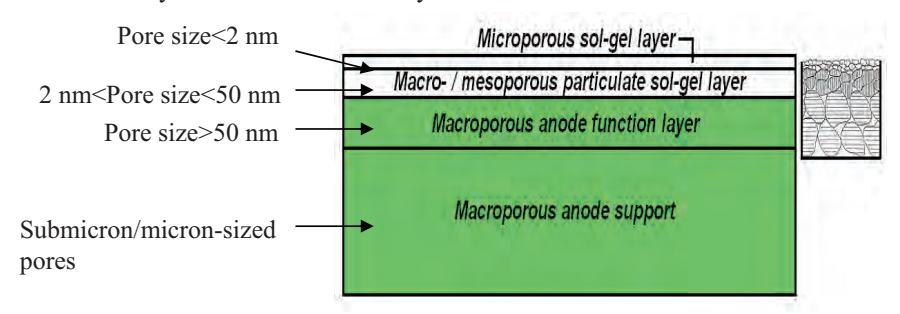


Figure 3.1 Graded layer deposition concept

3.2 Synthesis and sample preparations

3.2.1 A two-step polymeric zirconia sol-gel process

As shown in Figure 3.2, a two-step catalysed hydrolysis process was employed to prepare polymeric sols using Zr-n-propoxide, Yttrium (II)-butoxide mixture (Sigma-Aldrich GmbH, Darmstadt, Germany), diethonolamine (DEA), n-propanol, 1M nitric acid (HNO₃). Diethonolamine (DEA), used as complexing ligand to modify the reactivity of alkoxide precursors and to prevent inhomogeneous precipitation of hydroxide particles [86, 87]. The stability of nanoparticles in the sol was achieved through the interacting organic shells formed with the DEA groups. The DEA was first diluted in n-propanol and then added into Zr-n-propoxide and Yttrium (II)-

butoxide mixture (Sigma-Aldrich GmbH, Darmstadt, Germany), which were mixed with the Y³⁺:Zr⁴⁺ ratio of 16:92. The addition of acid-water-n-propanol-mixture was carried out drop wise at a dropping speed of 1.5ml/min under constant stirring, meanwhile co-hydrolyzation took place and a homogeneous YSZ sol formed. During the synthesis, the Zr-n-propoxide/Yttrium (II)-butoxide/n-propanol/DEA mixture was placed in a glove box filled with nitrogen to avoid hydrolysis with atmosphere moisture.

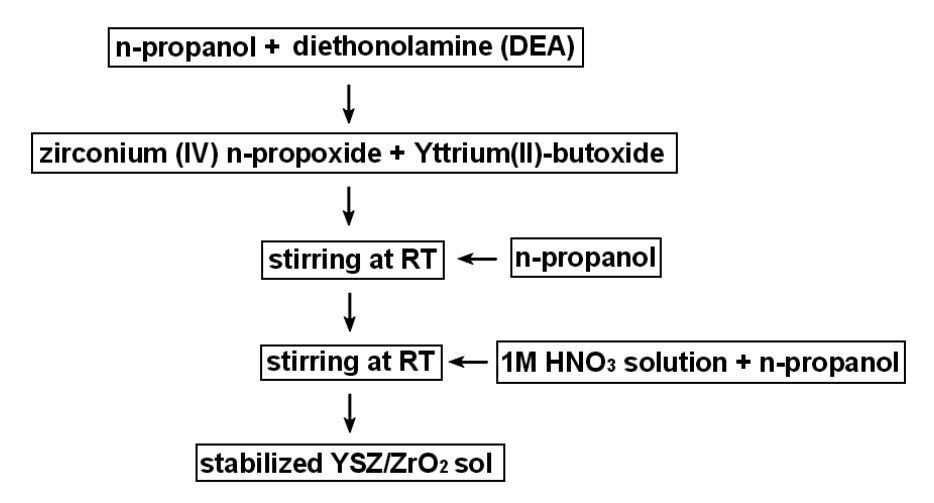


Figure 3.2 Scheme of preparation a colloidal sol

3.2.2 Synthesis of colloidal sol

1M HNO₃ solution was dropped into iso-propanol solution of zirconium n-propoxide (Alfa Aesar GmbH, Karlsruhe, Germany, molecular weight=327.56). This zirconia solution was peptized at 90 °C for 3-30 hours. Finally, YSZ sols were formed by adding the proper amount of yttrium nitrate to the sol. The HNO₃ solution is used here to adjust the zeta potential of the colloidal system to prevent coagulation or flocculation of the reaction products.

Oxalic acid dihydrate (Sigma-Aldrich GmbH, Darmstadt, Germany) was dissolved in water, namely solution 1. And yttrium nitrate hexahydrate (Sigma-Aldrich GmbH, Darmstadt, Germany) and zirconyl chloride octahydrate (Sigma-Aldrich GmbH, Darmstadt, Germany) were dissolved in water with the Y³⁺:Zr⁴⁺ weight ratio of 16:92, namely solution 2. Then solution 1 were carefully added in to solution 2 and the

mixture was stirred for 10 minutes and put into a climate chamber heated at 98°C for 1-4 hours to obtain sols with different particle size distributions. A longer heating time results in a lager average sol particle size.

3.2.3 Preparation of commercial colloidal zirconia and ceria nano-suspension

In a typical procedure, 8 g of 8YSZ or CGO nano-powders was first added in to 200 ml 0.05 M nitric acid solution to form a suspension. Then the suspension was intensively ultrasonically treated by means of an ultrasonic homogenizer Sonifier® 450 (Branson Ultrasonics, Danbury, USA) for 20 minutes. Ultrasonic irradiation was operated at 20 kHz, with a maximum input power of 400W. Then the homogenized suspension was treated by high-performance centrifuge separation (Heraus Biofuge primo Centrifuge, Thermo Scientific, Bonn, Germany) to remove large agglomerates, colloidal sols with graded particle size distribution were obtained.

3.2.4 Synthesis of CGO, LSM and LSFC polymeric sols from inorganic metal salts

3.2.4.1 CGO sol

50 ml propionic acid, 50 ml water and 2.5 g DEA were mixed in a flask to form solution 1. Then 0.016 mol Cerium (III) acetate hydrate (Sigma-Aldrich GmbH, Darmstadt, Germany) and 0.004 mol Gadolinium (III) acetate hydrate (Alfa Aesar GmbH, Karlsruhe, Germany) were carefully added into solution 1. A clear sol was synthesized after 3-hour refluxing the mixture at 85 °C.

3.2.4.2 LSM sol

50 ml propionic acid, 50 ml water and 2.5 g DEA were mixed in a flask to form solution 2. Then 0.0065 mol lanthanum (III) acetate hydrate (Sigma-Aldrich GmbH, Darmstadt, Germany), 0.003 mol strontium (II) acetate (Sigma-Aldrich GmbH, Darmstadt, Germany) and 0.01 mol Manganese (II) acetate tetrahydrate (Aldrich) were carefully added into solution 2. A clear sol was synthesized after 3 hour refluxing the mixture at 85 °C.

3.2.4.3 LSFC sol

50 ml propionic acid, 50 ml water and 2.5 g DEA were mixed in a flask to form solution 3. Then 0.0058 mol lanthanum (III) acetate hydrate (Sigma-Aldrich GmbH, Darmstadt, Germany), 0.004 mol strontium (II) acetate (Sigma-Aldrich GmbH, Darmstadt, Germany), 0.008 mol Iron (III) nitrate nonahydrate (Merck KgaA, Darmstadt, Germany) and 0.002 mol cobalt acetate tetrahydrate (Sigma-Aldrich GmbH, Darmstadt, Germany) were carefully added into solution 3. A clear sol was synthesized after 3-hour refluxing the mixture at 85 °C.

3.2.5 Preparation of powders

All sols were gelled at 60 °C under normal atmospheric conditions to form xerogels. Bulk xerogel samples were calcined from 400 to 600 °C. The calcination process was carried out at a ramp rate of 100 K/h for xerogels and held for 2 hours at the desired temperature.

3.2.6 Preparation of substrate and anode

The anode substrates (NiO/8YSZ), pre-sintered at 1230 °C for 3 h, were produced by warm pressing using a so-called Coat-Mix[®] material [100] or tape casting methods. The powder mixture is made of 57 wt.-% NiO (Mallinckrodt Baker, Inc., Phillipsburg, U.S.A.) and 43 wt.-% 8YSZ (Unitec Ceramics Ltd., Stafford, UK). An overview of the porosity of the substrates, which was derived from pycnometer measurements, is shown in Table 3.1.

Substrate type	Thickness	Density	Porosity
	(mm)	(g/cm ³)	(Vol%)
Coat-mix warm pressed	1.0-1.6	4.03±0.01	44±1
Tape cast FG31	0.5-0.6	3.79±0.02	48±1
Tape cast FG02	0.5-0.6	4.79±0.01	33±1

Table 3.1 Overview of the thickness, density and porosity of the reduced substrates [101]

An electrochemically active anode functional layer (NiO/8YSZ, thickness approx. $7 \mu m$) was deposited by vacuum slip casting or screen printing on anode substrates and calcined at 1000 °C for 1 h. The calcination ramping and cooling down rate was

set up at 180 K/h and 300 K/h, respectively. More details about the manufacturing process can be found elsewhere [102, 103].

3.2.7 Preparation of YSZ electrolyte layer

In order to reduce the pore size of the top layer prior to layer deposition, the support was coated with intermediate layers of YSZ suspension or colloidal YSZ sols and calcined at different temperatures. The sols with graded particle size (5-150 nm) was deposited by vacuum slip casting, spin coating with a Delta 80T2 spin coater (Suss Micro Tek AG, Garching, Germany) or dip-coating with programmable single side dip-coater (Pervatech BV, MC Enter, the Netherlands), as shown in Figure 3.3.

The coated samples were calcined in electrical oven (Nabertherm GmbH, Lilienthal, Germany) or Rapid Thermal Process Equipment (Xerion Advance Heating Ofentechnik GmbH, Freiberg, Germany). The process of coating and calcination was repeated to obtain the desired configuration of graded multi-layered electrolyte.

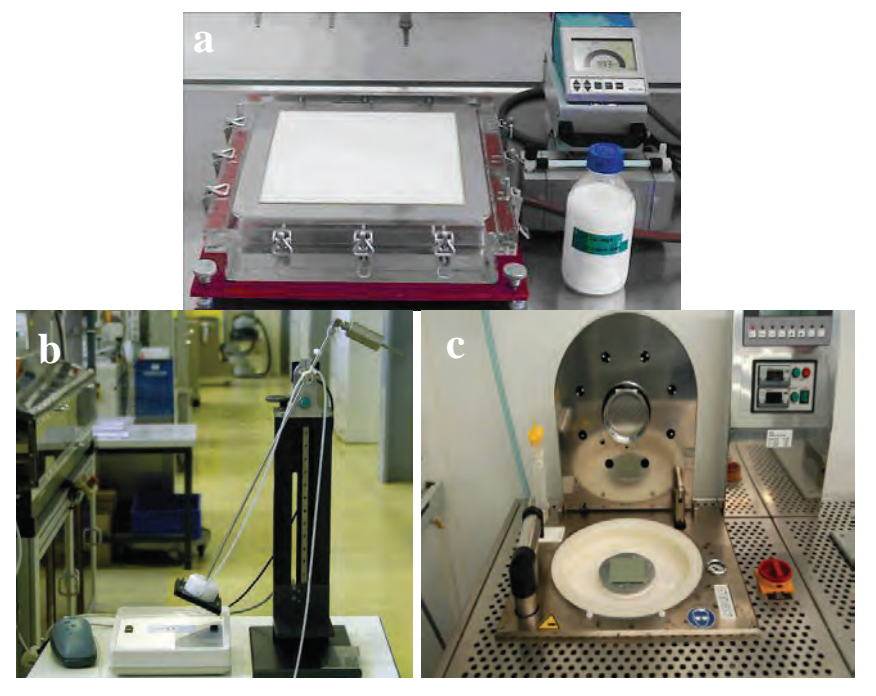


Figure 3.3 Electrolyte deposition equipments: (a) vacuum slip casting (b) Dip-coating (c) Spin-coating

3.2.8 Preparation of CGO barrier layer

In order to prevent Sr-diffusion during the manufacturing and operation of SOFCs, $Ce_{0.8}Gd_{0.2}O_{2-\delta}$ was applied on top of 8YSZ electrolyte by reactive sputtering from a planar metallic target with a nominal alloy composition of 80 at.% Ce and 20 at.% Gd (99.7% purity of the alloy) and an oxygen flow of 2-10 cm³/min. The base pressure in the process chamber was 10^{-6} Pa. The specific target power density during deposition ranged from 1-2 W/cm², leading to a deposition rate of 12 nm/min.

All physical-vapor-deposited CGO coatings were applied by a commercial physical vapor deposition cluster system CS 400 ES (Von Ardenne Anlagentechnik, Dresden, Germany). Prior to deposition, the substrate surfaces were cleaned by supersonic cleaning with organic solvents in order to remove residual dust, especially vacuum grease or oils (e.g. from helium leak tests of the substrates). After drying, the substrates were sputter-etched and subsequently coated. The substrates were heated at a rate of 3 K/min to 800 °C.

3.2.9 Preparation of cathode

The cathode material, $La_{0.58}Sr_{0.4}Fe_{0.2}Co_{0.8}O_{3-\delta}$ (LSFC) and $La_{0.58}Sr_{0.40}CoO_{3-\delta}$ (LSC) were synthesized by spray drying as described by Kontouros et al.[104]. After calcination of the powders, they were ground by ball milling for several hours until a mean particle size (d_{50}) of approximately 0.8 μ m was achieved. The cathodes were screen-printed using pastes with an ethyl cellulose binder and a terpineol-based solvent. The LSCF cathode was then sintered at 1040 °C and the LSC cathode was calcined at 800 °C on the CGO barrier layer resulting in a thickness of about 40 μ m.

3.3 Characterizations

3.3.1 Particle size distribution

The particle size distribution (PSD) of the sols and suspensions was characterized by LB-550 Dynamic Light Scattering Nano-Analyzer (Horiba Europe GmbH, Germany). The LB-550, using a dynamic light scattering technique, is able to measure very concentrated suspensions, up to 40% solids in many cases, over a size range of 1 nm-

6 μ m. The median diameter (d_{50}) of the particles in the sols and suspensions was measured.

3.3.2 Adsorption

Physical characterisation of synthesized powders was carried out by nitrogen adsorption at 77K to determine the pore volume, surface area and pore size. All samples were degassed at 200 °C prior to sorption and adsorption experiments. The weight of adsorbed gas was measured as a function of partial pressure.

Based on the isotherm plots, the specific surface area was calculated by BET method. The mesopore size distribution and cumulative pore volume were calculated by Barret-Joyner-Halenda (BJH) method, while the micropore size distribution and cumulative pore volume were calculated by the Horvath and Kawazoe (H&K) model.

3.3.3 Surface topography and deflection measurement

Surface topography and deflection measurement of the planar samples were performed on Cyber Scan CT200 (Technologies GmbH, Ingolstadt, Germany) non-contact laser scanning inspection system. A confocal laser sensor LT-9010M (Keyence Deutschland GmbH, Neu-Isenburg, Germany) and a laser Triangulations senor DRS 8000 (CyberOptics Ltd., North Yorkshire, UK) were used to obtain surface topography and deflection information, respectively.

3.3.4 Dilatometry

The sintering behaviour of several YSZ powders has been characterized by a push—rod dilatometer Setsys 16/18 (Setaram Inc., Caluire, France). The 8YSZ powders were first pressed into pellets using a uniaxial press with a pressure of 100 MPa. The pressed pellets were heated up to 1400 °C under air with a rate of 3 K/min. After a dwelling time of 5 hours, the pellets were cooled down with a rate of 8 K/min. The dilatometric plots were recorded.

3.3.5 Helium leak rate test

The gas-tightness of sintered electrolyte (half-cell dimension: 65 mmx65 mm)was examined with a Qualytest HTL 260 helium leak rate test module (Pfeiffer Vacuum GmbH, Asslar, Germany) in Forschungszentrum Jülich GmbH (IEF-1). The helium flow through the half-cell was determined with a mass spectrometer at a pressure difference of 1000 hPa. The values were normalized to measured area (16 cm²) and to a pressure difference of 100 hPa, which is typical for an SOFC stack [105].

3.3.6 X-ray diffraction (XRD)

Phase characterization was performed by Siemens D5000 diffractometer (Siemens AG, Karlsruhe, Germany) equipped with a monochromated $CuK\alpha$ radiation source. The XRD results then were represented in terms of $Cu-K_{\alpha,\beta}$ radiation intensity (arbitrary unit) versus the diffraction.

It is possible to estimate average domain size (τ) of the powder samples, in Å, via Scherrer equation [106]:

$$\tau = K \lambda / \beta_{\tau} \cos\theta$$

where β_{τ} is the line broadening due to the size effect of small domain. Regarding the thermal treatment of the samples, β_{τ} is given by (B-b) using Lorentz model, while B and b is the breadth of the reflection line and the instrumental broadening, respectively. Note β_{τ} that must be given in radians. K is the so-called shape factor, which usually takes a value of about 0.9, assuming the particle shape is spherical. The λ is the wavelength of the radiation, $\lambda_{Cu} = 1.54056$ Å.

3.3.7 SEM and TEM

Microstructure characterization of the powders and thin layers was performed using a Zeiss Ultra 55 scanning electron microscope (Carl Zeiss NTS GmbH, Oberkochen, Germany) equipped with an INCA energy dispersive X-ray (EDX) analysis system (Oxford Instruments, Uedem, Germany) and a Tecnai G2 F20 (FEI, Eindhoven, the Netherlands) field emission transmission electron microscope.

3.3.8 Electrochemical impedance spectroscopy (EIS)

3.3.8.1 Cell preparation and geometry

The SOFC single cells analyzed within this study were based on $5x5 \text{ cm}^2$ anode substrates with an average thickness of about 0.6 mm. On these substrates, an NiO/8YSZ anode functional layer ($\sim 5 \mu \text{m}$) was screen-printed and fired at $1000 \,^{\circ}\text{C}$ for 1 h. The 8YSZ electrolyte ($\sim 1 \mu \text{m}$) consisted of dip-coated nano-suspension layers and spin-coated polymeric sol-gel layers, which were co-sintered at $1400 \,^{\circ}\text{C}$ for 5 h. A $Ce_{0.8}Gd_{0.2}O_{2-\delta}$ (CGO) diffusion barrier layer (approx. $0.5 \, \mu \text{m}$) was magnetron sputtered at $800 \,^{\circ}\text{C}$ on the electrolyte. On top of CGO layer, a $La_{0.58}Sr_{0.4}Co_{0.2}Fe_{0.8}O_{3-\delta}$ cathode was applied by screen-printing, resulting in a thickness of approx. $50 \, \mu \text{m}$ after sintering. Details regarding the manufacturing procedures can be found elsewhere [102, 107].

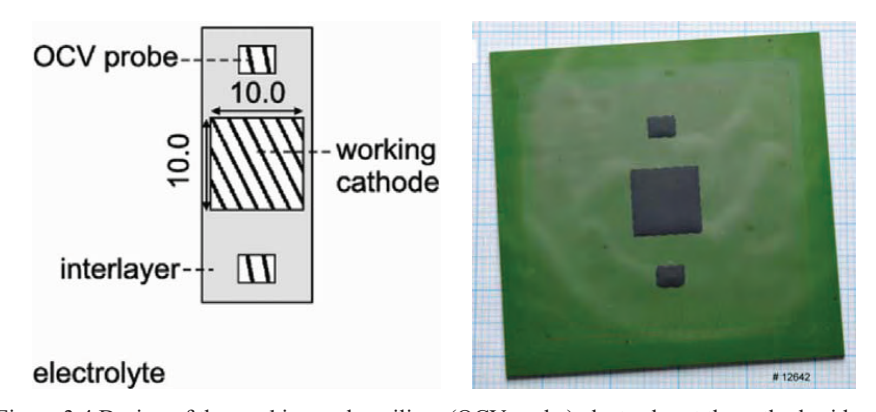


Figure 3.4 Design of the working and auxiliary (OCV probe) electrodes at the cathode side of the anode-supported SOFC single characterized cell

The active area of the working cathode was $10x10 \text{ mm}^2$. Two auxiliary electrodes in gas flow direction in front of and behind the cathode were applied for open-circuit voltage (OCV) control (OCV probes in Figure 3.4). The electrodes were separated from the electrolyte by a continuous CGO interlayer with lateral dimensions of 12x30 mm. The cell geometry is also shown in Figure 3.4.

3.3.8.2 Impedance measurements

The electrochemical impedance spectroscopy characterization and data processing in this work is made by Institute of Materials for Electrical and Electronic Engineering at Karlsruhe Institute of Technology.

The single cells were mounted into ceramic housings. Cathode and anode were contacted by gold and nickel meshes, respectively and gold rings were used for sealing. The cells were operated under ambient pressure with different N₂/O₂ mixtures at the cathode side and varying H₂O/H₂ mixtures at the anode side. High contents of water vapor could be formed by feeding oxygen into an upstream combustion chamber. The total anodic and cathodic gas flow rates were maintained at a constant value of 250 ml/min during all experiments. The cells were tested over a range of temperatures between 550 and 850°C. Impedance measurements were carried out with a Solartron 1260 frequency response analyzer (Solartron Analytical AMETEK Advanced Measurement Technology GmbH, Meerbusch, Germany) in a frequency range from 0.1 Hz to 1 MHz. The amplitude of the current stimulus was chosen in order to achieve a voltage response not higher than 12 mV. All experiments within this investigation were conducted under open-circuit conditions. To investigate the parameter dependence of each single polarization process, a series of impedance measurements was carried out in which only one cell parameter at a time was varied, such as oxygen partial pressure, water partial pressure, temperature.

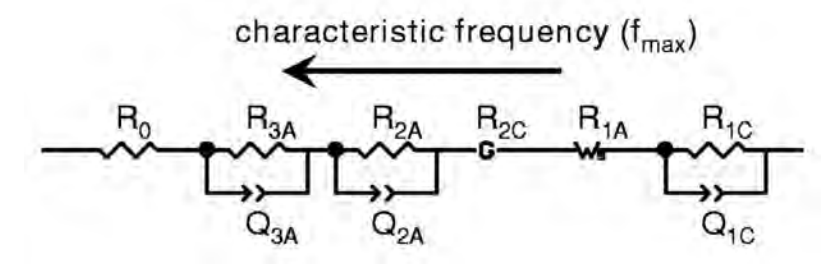


Figure 3.5 Equivalent circuit of electrochemical impedance spectrum [108]

Based on an accurate analysis of all recorded impedance data and their corresponding distribution function of relaxation times (DRTs), an equivalent circuit model composed of five impedance elements connected in series, as demonstrated in Figure 3.5, was applied in interpreting the impedance spectra, as described in the literature [108].

3.3.9 Electrochemical single cell test

The electrochemical single cell tests and data processing in this work is made by Institute for Energy Research (IEF-3) at Forschungszentrum Jülich GmbH. The electrochemical measurements of the single cells were performed in an alumina test housing placed inside a furnace. The size of the tested cells was 50x50 mm² with active cathode area of 40x40 mm². In order to obtain sufficient electronic contact between the cell and the electronic devices, a Ni mesh and a Pt mesh were used at the anode side and the cathode side, respectively. The gas tightness of the gas compartment was obtained by a gold sealant. During the start-up of the tests an argon flow was injected at the anode side and an air flow at the cathode side. The temperature was then slowly increased to the temperature for anode reduction. After reaching this temperature, the anodes of the single cells were reduced by gradually replacing the argon by hydrogen. Water vapour (3 vol.-%) was added by saturating the hydrogen gas through a water bubbler and condenser (super saturation and condensation) at the desired dew point of 24 °C. The total gas flows of hydrogen and air were both set at 1000 ml/min (standard temperature and pressure: STP) using mass flow controllers. The electrochemical performance was measured at varied temperature in the range of 600 to 900 °C. All electrochemical data were obtained by direct current methods using a current-control power supply type Gossen 62N-SSP500-40 (Gossen-Metrawatt GmbH, Nürnberg, Germany), and a computercontrolled data acquisition system including a data logger type NetDAQ 2640A (Fluke, Eindhoven, the Netherlands).

The current–voltage characteristics (*i*-V curves) were measured with increasing current load by a sequential step change of 0.0625 A/cm² starting from zero until either the voltage dropped below 0.7 V or the maximum current load of 1.5 A/cm² was reached. If the current density is higher than 1.5 A/cm² at 0.7 V, a linear extrapolation is applied to determine the current density. For all the different types of single cells, at least two nominally identical cells were measured [109-111]. The open circuit voltage (OCV) plots are also measured in the test. The area specific resistance (ASR) of the cell is calculated, based on the data from the linear part of the *i*-V curve.

4 Results and discussion

4.1 Fundamental characterization of materials

4.1.1 YSZ polymeric sols and derived powders

Particle size distribution, rheology behaviour and other properties are very important factors in fabrication of homogeneous ceramic layers via sol-gel method. The investigation results are reported in the following part. The particle size distribution (PSD) of a powder, or granular material, or particles dispersed in fluid, is a list of values or a mathematical function that defines the relative amounts of particles present, sorted according to size.

Zr-precursor concentration	d_{10} (nm)	<i>d</i> ₅₀ (nm)	<i>d</i> ₉₀ (nm)
0.155mol/L	2.8	4.1	5.4
0.31 mol/L	4.5	6.1	8.1
0.465mol/L	5.6	7.8	10.7

Table 4.1 Particle size of 8YSZ polymeric sols at 25°C

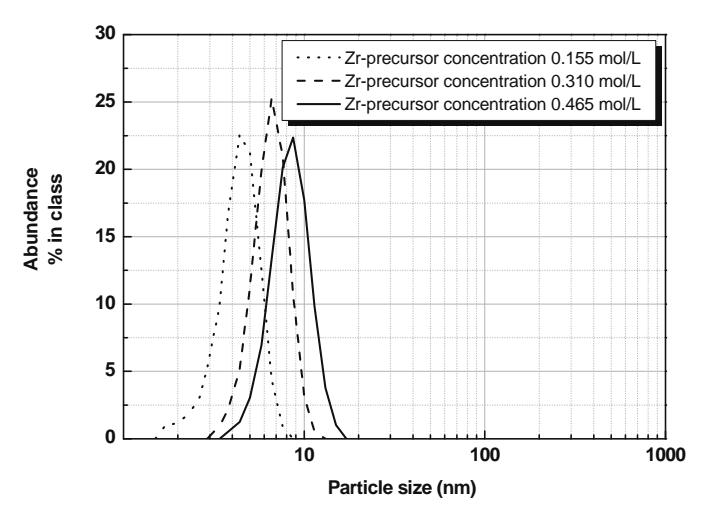


Figure 4.1 Particle size distribution of 8YSZ polymeric sol under varied precursor concentrations

The particle size of the as-prepared polymeric sol was measured at room temperature, listed in Table 4.1 and plotted as curves in Figure 4.1. As the precursor concentration of the synthesized polymeric sols increased from 0.155 mol/L, 0.310 mol/L to 0.465 mol/L, the measured median particle size (d_{50}) increased from 4.1 nm, 6.1 nm to 7.8 nm, accordingly, which shows a linear dependence on the precursor concentration, as illustrated in Figure 4.2. The particle size distribution is very narrow as the d_{10} and d_{90} of the sols are rather close to the d_{50} values (Table 4.1).

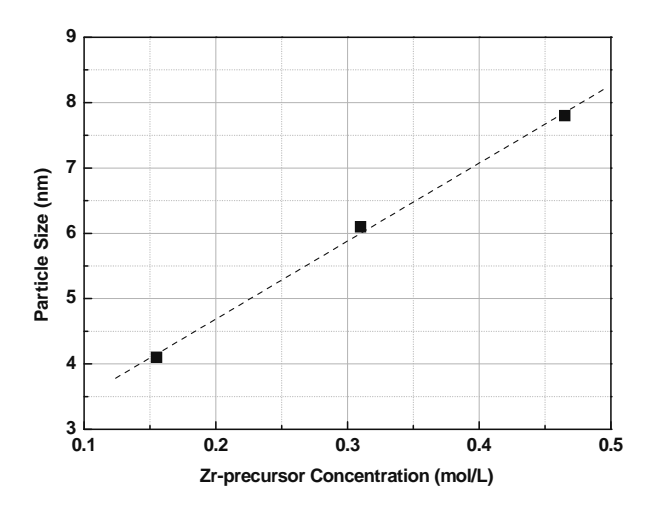


Figure 4.2 Dependence of d_{50} on Zr-precursor concentration in 8YSZ polymeric sols

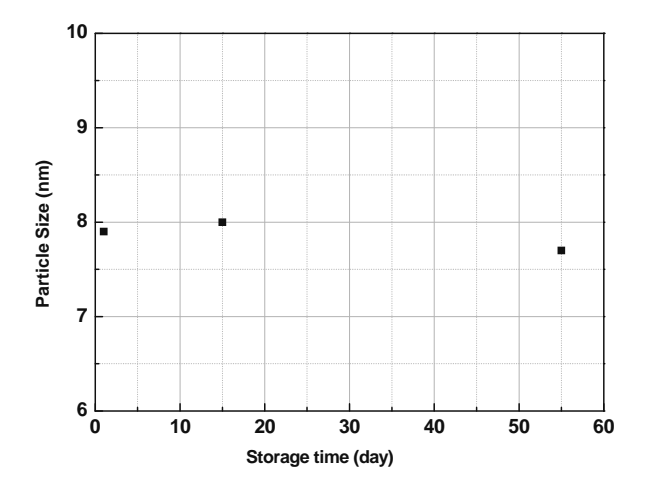


Figure 4.3 d_{50} of 8YSZ polymeric sol vs storage time

The particles have a tendency to grow as the precursor concentration increases, in order to reduce the specific surface area and to reach a more stable energy state. Under the thermal-dynamically stable equilibrium state, the particle size of the asprepared sols with different concentrations remained unchanged for over 50 days at room temperature, seen in Figure 4.3. Apart from the particle size distribution, viscosity is another important factor that frequently influences the layer formation behaviour of the sol. A low sol viscosity can result in the penetration of the sol into the pores in the support, rather than forming a layer on the substrate surface. In order to increase the sol viscosity, binders are often employed. Besides the addition of binders, the control of sol concentration offers a substantial way to increase of sol viscosity. On the other hand, a very viscous sol tends to cause irregularity on the substrates resulting in inhomogeneous coatings. Additionally, the viscosity of a solution undergoing hydrolysis and polycondensation is time-dependent and often related to the size of the particles. High precursor concentration normally results in formation of larger molecules, and consequently leads to higher viscosity. Thus, any variation of the processing parameters that induces an increase of particle size may increase the viscosity of the sol.

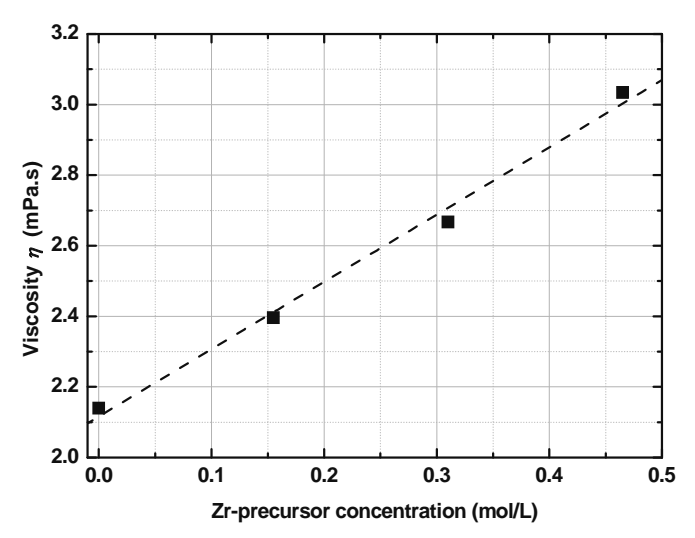


Figure 4.4 Dependance of viscosity on Zr-precursor concentration in 8YSZ polymeric sols

In the case of the as-prepared polymeric sols, the precursor concentration is so low that the propanol as the only solvent dominates the Newtonian fluid property of the sols. It can be seen in Figure 4.4, the viscosity increased steadily from 2.4 to 2.8 mPa·s by tuning the Zr-precursor concentration from 0 mol/L to 0.465 mol/L. The viscosity also shows a linear dependence on the precursor concentration as the particle size increased. Sealed and stored in flasks at room temperature for 60 days, the viscosity of the as-prepared 8YSZ polymeric sols remained stable and unchanged, seen in Figure 4.5.

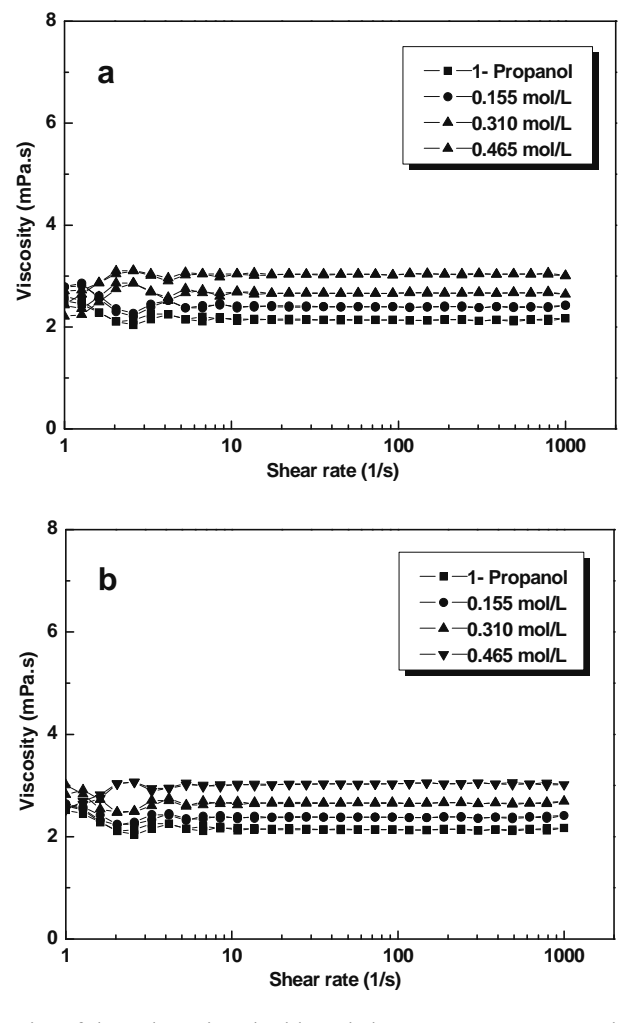


Figure 4.5 Viscosity of the polymeric sol with varied Zr-precursor concentration: (a) freshly prepared sol (b) sol stored for 60 days

In order to determine the phase structure and domain size of the synthesized 8YSZ materials, the 8YSZ polymeric sol was gelled and calcined at varied temperature to

obtain polycrystalline powders. According to X-ray diffraction analysis results in Figure 4.6, the powder was confirmed to be single phase solid solution with Fluorite crystal structure. Using the Scherrer equation, the domain size of the samples are estimated to be 3.1 nm (450°C), 3.9 nm (600°C) and 5.1 nm (900°C), respectively, which reveals a clear growth tendency of the domain size as the calcination temperature increases, also shown in Figure 4.7.

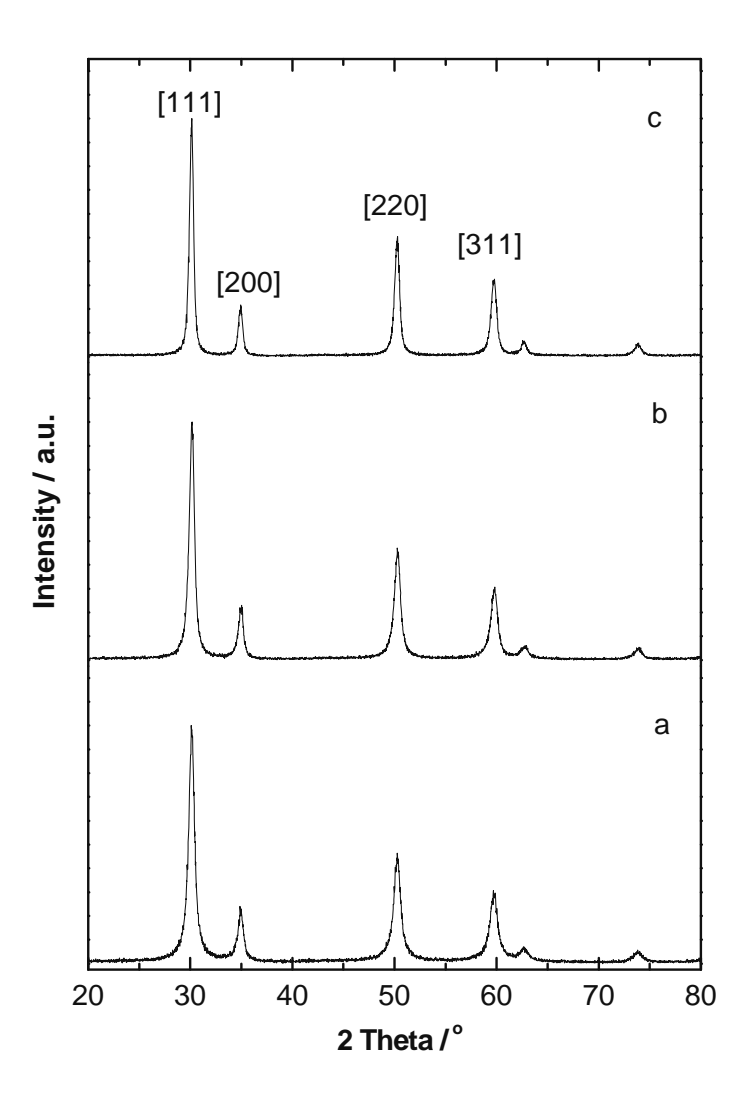


Figure 4.6 XRD patterns of the calcined 8YSZ powder derived from polymeric sol, calcined at: (a) 450° C, (b) 600° C, (c) 900° C

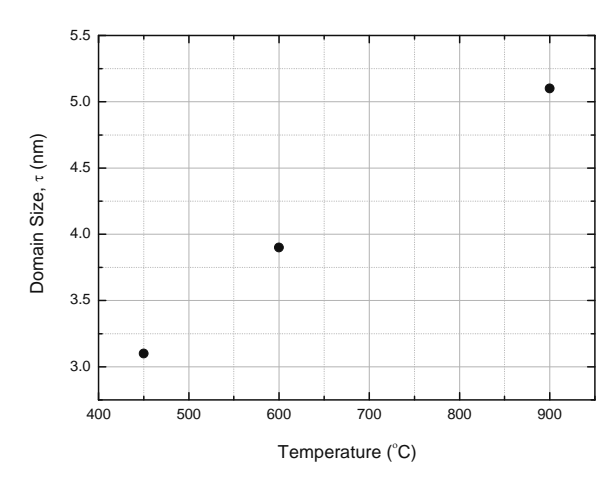


Figure 4.7 Domain size of sol-gel derived 8YSZ powders calcined at varied temperatures

Porous YSZ powders obtained from the polymeric sol through the processes of hydrolyzation, gelation and subsequent pyrolysis were characterized by N_2 adsorptions. As listed in Table 4.2, the specific surface area of 8YSZ powder calcined at 450 °C is 99 m²/g, almost twice as large as the 8YSZ powder fired at 600 °C with a value of 52 m²/g. The specific surface area of 3YSZ powder diminished from 81 m²/g to 11 m²/g as the calcination temperature increased from 450 to 600 °C.

powder	calcination	surface	mesopore (BJH model)		micropore (H&K model)	
composition	temperature	area	average	cumulative	average	cumulative
	(°C)	(m^2/g)	pore size	pore volume	pore size	pore volume
			(nm)	(cm ³ /g)	(nm)	(cm ³ /g)
8YSZ	450	99	2.4	0.061	0.9	0.046
8YSZ	600	52	<3.5	0.042	0.9	0.025
3YSZ	450	81	<10.8	0.009	< 0.8	0.037
3YSZ	600	11	3.5	0.014	< 0.6	0.006

Table 4.2 N₂ sorption results of YSZ powders derived from polymeric sol-gel route

The pore size distribution of powders derived from polymeric sol-gel route is shown in Figure 4.8. Thermally treated at 450 °C for 2 hours, the micropore size distribution is very narrow with an average micropore size of 0.9 nm. The average micropore size remained almost unchanged as calcination temperature was raised from 450°C to 600°C. In the contrast, the mesopore size distribution of 8YSZ powders is not well-defined and increased from 2.4 nm to 3.5 nm as the calcination temperature increased from 450 °C to 600 °C. The cumulative pore volume of 8YSZ powder calcined at

 $450\,^{\circ}\text{C}$ was $0.11\,\text{cm}^3/\text{g}$ and reduced to $0.07\,\text{cm}^3/\text{g}$ as the thermal treatment temperature increased to $600\,^{\circ}\text{C}$. The cumulative pore volume of 3YSZ powder calcined at $450\,\text{and}\,600\,^{\circ}\text{C}$ is $0.05\,\text{and}\,0.02\,\text{cm}^3/\text{g}$, respectively. The total micropore volume decreases and total mesopore volume increases in the whole process. The change in the total pore volume may suggest that the sintering process of the fine nanopowders have taken place at temperature as low as $600\,^{\circ}\text{C}$, which could also be evidenced by the dilatometric data demonstrated in section 4.1.5.

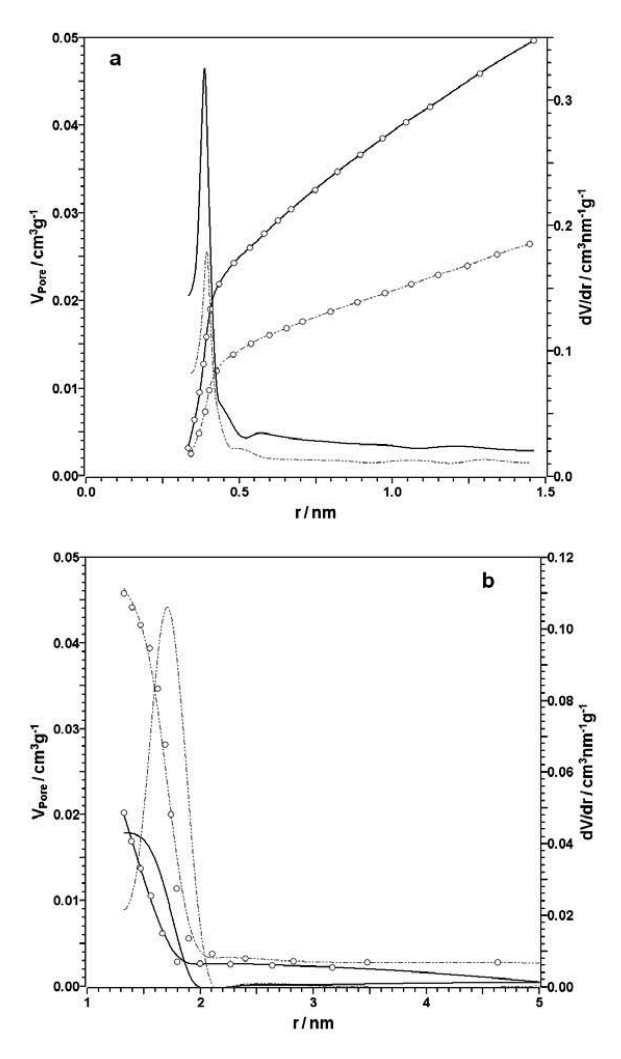


Figure 4.8 Pore size distribution plots derived from N_2 adsorption isotherms of 8YSZ powders synthesized by polymeric sol-gel route, thermally treated at 450°C (solid line) and 600°C (dash line): (a) micropore size distribution (H&K model), (b) mesopore size distribution (BJH model)

4.1.2 CGO, LSM and LSCF polymeric sols and derived powders

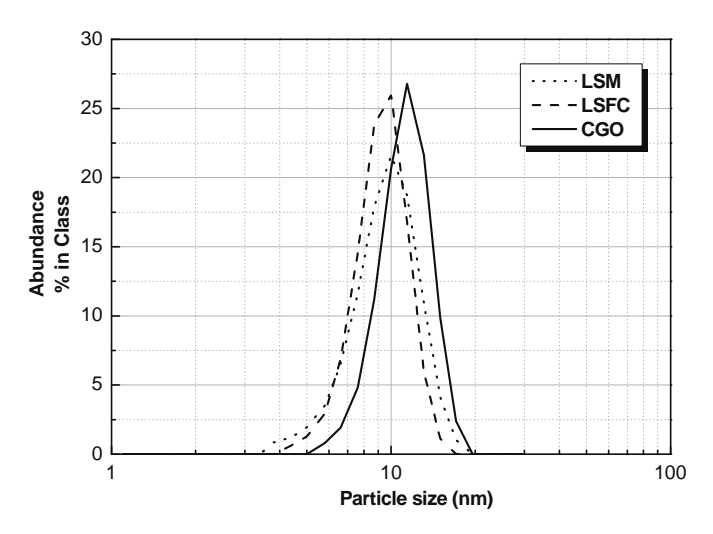


Figure 4.9 Particle size distribution of LSM, LSCF and CGO sols synthesized with acetates

Ce_{0.8}Gd_{0.2}O_{2- δ} (CGO), La_{0.8}Sr_{0.2}MnO_{3- δ} (LSM), and La_{0.58}Sr_{0.40}Co_{0.20}Fe_{0.80}O_{3- δ} (LSCF) sols were prepared from acetates and nitrates regarding their important applications as electrolyte or cathode materials in SOFC and gas-separation applications. The formation of a sol from acetates also involves two simultaneous chemical processes, hydrolysis and polymerization. As shown in Figure 4.9, the average particle size of 0.2 mol/L CGO sol is 11 nm, and the average particle size of 0.1 mol/L LSM sol and 0.1 mol/L LSCF sol are both 9 nm despite of different chemical composition.

Pale yellow $Ce_{0.8}Gd_{0.2}O_{2-\delta}$ powder was obtained by calcining the xerogel. According to X-ray diffraction analysis results in Figure 4.10, the powder was confirmed to be single phase solid solution with fluorite crystal structure and measured unit cell parameter of a=0.5430 nm (450 °C), a=0.5427 nm (600 °C), a=0.5426 nm (900 °C) and a=0.5422 nm (1200 °C). The slight decrease in lattice parameter might be caused by the facts that the atoms at the surface of the crystalline have longer covalent bond length than the atoms inside the bulk and the number of atoms located at the surface of the $Ce_{0.8}Gd_{0.2}O_{2-\delta}$ domain decreased as the grains grows larger at high calcination temperature, as illustrated in Figure 4.11.

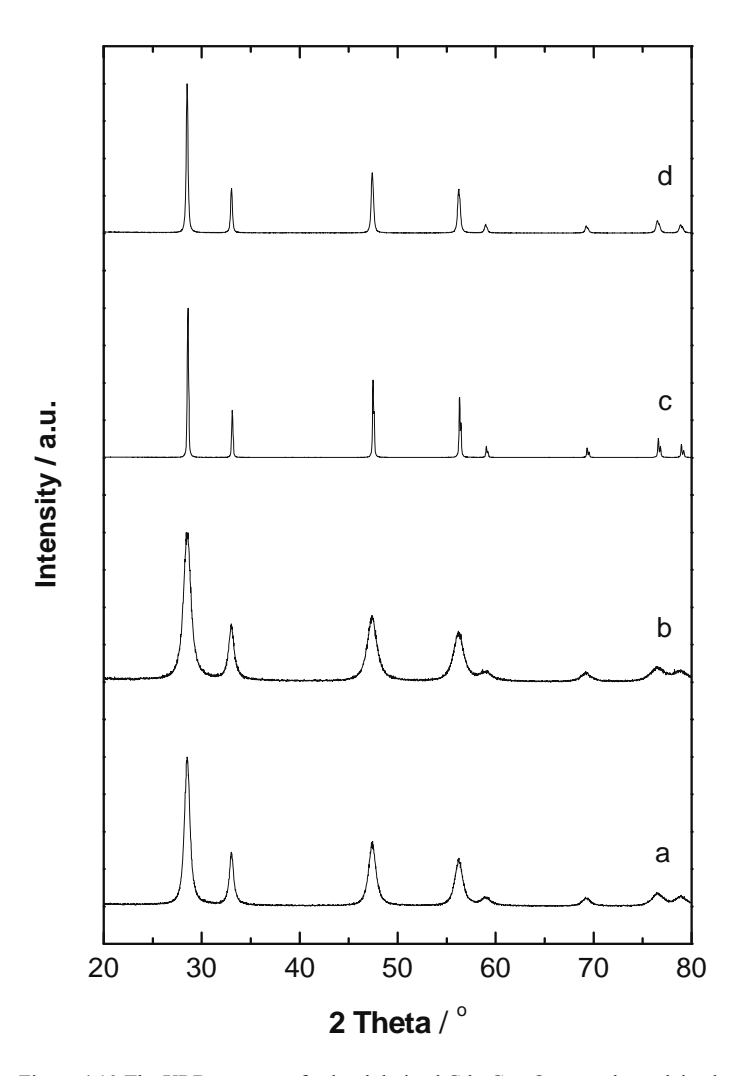


Figure 4.10 The XRD patterns of sol-gel derived $Gd_{0.2}Ce_{0.8}O_{1.9}$ powder, calcined at: (a) 450 °C, (b) 600 °C, (c) 900 °C, (d) 1200 °C

According to Scherrer equation [106], the average domain size (τ) of the powders thermally treated at different temperature is estimated to be 8 nm (450 °C), 11 nm (600 °C) and 126 nm (1200 °C), plotted in Figure 4.11. Considering the data as the approximation of the absolute domain size value, the tendency exhibits clearly a domain/particle growth with increasing thermal treatment temperature. Particularly, the XRD pattern of the CGO powder calcined at 900 °C sharply narrowed, indicating that a significant domain growth took place in the temperature range of 600 °C-900 °C, as shown precisely in Figure 4.10.

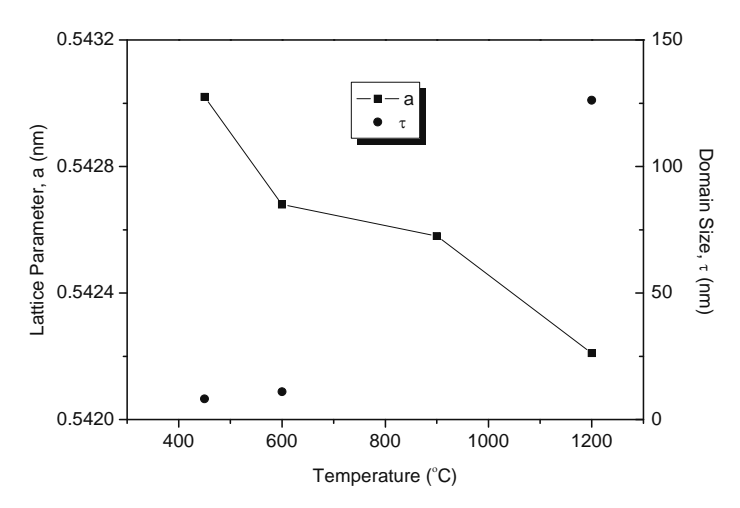


Figure 4.11 Lattice parameter and domain size of sol-gel derived CGO powder

4.1.3 8YSZ colloidal sols and derived powders

One of the most important advantages of preparing a ceramic layer from a synthetic sol-gel route is the flexibility in particle size distribution control, which means the particle size of the sol can be tuned and controlled in a continuous range (4 to 100 nm). The sol can be further applied to deposit layers or prepare fine ceramic powders. This idea can be perfectly demonstrated by the following preparation of 8YSZ sol from alkoxide precursors.

Zr-n-propoxide	Y-butoxide	DEA	Isopropanol	H ₂ O	0.05M HNO ₃	d_{50}
(mmol)	(mmol)	(g)	(ml)	(ml)	(ml)	(ml)
5.24	0.91	1.5	50	0	5	4
5.24	0.91	1.5	50	0	4.5	8
5.24	0.91	1.5	50	0	4	16
5.24	0.91	1.5	50	5	5	38
5.24	0.91	1.5	50	10	5	53
5.24	0.91	1.5	50	12.5	5	79

Table 4.3 Preparation conditions and d50 of colloidal 8YSZ sols synthesized from alkoxides

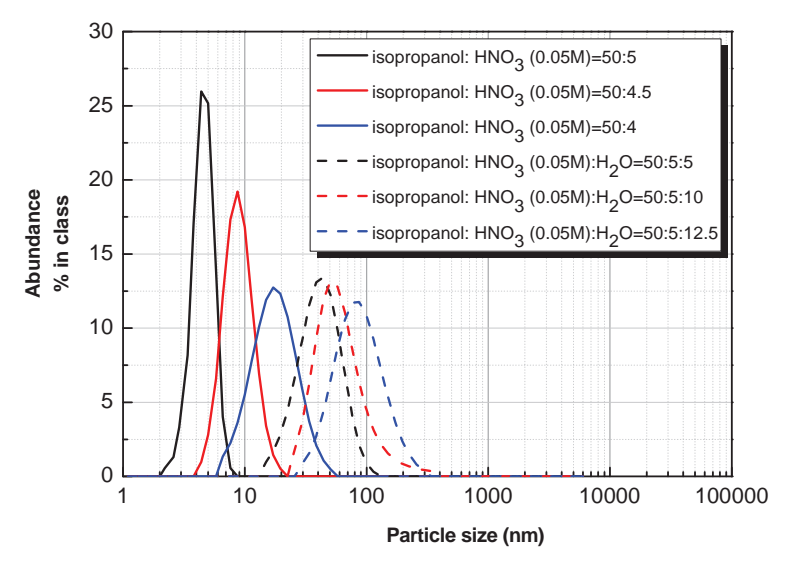


Figure 4.12 Particle size distribution of 8YSZ sol synthesized from alkoxide precursors. The Y³⁺:Zr⁴⁺ ratio was kept 16:92 by adding 5.24 mmol zirconium n-propoxide and 0.91 mmol Yttrium butoxide into 50 ml of isopropanol 1.5 g of DEA was used to modify the reactivity of the alkoxide

The Y³⁺:Zr⁴⁺ ratio was kept to 16:92, adding 5.24 mmol zirconium n-propoxide and 0.91 mmol yttrium butoxide into 50 ml of isopropanol. 1.5 g of DEA was also added to modify the reactivity of the alkoxide and avoid the precipitation of inhomogeneous hydroxide particles during the hydrolysis step. The particle size distribution of the sol was controlled by adjusting the amount of acid and water added into the reactants solution. As the isopropanol:HNO₃ (0.05M) ratio increased from 10:1 to 12.5:1, the d_{50} of particles in the sol increased from 4 nm to 16 nm. If additional water was added to the solution, the d_{50} of particles in the sol increased to the range of 30 nm to 80 nm. As an example, sol with d_{50} of 53 nm was prepared when the isopropanol: HNO₃ (0.05M): H₂O ratio was 10:1:2. As observed in Figure 4.12, the particle size increased significantly as more water was added into the system.

The time of peptization process is another important parameter to control the particle size distribution of the sol. In colloid chemistry, peptization is a particularly important process for the formation of stable sol of colloidal particles in water. By carrying electric charge, the colloidal particles mutually repel each others and cannot aggregate together. Peptization is widely used in synthesis of nanoparticles to make clustered

particles separated into many primary particles by changing the surface properties, applying a charge, or by adding a surfactant. In the synthesis of zirconia nanoparticles, peptization involves adsorption of charged molecules on the zirconia surface and causes the surface to become charged. Electrostatic repulsion of the primary particles in the agglomerated zirconia breaks up the agglomerate into primary particles.

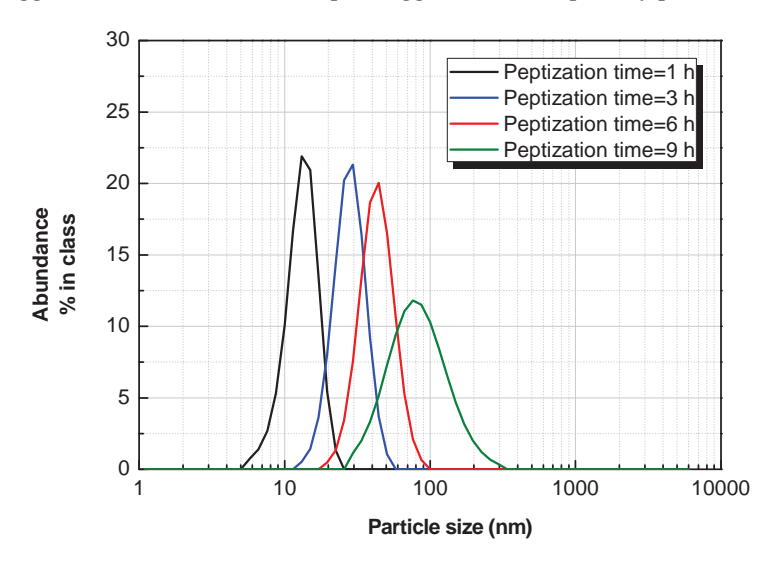


Figure 4.13 Particle size distribution of 8YSZ sol synthesized by zirconyl chloride octahydrate and yttrium nitrate hexahydrate

An alternative way to prepare particulate YSZ sol was the oxalate synthesis route by applying zirconyl chloride octahydrate, yttrium nitrate hexahydrate, oxalic acid dehydrate and distilled water as reactants. Particle size distribution of the as-prepared colloidal sols had a dependence on time of peptizing process. The average particle size varied from about 20 nm to several hundred nanometers. The size distributions of 4 representative sols are shown in Figure 4.13. With increasing peptization time, the particle size distributions tend to increasingly broadened and sols with well-defined particle size distribution (less then 40 nm) were prepared. The sols with particles of 20 nm to 50 nm are ideal for fabrication of intermediate YSZ layers on macroporous substrates if the drying cracks of the deposited layers can be avoided.

YSZ powders prepared from oxalate colloidal sol-gel route were characterized by N_2 sorption analysis. The data derived from the BET, BJH and H&K fits were summarized in Table 4.4. After peptization, drying and subsequent pyrolysis at

450 °C, the surface area of oxalate route derived 8YSZ powder is 37 m²/g, which is much smaller the specific surface area value ($100 \, \text{m}^2/\text{g}$) of the polymeric sol-gel derived powders calcined under the same condition. The specific surface area diminished by 40% to 22 m²/g after the powder was thermally treated at 600 °C for 2 hours. The specific surface area of 3YSZ powder prepared from colloidal sol reduced from 48 m²/g to 21 m²/g as the thermal treatment temperature increased from 450 to 600 °C.

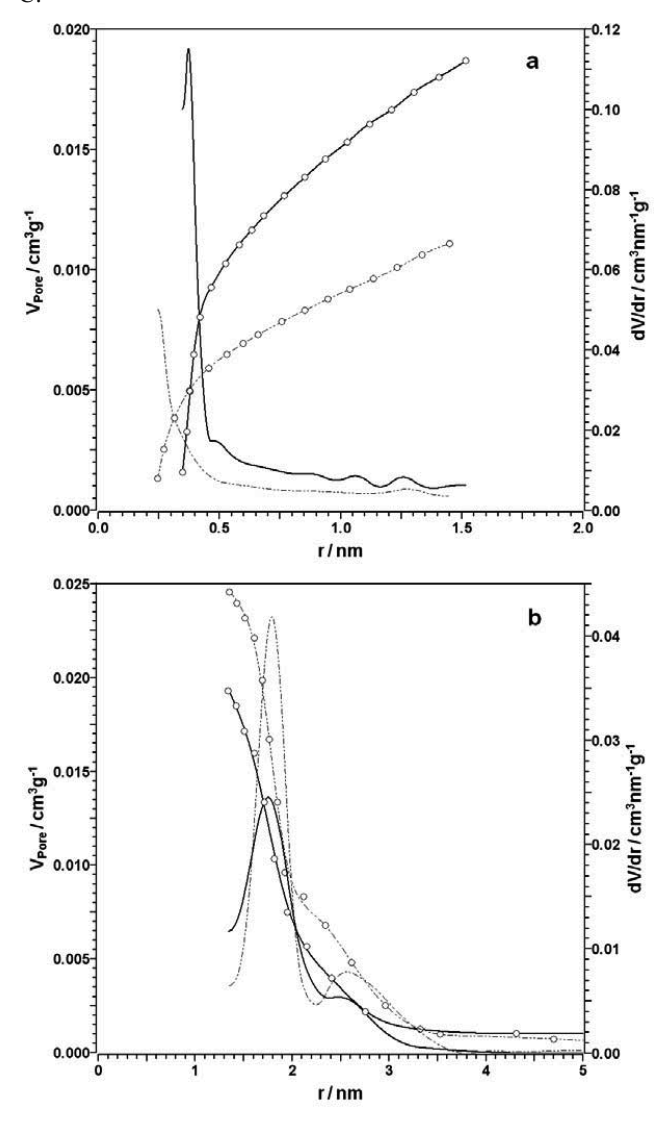


Figure 4.14 Pore size distribution plots derived from N_2 adsorption isotherms of powders made from colloidal sol-gel route, thermally treated at 450 °C (solid line) and 600 °C (dash line): (a) micropore size distribution (H&K model), (b) mesopore size distribution (BJH model)

powder	calcination	surface area	mesopore (BJH model)		micropore (H&K model)	
composition	temperature	(m^2/g)	average	cumulative	average	cumulative
	(°C)		pore size pore volume		pore size	pore volume
			(nm)	(cm ³ /g)	(nm)	(cm^3/g)
8YSZ	450	37	3.84	0.018	0.91	0.018
8YSZ	600	22	3.76	0.023	0.80	0.011
3YSZ	450	48	3.51	0.022	1.05	0.024
3YSZ	600	21	3.58	0.043	1.00	0.010

Table 4.4 N₂ sorption results of YSZ powders derived from colloidal sol-gel route

The pore size distribution of powders derived from oxalate sol-gel route was shown in Figure 4.14. Thermally treated at 450 °C for 2 hours, the average micropore and mesopore size was 0.9 nm and 3.8 nm, respectively. The pore size distribution of both micropores and mesopores remained almost unchanged as calcination temperature increased from 450 °C to 600 °C. In the process, the cumulative mesopore volume of as-prepared 8YSZ powder increased from 0.018 cm³/g to 0.023 cm³/g and the cumulative micropore volume decreased from 0.018 cm³/g to 0.011 cm³/g. Similar pore volume change was also observed with 3YSZ powder prepared in the same method. The cumulative mesopore volume of 3YSZ powder increased from 0.022 cm³/g to 0.043 cm³/g and the cumulative micropore volume decreased from 0.024 cm³/g to 0.010 cm³/g. The results here coincided with those of the powders prepared by the polymeric sol-gel route, indicating that the sintering process of powders synthesized with colloidal sol-gel route may also have already started at low temperature.

4.1.4 Nano-suspensions made of commercial oxide particles

Colloidal stabilized nano-suspensions with graded particle size distribution in the range of 40 nm to 160 nm were prepared through removing large particles and agglomerates by means of physical treatments. In high-performance centrifugation separation process, the rotation acceleration can be calculated as the product of the radius (r) and the square of the angular velocity (ω) . Regardless of equipment dimensions, relative centrifugal force (RCF) is the universal description of the acceleration applied to samples and it is described in units of gravity (g), as given by

$$RCF = r\omega^2/g = r(2\pi N)^2/g$$
 Equation 4.1

where g is gravitational acceleration of the earth, r is the rotational radius, N is the rotating speed, measured in revolutions per minute.

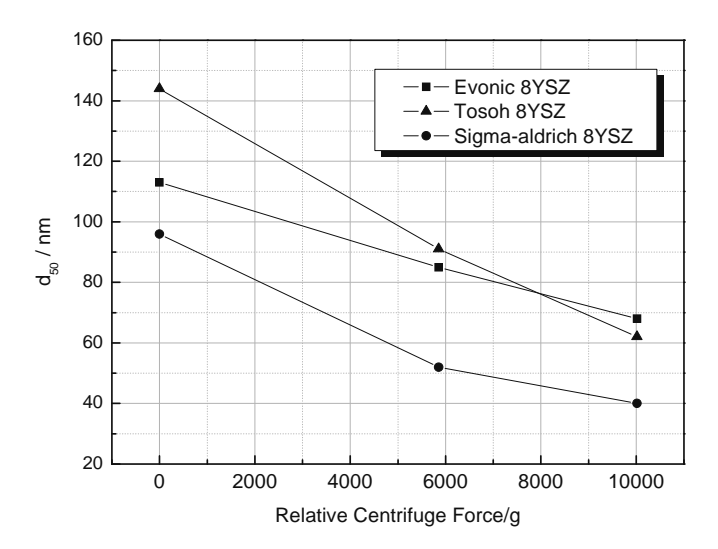


Figure 4.15 Dependence of particle size distribution on relative centrifuge force

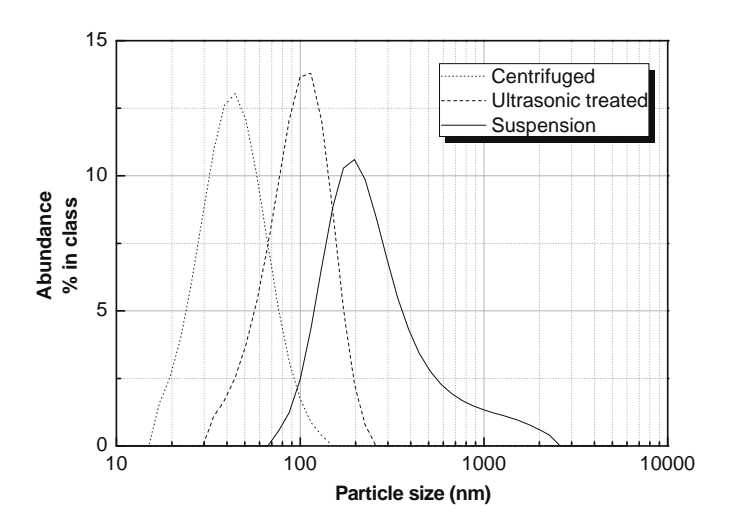


Figure 4.16 Particle size distributions of 8YSZ nano-suspensions made of Sigma-Aldrich powder

The average particle size and solid concentration of the 8YSZ nano-suspension is closely dependant on the relative centrifugal force (RCF). As demonstrated in Figure **4.15**, the d_{50} of the particles in the suspension, made of Tosoh 8YSZ powders, reduced linearly from 140 nm to 60 nm as the RCF increased, indicating the particle

size in the system is continuously distributed in the range of 60-140 nm. The loosely agglomerated particles in the suspension can be effectively broken by intensive ultrasonic treatment, as shown in Figure 4.16, the average particle size of suspension made of Sigma-aldrich 8YSZ powders sharply decreased from 220 nm to ~96 nm. As summarized in Table 4.5, the opaque milky suspension turned into a translucent sol by removing most large particles and hard agglomeration through the centrifugation process with RCF of 4000-6000 g, where g is the gravitational acceleration of the earth. Further increasing the RCF to 10000 g, the d_{50} of the particles in the sol slightly reduced to 40 nm and the sol turned from translucent into transparent state. Accordingly, the concentration of solid phase in the liquid became so low that the nano-suspension is no longer suitable for deposition of layer with sufficient thickness for SOFC applications.

RCF	d_{50} of sol made of Sigma-Aldrich 8YSZ powders	Physical appearance of
(g)	(nm)	the nano-suspensions
0	96	white, opaque
4000	52	translucent
5000	48	almost transparent
6000	45	almost transparent
7000	41	transparent
9000	40	transparent

Table 4.5 Particle size and physical appearance of 8YSZ nano-suspensions (made of Sigma-aldrich powders) centrifuged at different *RCF*

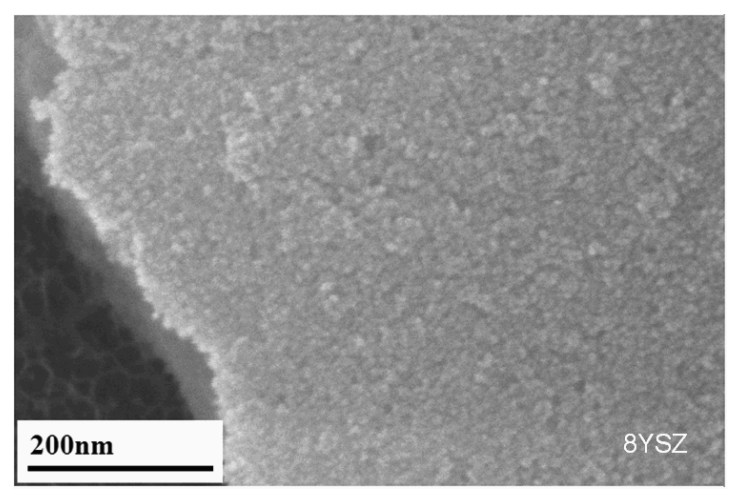


Figure 4.17 SEM image of dried Sigma-Aldrich 8YSZ powders on sample holder

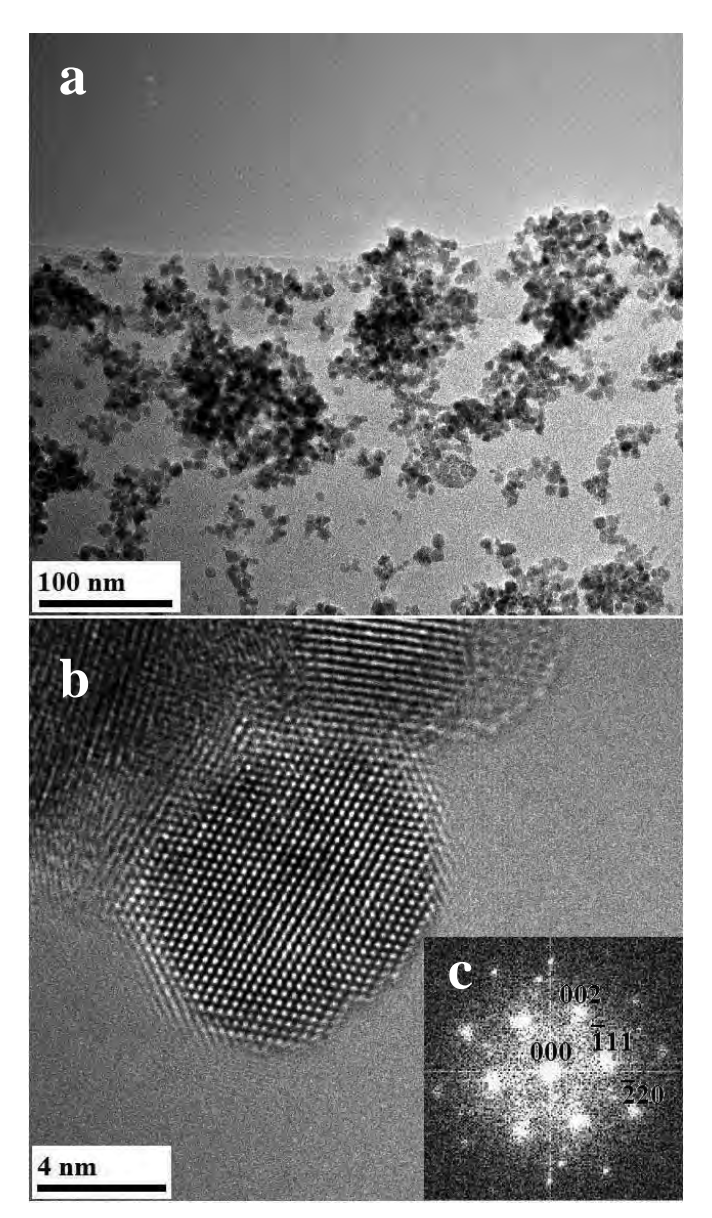


Figure 4.18 (a) TEM image of the Sigma-Aldrich 8YSZ nanoparticles, (b) high-resolution images of one single particle (c) the corresponding FFT images.

The actual primary particle size of the Sigma-Aldrich powders is only several nanometers, as shown in SEM image (Figure 4.17). It can be further confirmed in the TEM photograph (Figure 4.18a) that sphere nanoparticles with size of 5 to 10 nm and agglomerates with size of 20 to 100 nm are loosely dispersed on the carbon film of the

grid holder. As shown in Figure 4.18b, the single primary 8YSZ particle has a crystalline structure with a lattice constant close to the (111) plane (2.97 Å) of cubic ZrO_2 . Its simulated fast Fourier transform (FFT) image exhibited 002, $\bar{1}11$ and $\bar{2}22$ diffraction spots, which corresponded to the cubic ZrO_2 crystal with the [110] incident direction, as seen in the Figure 4.18c.

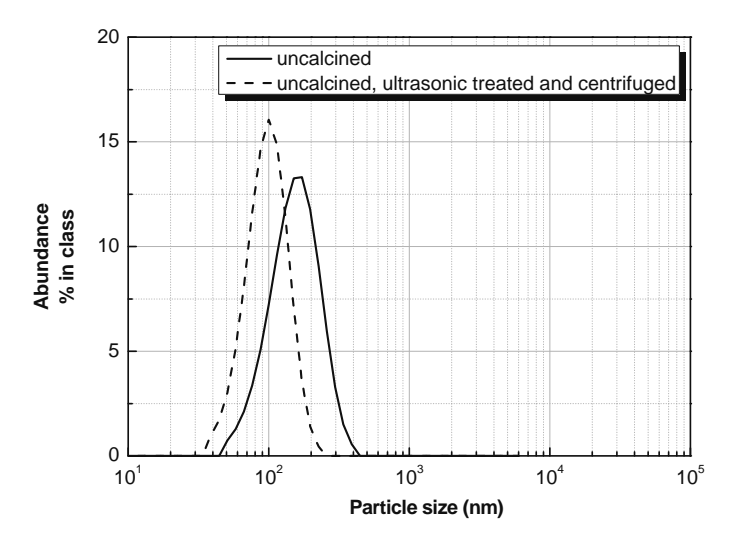


Figure 4.19 Particle size distribution of suspension made from Tosoh 8YSZ powders

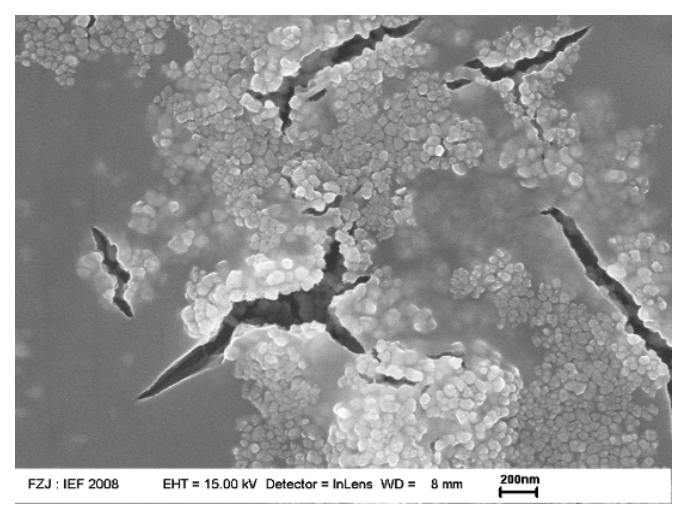


Figure 4.20 SEM image of dried uncalcined Tosoh 8YSZ powders on sample holder

The average particle size of uncalcined Tosoh 8YSZ powder used in this work is about 150 nm. By removing large particles and agglomerates through ultrasonic and centrifugation treatments, the average particle size of the aqueous suspension made from Tosoh 8YSZ powders is reduced to ~90 nm (Figure 4.19), which is in good agreement with the primary particle size observed in SEM image (Figure 4.20).

4.1.5 Results of dilatometric measurements

The densification and thermal displacement of pellets made from the three different 8YSZ powders are shown in Figure 4.21 and the dilatometric data are summarized in Table 4.6 respectively. The sinter process of pellets made of Tosoh 8YSZ powder starts at temperature of 1000 °C and the maximum sinter rate is 8x10⁻⁵ s⁻¹ at 1310 °C. The final sintered samples have yielded a relative density of 99%, which is measured by the Archimedes method.

Powder	sinter	max.	max.	green	sintered	relative
	start temp.	sinter rate	sinter rate at	density	density	sintered
	(°C)	(s ⁻¹)	(°C)	(g/cm ³)	(g/cm ³)	density
PS 8YSZ	652	1.7×10 ⁻⁵	1125	2.47	5.33	89.7%
CS 8YSZ	827	2.7×10 ⁻⁵	1129	2.68	5.44	91.6%
Tosoh 8YSZ	954	8.0×10 ⁻⁵	1310	2.52	5.88	99.0%

Table 4.6 Summary of dilatometric data for 8YSZ

The measurable shrinkage of the pellets made from polymeric sol-gel derived 8YSZ powder (PS 8YSZ) began at 650 °C, about 300 °C lower than the sinter starting temperature of Tosoh 8YSZ powder (TZ-8Y). At about 1130 °C, the sintering speed reaches the maximum value of $1.7x10^{-5}$ s⁻¹. The sintered pellets yielded a relative density of 90%. Similarly, the measurable shrinkage of pellets made of oxalate sol-gel route derived 8YSZ powder (CS 8YSZ) started at around 830 °C and the sintering process of the pellets ended up with a relative density of 92%. The maximum densification speed of $2.7x10^{-5}$ s⁻¹ was also reached at around 1130 °C.

Considering that the green density of the samples is very close to each other, the packing density of the pellets should not have played a crucial role in the finally sintered density. The comparatively low sintered density of the samples prepared with

sol-gel derived powders may result from other reasons, such as inhomogeneous agglomerates, pore entrapment, and non-uniform shrinkage or grain growth. Although the sintered pellets made from sol-gel derived powders showed low relative sintered density, the sol-gel film or thin layer could still be fully densified, if the green density of the layer is substantially increased under the capillary force exerted by porous substrates.

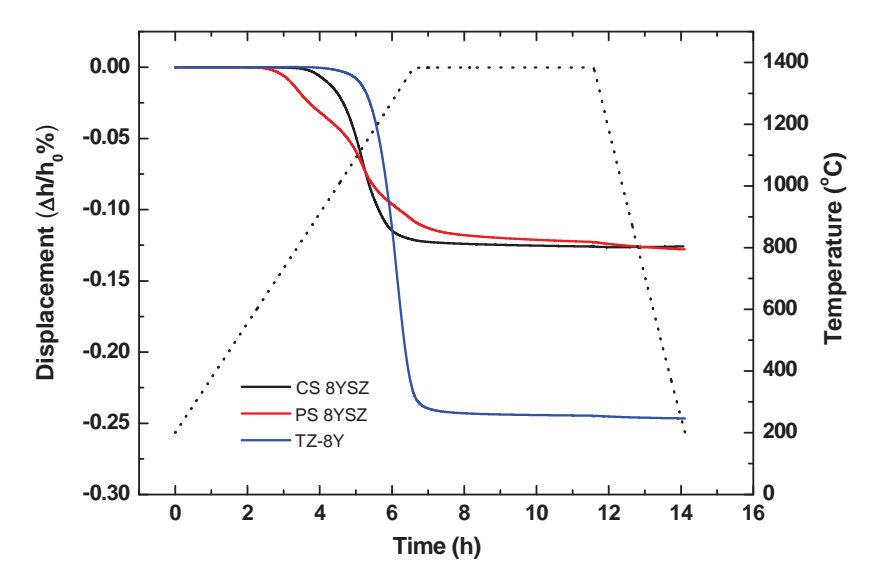


Figure 4.21 Densification plots of 8YSZ during heat cycle

4.2 Characterization of layers

4.2.1 Substrates

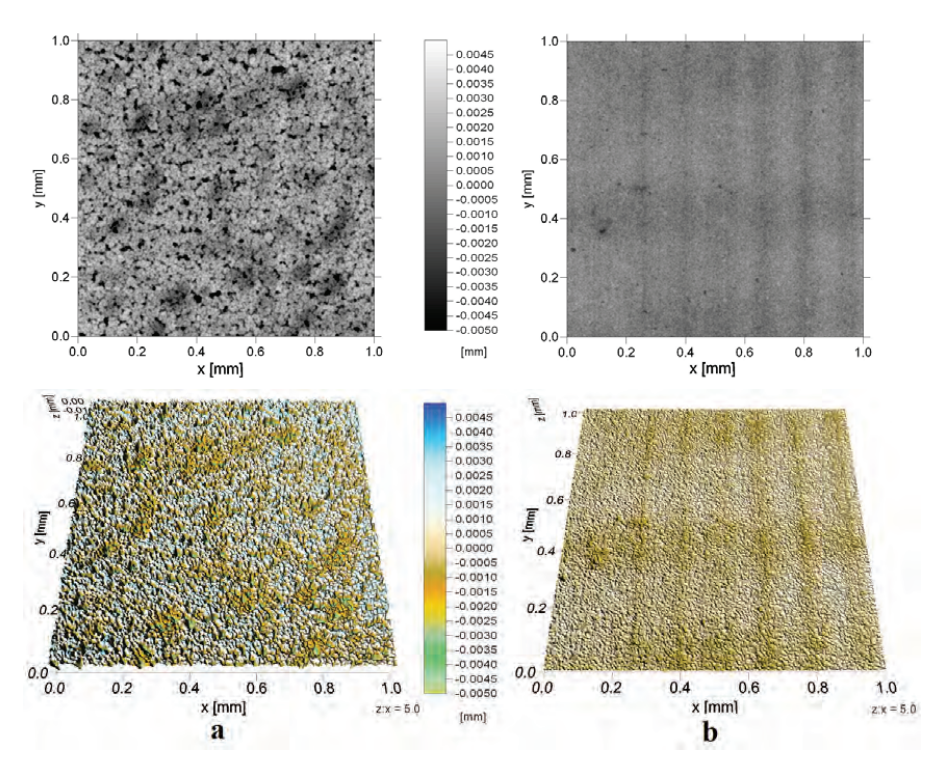


Figure 4.22 Topography of porous anode substrates, pre-sintered at 1230 °C for 3 hours: (a) warm-pressed substrate, (b) tape-cast substrate

Typical topographies of warm-pressed and tape-cast cermet anode supports were obtained by Cyber Scan CT200 non-contact laser scanning inspection system. As demonstrated in Figure 4.22, the surface of the tape-cast substrate is smoother than the surface of warm-pressed substrate. There are pores with size of $10{\sim}50~\mu m$ spreading all over on the surface of the warm-pressed anode support. On the contrast, it can be seen in the SEM image (Figure 4.23) that the surface of tape-cast substrates are dominated much smaller pores (<5 μm). The roughness data of polished and unpolished samples are comparable in Table 4.7. Although the overall average roughness (Sa) is reduced by polishing, the local roughness (peak to valley height) remains almost unchanged.

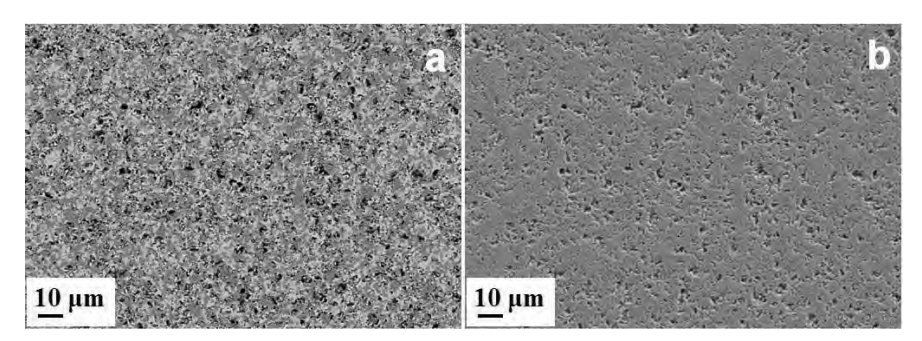


Figure 4.23 SEM surface image of polished FG02 tape-cast anode substrates, finally sintered at 1400 °C for 5 hours: (a) backscattered electron, (b) secondary electron image

Sample	Average	Peak	Valley	Peak to valley
	roughness	height	depth	height
	(µm)	(µm)	(µm)	(µm)
FZJ FG02 substrate unpolished	1.5	11.9	14.6	26.4
FZJ FG02 substrate polished	0.6	14.5	11.3	25.9

Table 4.7 Roughness data of FG02 tape-cast anode substrates, finally sintered at 1400 °C for 5 hours

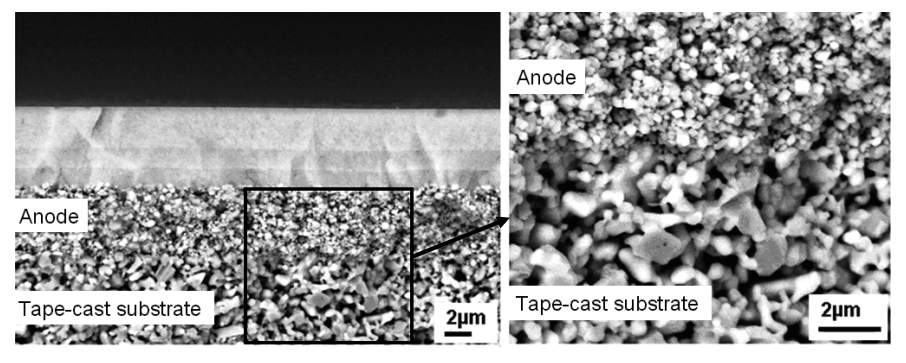


Figure 4.24 Pore structure of tape-cast substrate and screen-printed anode layer

Vacuum-slip-cast or screen-printed anode layers are coated with fine particles (d_{50} <0.4 µm) to reduce the substrate surface roughness and pore size distribution of the substrate. By covering the micron-sized pores, the anode layer served as the first intermediate layer supporting the electrolyte deposited with fine 8YSZ particles. As clearly shown in Figure 4.24, the pores and particles in the anode layer are in the range of 50 to 300 nm, significantly smaller than the micron-sized pores and particles in the tape-cast substrate.

4.2.2 Layers deposited with polymeric sols

4.2.2.1 Layers spin-coated on silicon wafer

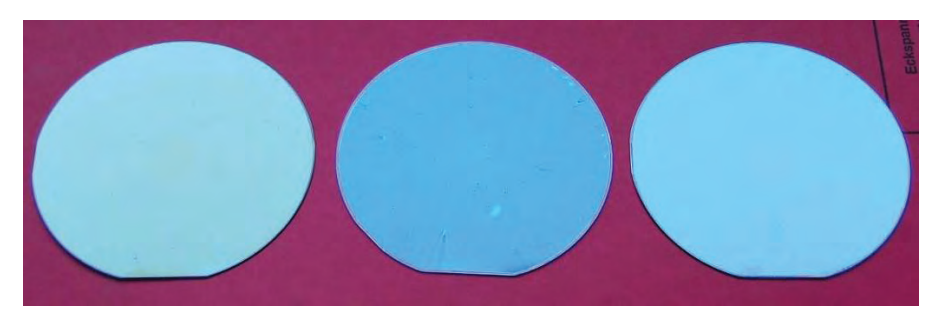


Figure 4.25 ZrO₂, 3YSZ and 8YSZ thin layers deposited on silicon wafers

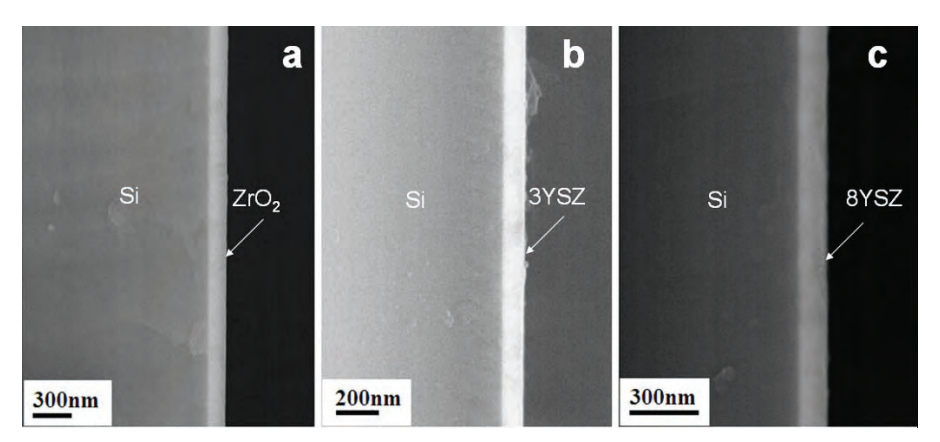


Figure 4.26 Fracture surface SEM of ultrathin zirconia layers coated by polymeric sol

ZrO₂, 3YSZ and 8YSZ polymeric sols with concentration of 0.155 mol/L were directly used for deposition thin layers on silicon wafers via spin coating. The asprepared polymeric sol showed excellent layer formation properties and the deposited precursor layers transformed into crack-free ultra thin ceramic layers by intermediate temperature calcination process at 450 to 600 °C (Figure 4.25). If it is not specially mentioned, all the samples described in this section were thermally treated with a heating rate of 100 K/h and dwelling time of 1 h, regardless of the final calcination temperature.

As shown in fracture surface SEM images (Figure 4.26), the thickness of as-deposited ceramic layers was approximately 100-150 nm, with a nicely coverage on the silicon

wafer. Defects, such as pin-holes or cracks are not observed in SEM surface images of the layers (Figure 4.27). Calcined at 600 °C for 2 h, the grain size in the layers with varied phase composition is in the range of 5 to 10 nm, as viewed in Figure 4.28.

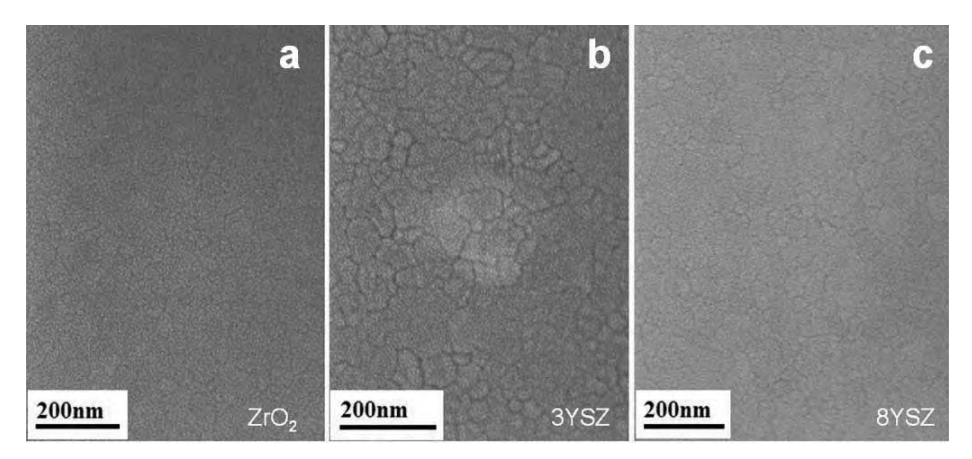


Figure 4.27 Surface SEM of ultrathin zirconia layers coated by polymeric sol on silicon wafers

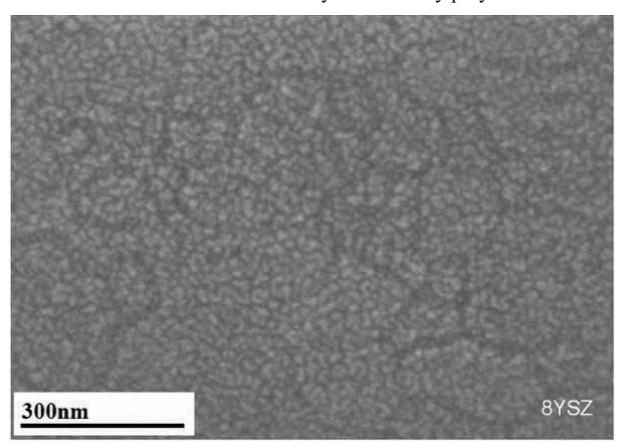


Figure 4.28 Surface SEM of ultrathin 8YSZ layer coated by polymeric sol on silicon wafers

4.2.2.2 Layers spin-coated on finally sintered anode substrate

Spin-coated sol-gel layer was then prepared on non-shrinking FG02 tape-cast anode substrates, which were finally sintered at 1400 °C with a heating rate of 180 K/h for 5 h. An ultra thin transparent layer of around 100 nm was formed following the topography (ups and downs) of the surface of unpolished tape-cast substrates (Figure 4.29a). The polymeric sol could also flow into pores and form a thicker layer or infiltrate into the connected pore channels. The top view of the layer showed that the pin-holes with size less than 1 µm have formed inevitably in the transparent layers

due to the rough topography of the substrates (Figure 4.29b). These results proved again the necessity to deposit intermediate layers to support a dense sol-gel electrolyte layer and to avoid formation large defects.

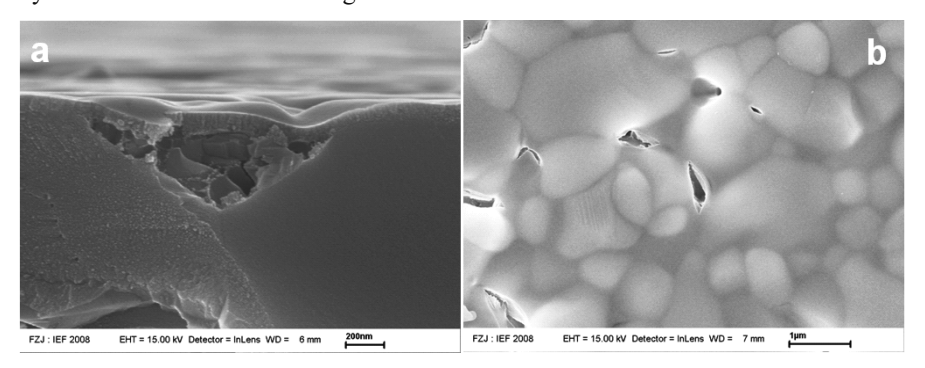


Figure 4.29 SEM images of 8YSZ layer by spin coating polymeric sol on finally sintered tape-cast anode supports, fired at 600°C: (a) fracture surface (b) surface

4.2.2.3 Layers spin-coated on sintered electrolyte

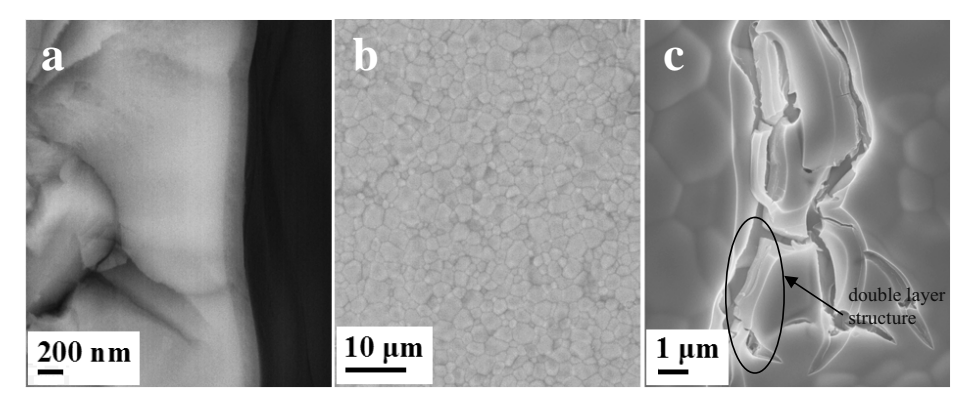


Figure 4.30 SEM images of spin-coated 8YSZ layer with polymeric sol on the surface of sintered electrolyte, fired at 600°C: (a) fracture surface (b) surface (c) cracks in the layer

Similarly, the polymeric sol also showed good layer forming behaviour on the sintered electrolyte. Twice spin-coated with the as-prepared 0.31 mol/L polymeric sol and calcined at 500 °C, a transparent 8YSZ layer of 150 nm in thickness was formed (Figure 4.30a). The micron-sized grains of the sintered electrolyte under the transparent sol-gel derived layers can be clearly seen in Figure 4.30b and a double-layer structure is observed in Figure 4.30c, where cracks in the layer are located. In the electrochemical point of view, the interface between the two layers should be removed by sintering the layers at high temperature to avoid polarization resistance.

Grain boundaries should be minimized to enhance the oxygen ion migration rate of the layer by increasing the grain size, because the grain boundary normally has much higher resistance than the bulk material.

The microstructure evolution of the thin layers related to thermal treatment temperature is demonstrated in Figure 4.31. First of all, no grain is visible in the SEM picture of the sample calcined at 500 °C for 1 h Figure 4.31a. However, the grains in the as-prepared layers grew from around 30 nm to over 100 nm as the calcination temperature increased from 800 to 1040 °C with dwelling time of 1 h, which are also the typical substrate temperature for deposition of the CGO barrier layer and the calcination temperature for LSCF cathode in the single cell manufacturing process. It is clearly observed that the layer is over-sintered and finally developed into a maroporous layer with pore size larger than 50 nm, seen in Figure 4.31d.

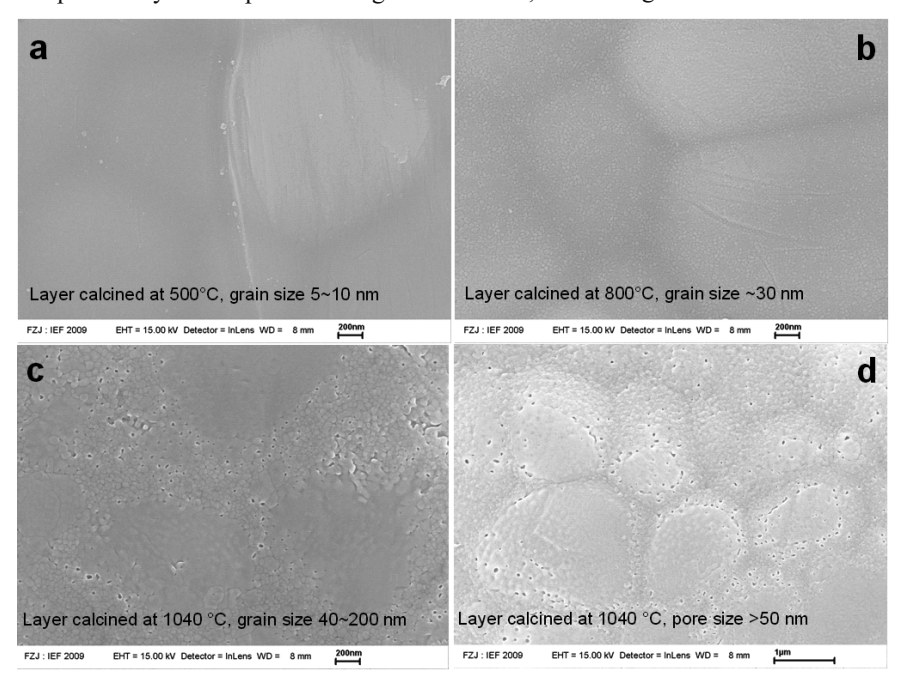


Figure 4.31 Evolution of polymeric sol-gel derived 8YSZ layer

4.2.3 Layers deposited with nano-suspensions

4.2.3.1 Concept of hybrid PVA-ceramic layers

Nontoxic and odorless polyvinyl alcohol (PVA) has excellent film forming, emulsifying, and adhesive properties. According to the work of T.A. Peters et al. [112], thin PVA membrane can be formed on porous ceramic support. In principle, the method described in this work for fabricating thin electrolyte with colloidal sol or nano-suspension has three steps: 1. Hybrid PVA membrane is formed with fine oxide (YSZ or CGO) particles distributed and fixed in the dried PVA membrane (Figure 4.32a); 2. PVA is totally decomposed and removed in thermal process above 200°C and porous YSZ and CGO ceramic layers are formed on the substrate (Figure 4.32b); 3. Porous ceramic layers are sintered at higher temperature forming dense ceramic layers (Figure 4.32c). In the process, PVA played a crucial role to minimize the infiltration of the particles into the pores of the substrate. A PVA network consisting of numerous monomers connected and fixed the oxide particles in the hybrid membrane and prevented formation of inhomogeneous layers by preventing segregation of the oxide particles.

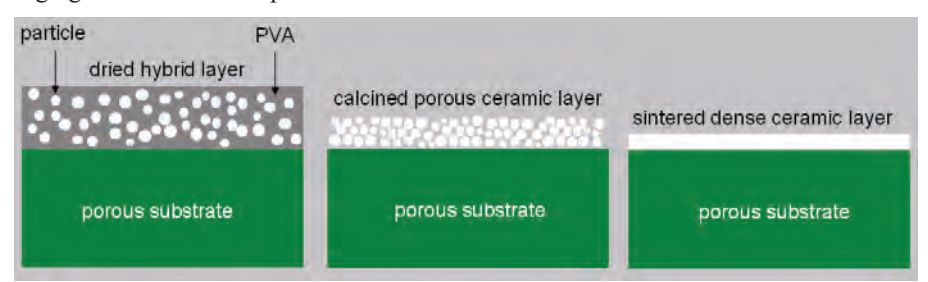


Figure 4.32 Formation of ceramic layers from hybrid layers: (a) dried hybrid layer, (b) porous ceramic by decomposition of PVA; (c) dense ceramic layer by sintering process

4.2.3.2 Layers deposited via dip-coating method

Homogenous 8YSZ layers with thickness of 1 to 6 μm were successfully fabricated on tape-cast substrate by repeating dip-coating and thermal treatment processes, seen in Figure 4.33. PVA solution was added into the nano-suspensions as binder and drying control chemical addictives. The multilayer structure was recognizable after calcination of the layers at 500 °C for 1 h. In the SEM image of a triple-layered coating in Figure 4.34a, sharp 8YSZ/8YSZ interfaces are observed. When the

underlying layer is porous, intermixing of the layers may occur. Such interpenetration process may aided by the capillary pressure created by solvent flow into the underlying porous layer [82]. By increasing the solid concentration of the sol or nanosuspension, the single layer thickness in a calcined state increases from 1 to 2 μ m. As demonstrated in Figure 4.34a, the third layer coated with nano-suspension of doubled solid concentration shows a doubled layer thickness compared to the first and second coated layer.

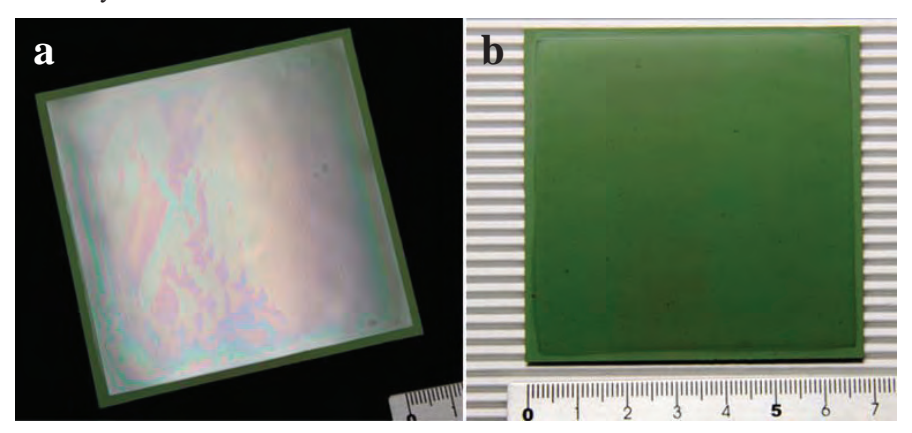


Figure 4.33 Half-cells with dip-coated 8YSZ layer, FG02 anode support with screen-printed anode as substrate: (a) 8YSZ layer calcined at 500 °C, (b) 8YSZ layer sintered at 1400 °C

The surface SEM image in Figure 4.34c shows that the grain size of the sample calcined at 500 °C remained in nanometer regime (approximately 5-10 nm). The calcined layers are not permeable by propanol (propanol-tight) and suitable for supporting polymeric sol-gel layer by avoiding serious the sol infiltration. As the thermal treatment temperature of the layer increased to over 700 °C, significant grain growth took place and the pore structure of the nano-suspension layer was changed. The layers were not propanol-tight anymore. The samples sintered at 1400 °C are fully dense and the average grain size of the layer made of nano-suspension is lager than 1 μ m, as shown in Figure 4.34b,d. By comparing of the fracture surface images, it is found that the layer thickness shrinked from 6 to 3.5 μ m, during the transformation process of the layer from the calcined state to the final sintered state. The visible grain boundary in Figure 4.34b proved that the as-prepared electrolyte has normally only one single grain, with size larger than 2 μ m, packed in the vertical direction to the sample plane. In the single SOFCs prepared with such electrolyte, the

oxygen ions do not need to cross more than one grain boundary in the electrolyte to reach the reaction site at anode side during cell operation.

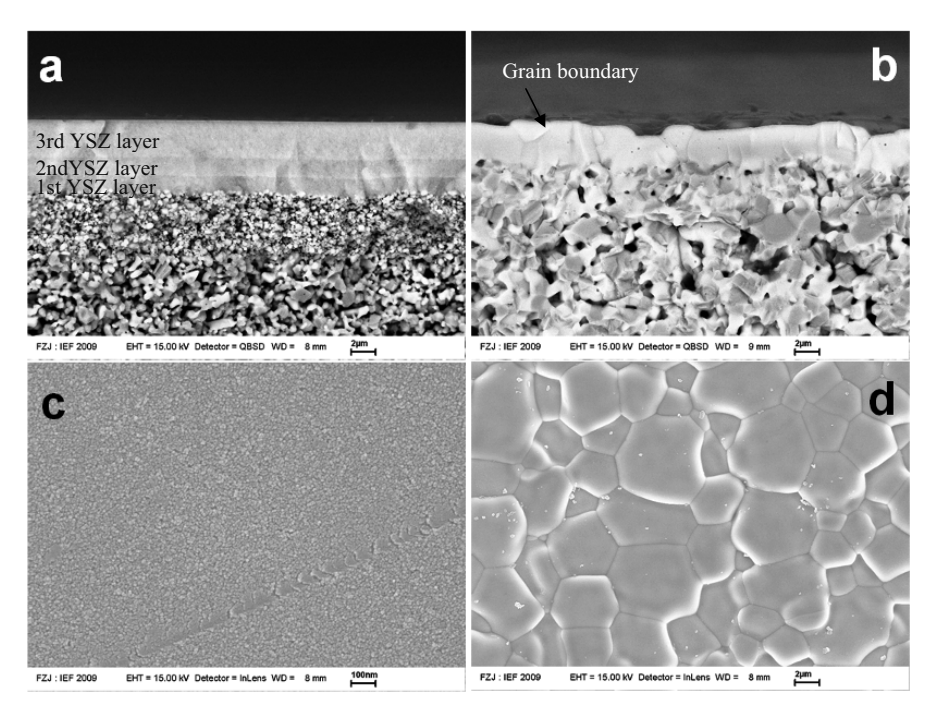


Figure 4.34 SEM images of dip-coated 8YSZ layer with colloidal sol/suspension on tape-cast substrates with screen-printed anode layer: (a) fracture surface, calcined at 500 °C for 1 h, (b) fracture surface, sintered at 1400 °C for 5 h, (c) surface, calcined at 500 °C for 1 h, (d) surface, sintered at 1400 °C for 5 h

Layers thicker than 5 μ m were deposited by increasing the solid concentration of the sol or suspension or repeating the coating cycles. Although the thick layers remains crack-free after the calcinations at 500 or 600 °C for 1 h, massive cracks are found in the sintered electrolyte. The layer even delaminate from the substrate at the edge of the coated layer, as shown in Figure 4.35a. A drying frontier may form in the coated layer if the sol dried before reaching the edge of the substrate. The local thickness of the layer on the drying line is normally thicker due to the existence of a large contact angle at the solid/liquid/gas interface. Cracks are found on the drying line when the local layer thickness on the line exceeds the critical thickness for the formation of crack-free layers, as shown in Figure 4.35b.

In order to increase the green density and 8YSZ material load of the electrolyte layers, a multi-temperature calcination process was investigated. The first dip-coated layer was calcined at 1000 °C for 1 h to enlarge the pore size of the layer. During the formation of the second layer, the fine particles may fill into the pores of the first layer increasing the packing density of the double-layer electrolyte. The second layer with intermediate pore size was formed by a calcination process at 800 °C for 1 h, instead of forming a propanol-tight mesoporous layer by a calcination at 500 °C. In the next step, the polymeric 8YSZ precursor layer forms on the top of the intermediate 8YSZ layer with partly infiltration of the precursor polymeric sol into the porous intermediate layers, resulting in an additional enhancement of the electrolyte green density prior the final sintering step.



Figure 4.35 Cracks in electrolyte layer prepared by dip coating: (a) crack in sintered electrolyte with over-critical thickness (substrate in oxidized state), (b) cracks on the drying frontier (substrate in reduced state)

4.2.3.3 Helium leak rate

The layers, deposited with colloidal nano-suspension and calcined at 500 °C, is propanol-tight and with well-defined pore structure and grain size, which is suitable to serve as an intermediate layer and support the propanol-based polymeric sol to form a thin layer on the top by limiting sol infiltration into the supports. The fine pore structure of the propanol-tight intermediate layer is destroyed by the thermal treatment at temperature over 800 °C due to significant grain growth. Micro-porous structure in the layer was replaced by meso-/macro-porous structure, which were not able to prevent the polymeric sol from infiltrating into the layer. The as-deposited

layers can be fully sintered at 1400 °C for 5 h with micron-sized grains. Finally the sinter samples were reduced in H_2/Ar at 900 °C and the 8YSZ layer remained dense.

Samples with polymeric-sol-derived layers on top the porous intermediate layer proved to be moderate gas-tight with rather low helium leak rate in the range of 5.3×10^{-5} to 4.6×10^{-3} hPa·dm³·s⁻¹cm⁻², shown in Figure 4.36. The leak rate is supposed to be strongly influenced by the defect in the layer. As the thermal treatment of temperature of the layers increased to over 700 °C, the helium leak rate of the 8YSZ layer increased significantly due to microstructure change in the overly sintered polymeric-sol-derived layer as described in section 4.2.2 and demonstrated in Figure 4.31. The helium leak rate of half-cells with dip-coated and sintered 8YSZ electrolyte layers are in the range of 8×10^{-6} to 5×10^{-5} hPa·dm³·s⁻¹cm⁻². The helium leak rate of the same samples exceeded 7×10^{-4} hPa·dm³·s⁻¹cm⁻² after the reduction of anode substrate in Ar/H₂ at 900 °C.

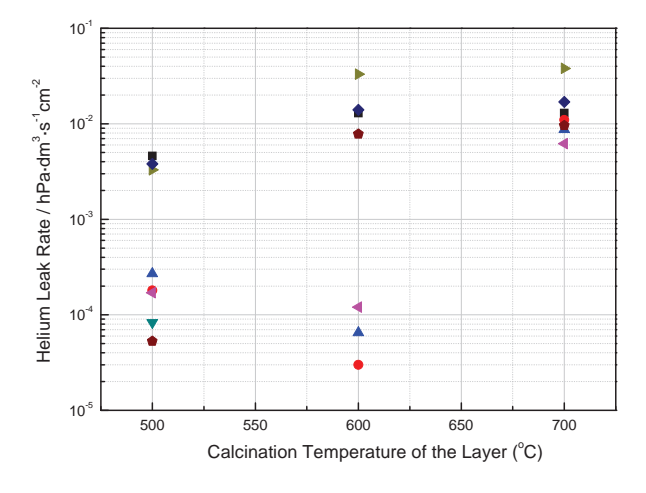


Figure 4.36 Helium leak rate of samples prepared on tape-cast substrates with calcined 8YSZ layer

4.2.3.4 Layer thickness and microstructure

The dip-coating processes were carried out for 1-3 times with fixed solid concentration in nano-suspension. As shown in Figure 4.37 and Figure 4.38, the thickness of as-prepared increased steadily and the thickness of 3-times dip-coated zirconia and ceria layers is 2.7 and 3.5 µm, respectively. According to the SEM surface images, the zirconia and ceria layers remains porous and incompletely

densified after firing at 1200 °C and 1300 °C for 2 hours (Figure 4.39a, b and Figure 4.40a,b). The pores in the layers gradually diminished and the average grain size of the layer steadily increased as the thermal treatment temperature of the sample increased. The SEM images of finally sintered layers are shown in Figure 4.39c and Figure 4.40c. The grain size of ZrO_2 layer sintered at 1400 °C for 2 hours remains in sub-micron regime, while the 8YSZ layer sintered at 1400 °C for 5 hours normally has the grain size of several microns. In the case of ceria coatings, the grains in the layers grew from around 300 nm to over 1 μ m as the thermal treatment temperature rose from 1200 to 1400 °C, with dwelling time of 2 hours.

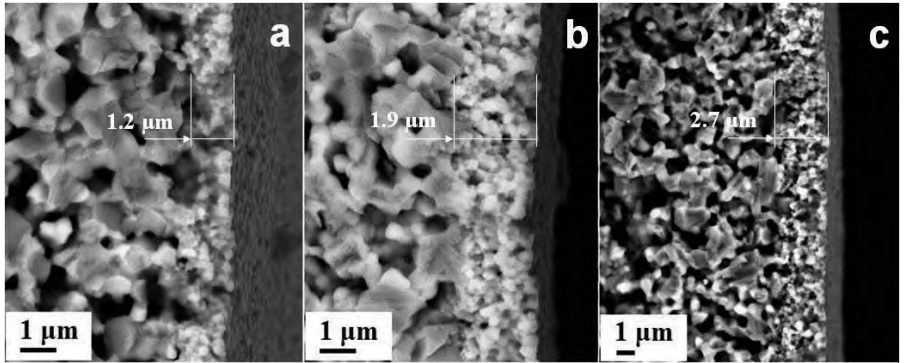


Figure 4.37 SEM fracture surface images of dip-coated zirconia layers on anode support, fired at 1200 °C for 2 h: (a) dip-coated 1 time, (b) dip-coated 2 times, (c) dip-coated 3 times

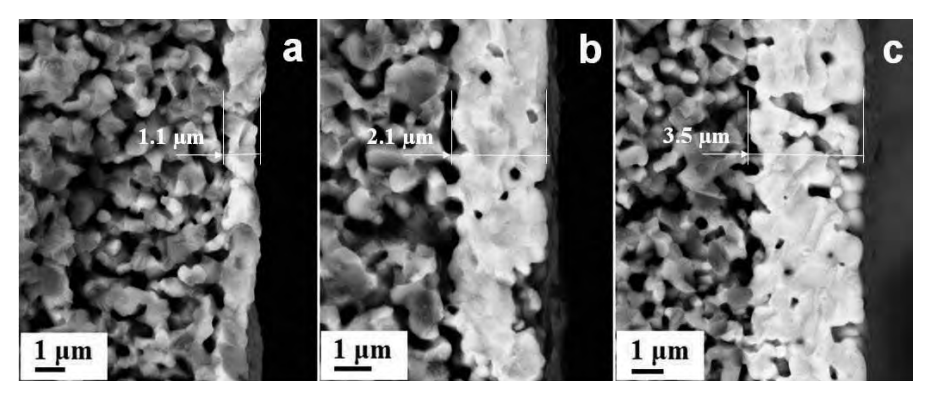


Figure 4.38 SEM fracture surface images of dip-coated ceria layers on anode support, fired at 1300 °C for 2 h: (a) dip-coated 1 time, (b) dip-coated 2 times, (c) dip-coated 3 times

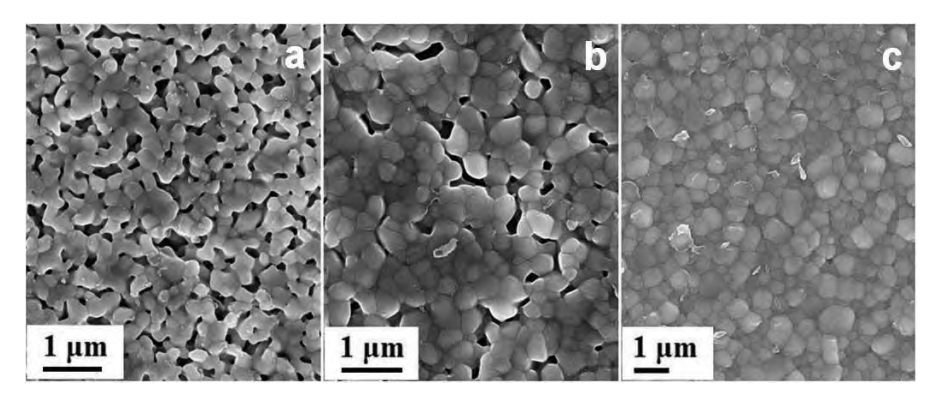


Figure 4.39 SEM surface images of zirconia layers on porous AFL, fired at: (a) fired at 1200 °C for 2 h, (b) fired at 1300 °C for 2 h, (c) fired at 1400 °C for 2 h

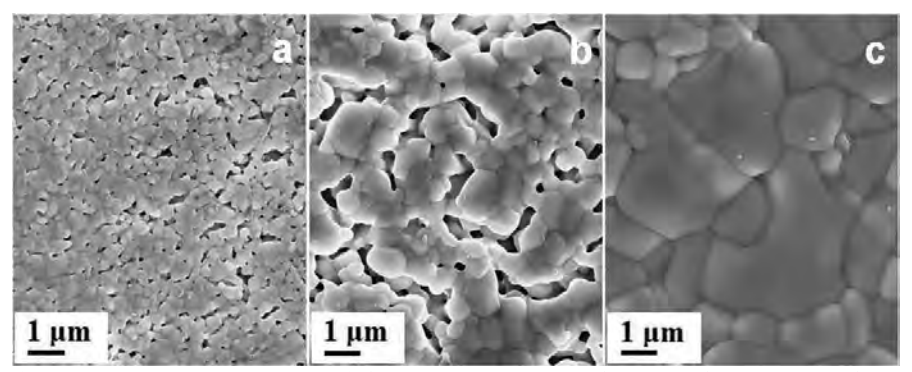


Figure 4.40 SEM surface images of ceria layers on porous AFL, fired at: (a) fired at 1200°C for 2 h, (b) fired at 1300°C for 2 h, (c) fired at 1400°C for 2 h

4.2.3.5 Curvature

The samples with sintered zirconia or ceria layers prepared on 1 mm thick warm-pressed substrates or 0.6 mm thick tape-cast substrates showed curvatures after sintering at 1400 °C for 5 h. Curvatures are observed in the 3-dimensional topography images monitored by the senor DRS 8000 on Cyber Scan CT200 laser scanning system.

	Layer thickness Deflect		x-axis profile through	y-axis profile through	
	(µm)	(mm)	center, curvature (m ⁻¹)	center, curvature (m ⁻¹)	
a	1 μm	0.96	0.11	0.17	
b	2 μm	0.17	-8.86	-9.50	
С	3 μm	0.48	-23.62	-20.81	

Table 4.8 Bending results of sintered ceria layers on 1 mm thick warm-pressed anode substrates

In the first experiment, square-shaped warm-pressed anode substrates (1 mm thick) pre-sintered at 1230 °C for 3 h with size of 40 x 40 mm² were used as substrates. The thickness of ceria layers was adjusted in the range of 1-3 μ m by controlling the coating times and solid concentration of the nano-suspension. As the layer thickness increases, the curvature and deflection of the samples increases accordingly and the acquired results are listed in Table 4.8. The measured overall deflection of the sintered sample with 1 μ m thick ceria layer prepared on 1 mm thick pre-sintered anode substrate is only 0.11 mm. The deflection and curvature increased dramatically to 3.6 mm as the layer thickness increased to 3 μ m. The visualized deflection and curvature results are demonstrated in Figure 4.41.

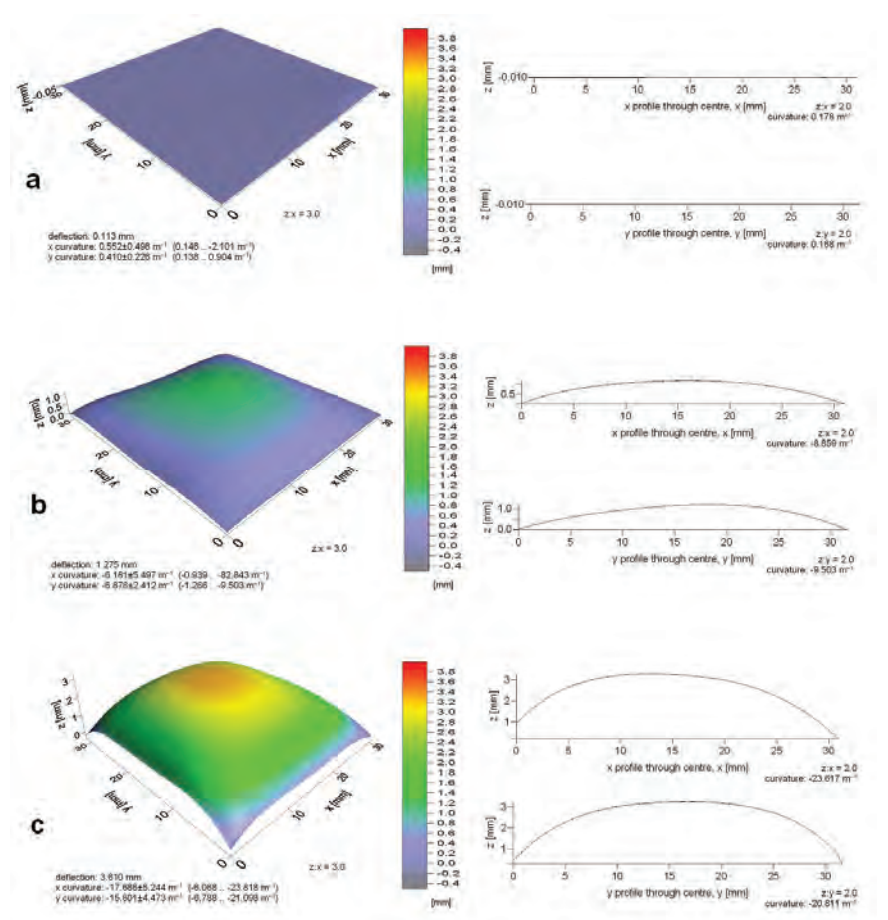


Figure 4.41 Topography of dip-coated ceria layers on rectangular warm-pressed anode supports (thickness=1 mm), sintered at 1400°C for 5 h: (a) 1 time dip-coated layer with thickness of \sim 1 μ m, (b) 2 times dip-coated layer with thickness of 1.5-2.5 μ m, (c) 3 times dip-coated with layer thickness of 3-3.5 μ m

	Layer thickness	Deflection	x-axis profile through center,	y-axis profile through center,
	(µm)	(mm)	curvature(m ⁻¹)	curvature (m ⁻¹)
a	1 μm	0.96	5.34	2.14
b	2 μm	0.17	0.72	0.53
С	3 μm	0.48	-1.89	-2.32

Table 4.9 Bending results of sintered ceria layers on air side of ~0.6mm thick tape-cast anode support

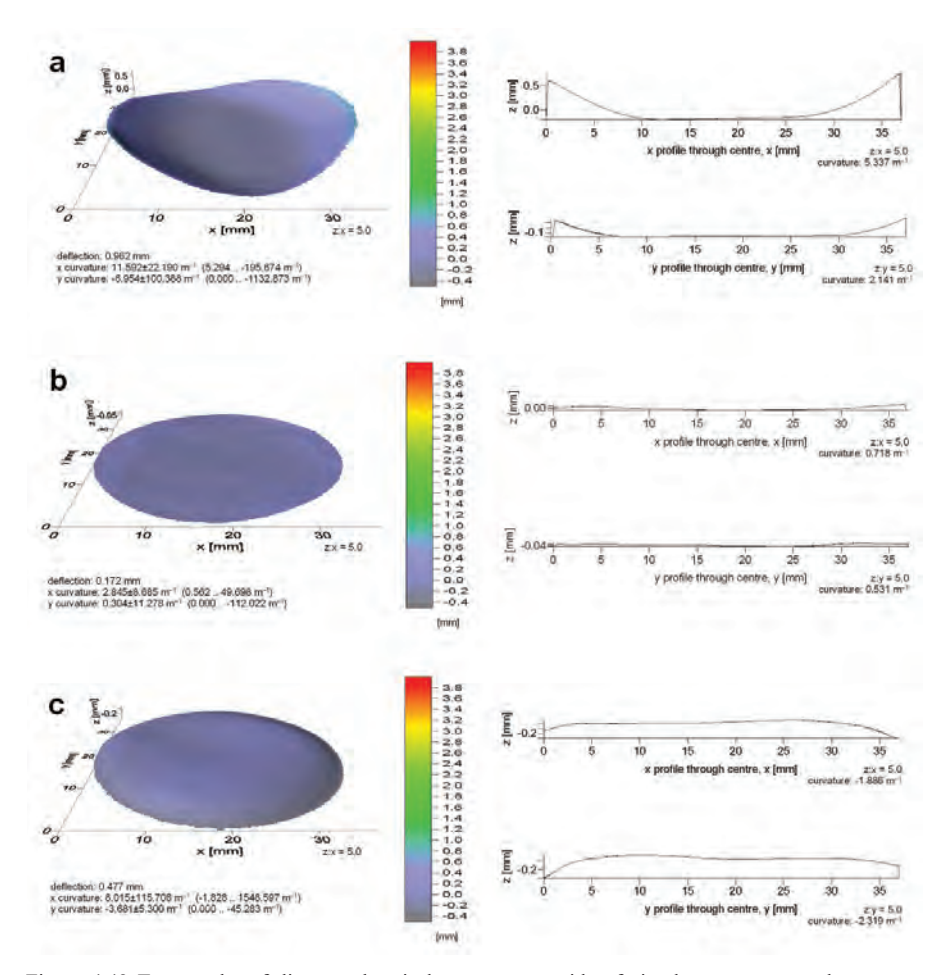


Figure 4.42 Topography of dip-coated ceria layers on tape side of circular tape-cast anode supports (thickness= \sim 0.6 mm, diameter=4 cm) sintered on air side at 1400 °C: (a) 1 time dip-coated layer with thickness of \sim 1 µm, (b) 2 times dip-coated layer with thickness of 1.5-2.5 µm, (c) 3 times dip-coated with layer thickness of 3-3.5µm

In a second experiment, circular tape-cast anode supports (0.6 mm thick, pre-sintered at 1230 °C for 3 h) were used as substrates. Ceria layers were directly deposited on the pre-sintered substrate by dip-coating. The layer thickness was also adjusted in the

range of 1-3 μ m by controlling the coating parameters and all samples were sintered at 1400 °C for 5 h. The deflection behaviour of the samples is strongly dependent on layer thickness. The direction of sample curvatures changed as the thickness of ceria layers increased from 1-3 μ m. As observed in Table 4.9 and Figure 4.42, the sample with 2 μ m ceria layer has the minimum curvature among the samples, because the shear stress on the layer/substrate interface is nearly balanced. Otherwise, unbalanced stress at the layer/substrate interface may cause curvature in the samples.

The bending of samples may attribute to the different shrinkage behaviours of the deposited layers and the substrates, as well as their different material composition and porosity. The thickness of the layers and substrates also plays an important role in the process. Through the optimization of the material composition, porosity and the thickness ratio between the coated layers and substrates, it might be possible to avoid bending and produce flat samples without flattening process by application of a weight load during the thermal treatment.

4.2.3.6 Layers deposited on pre-sintered anode substrate by spin-coating method

Homogeneous hybrid layers with PVA and ceramic particles are easily formed on warm-pressed substrate by spin-coating nano-suspensions` at a rotation speed of 1200 rpm. As shown in Figure 4.43, the thickness of the sintered electrolyte layer is about 1.5 μ m and the grain size is in the range of 1-3 μ m. Pin-hole located on the grain boundary with size of ~0.5 μ m is also observed in backscattered SEM surface image of the crack-free electrolyte layer.

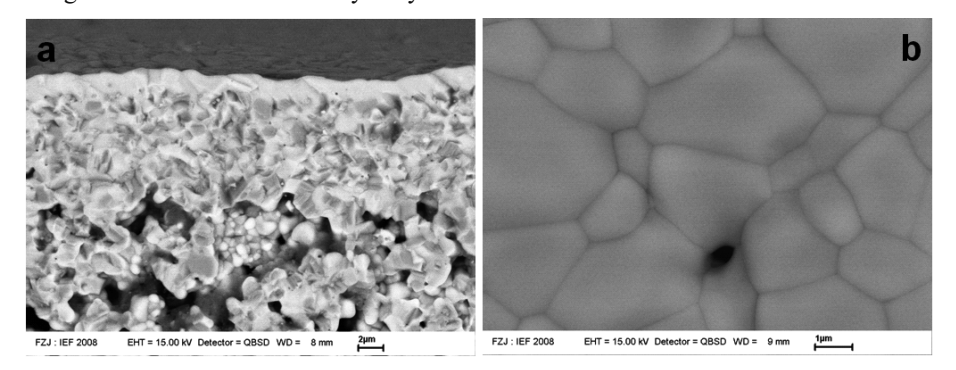


Figure 4.43 SEM images of spin-coated electrolyte on warm-pressed anode support with colloidal sol/suspension: (a) fracture surface, (b) surface

At the rotation speed of 1200 rpm, no layer is formed on tape-cast substrates because the surface of the FG31 and FG2 substrates with fine pore structure are much smoother than the warm-pressed substrates. Different from the dip-coating process, the properties of substrates, especially the surface roughness and pore structure, have remarkable influence on the layer formation behaviours of the PVA modified sols and nano-suspensions in fabrication of electrolyte layers via spin-coating method. The spin-coating parameters were optimized in order to prepare electrolyte layers on tape-cast substrates. By reducing the spin speed from 1200 to 400~800 rpm with acceleration of 20 rpm/s, homogenous 8YSZ electrolyte layers with adequate thickness were successfully deposited on tape-cast substrate and the photograph of the as-deposited layer (calcined at 500 °C for 1 h) is shown in Figure 4.44.

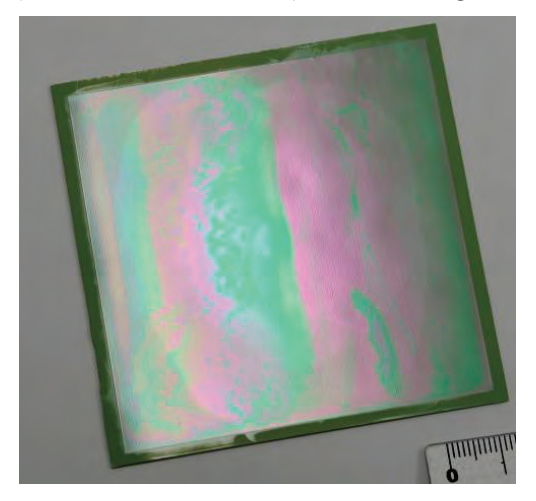


Figure 4.44 Half-cell with spin-coated 8YSZ layer (calcined at 500 °C for 1 h), pre-sintered FG02 anode support with screen-printed anode as substrate

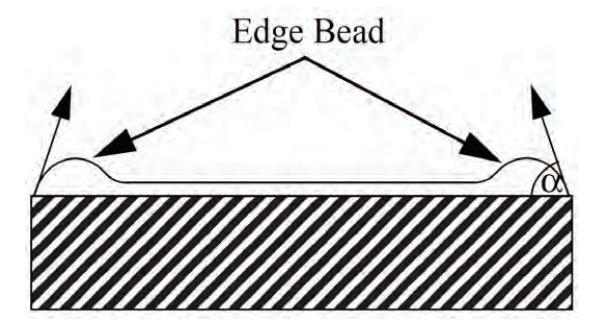


Figure 4.45 Graphical description of the edge bead effect [113], α is the wetting angle

According to work of G. Carcano et al. [113], edge beads are frequently formed in the spin-coating process with viscous liquids. The viscosity and surface tension dictate a constant contact angle at the solid-liquid-gas interface as seen in Figure 4.45. Cracks are normally formed in the dried edge bead due to the exceeding of critical thickness for crack-free layers. Not only the sol properties determine the edge bead, but spin coating recipe contributes as well. Due to the increased friction with air at the edge of the substrate, the sol in the bead dries fast, blocking the remaining sol to flow over the step and making the edge bead grows. Higher spin speed is favourable to reduce the size and width of the edge bead and avoid cracks in this region. Due to this reason, the standard spin coating speed was chosen to be 800 rpm, instead of 400 rpm, in most cases of the subsequent coatings on tape-cast substrates.

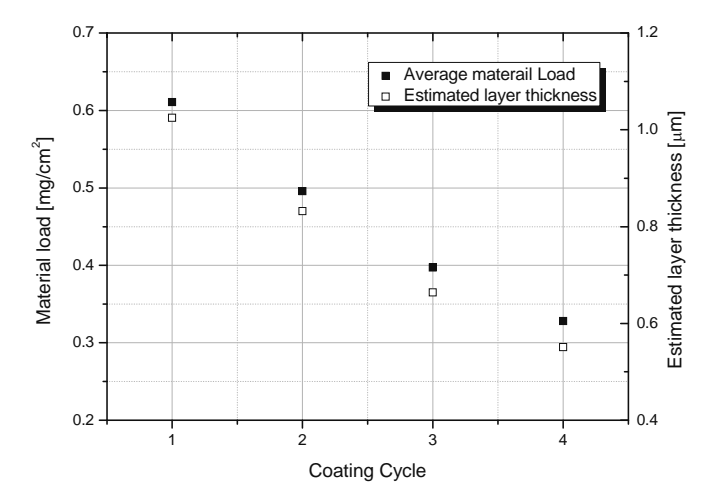


Figure 4.46 Weight gain of electrolyte layers by each coating cycle on FG02 substrates

It is observed in Figure 4.46 that the average weight of 4 subsequently spin-coated 8YSZ layers on tape-cast substrates decreased substantially. According to the coating sequence, the average weight of the layers is 0.61 mg/cm², 0.50 mg/cm², 0.40 mg/cm² and 0.33 mg/cm², respectively. The observed decrease in layer weight might be due to the fact that the fine particle infiltration into the substrates from the layer n+1 is impeded by the firstly coated layer n and the nano-suspension flows away from the sample more easily, while the pore structure on the sample surface became finer and the surface roughness reduced gradually as the spin-coating process repeated.

4.2.3.7 Layers deposited on sintered non-shrinking anode substrate by spincoating method

As there are great interests in coating dense layer on non-shrinking substrates, FG31 anode supports were firstly thermally treated at 1340 °C, 1370 °C and 1400 °C for 5 h. Subsequently, the microstructure and surface property of the substrate were changed and the well-distributed pores were closed on the anode surface as the thermal treatment temperature increased. As illustrated in Figure 4.47, the well-distributed pores in the substrates calcined at 1230 °C for 3 h offered well-distributed capillary force, which draws the liquid in the sol of nano-suspension into the pores of the substrate and improved the package density of the particles near the substrate surface due to the capillary pressure, forming a densely packed layer. During the spin-coating or dip-coating process, the packed layer stays firmly on the substrate and the superfluous sol and nano-suspension flows and takes away the particles in the "flow layer". In the case of sintered substrate, the most of the pores are closed in the substrate after the high-temperature thermal treatment and distributed capillary force was not available anymore to take action on the sol to form a well-packed layer. Eventually, the particles in the sol/suspension flow away from the substrate and no layer is formed.

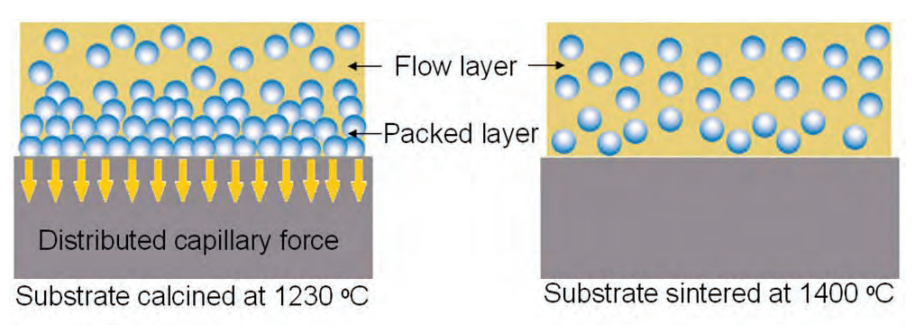


Figure 4.47 Influence of capillary force on the layer formation process

As shown in Figure 4.48, weight gain was hardly observed after the spin-coating was carried out on the substrates already sintered at 1370 °C or 1400 °C for 5 h. The average weight of thin layers formed on FG31 substrates calcined at 1340 °C for 5 h is

 $0.24~\rm mg/cm^2$, which is obviously less than the weight ($0.61~\rm mg/cm^2$) of layers formed on porous substrate only calcined at $1230~\rm ^oC$ for 3 h.

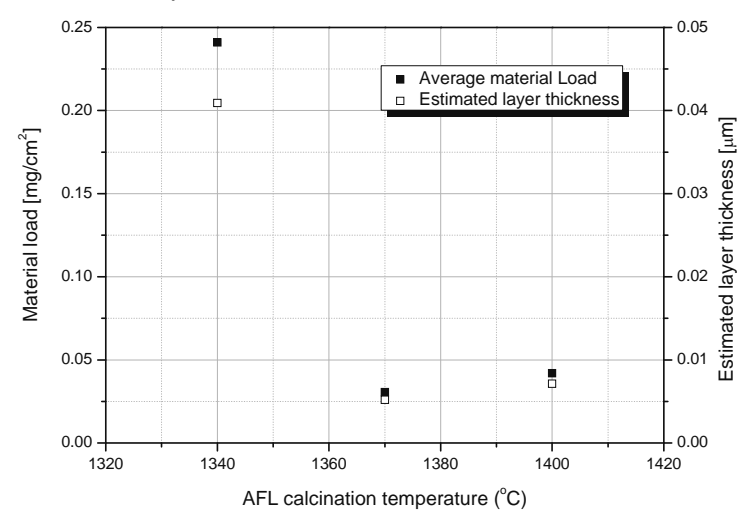


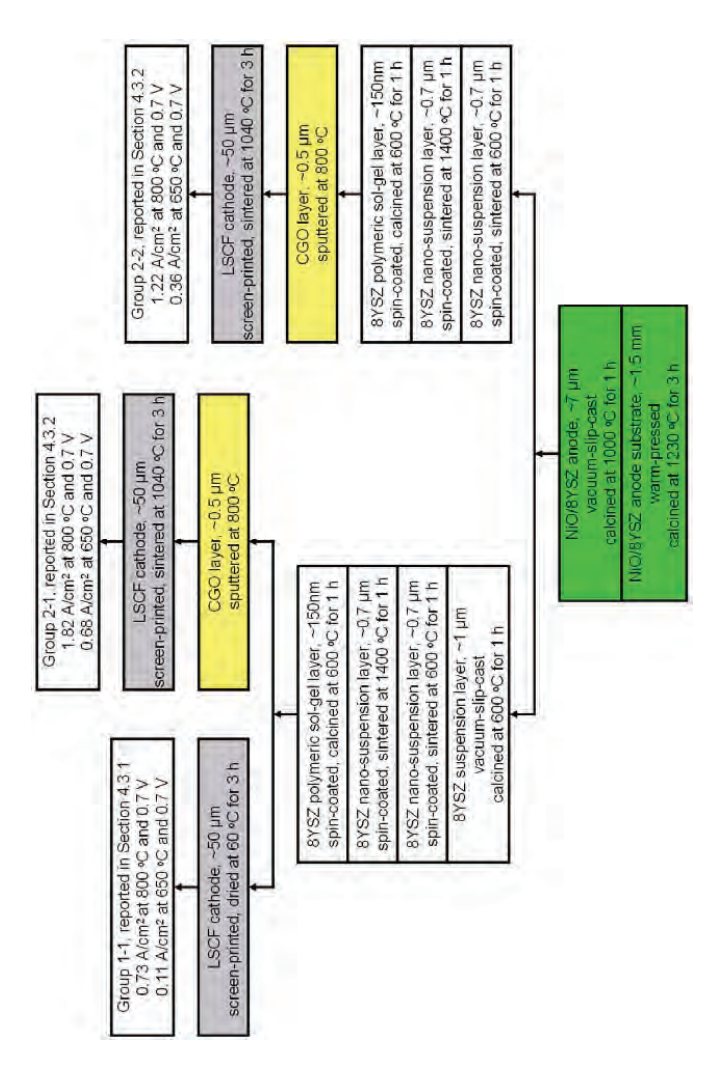
Figure 4.48 Weight of 8YSZ layer spin-coated on sintered FG31 substrates

4.2.3.8 Summary

Dense electrolyte layers have been successfully deposited on tape-cast anode support substrates via sol-gel dip-coating and spin-coating method. Using warm press substrates, layers can be easily formed by spin coating the PVA modified nanosuspension at a rotation speed of 1200 rpm. This might be due to the high roughness of the warm-pressed substrate as shown in Figure 4.22 in section 4.2.1, which provides a better layer formation property. In contrast, no layers with sufficient thickness were formed on the smooth tape-cast substrate at spin coating speed of 1200 rpm. In order to deposit thin layers on tape-cast substrate by spin coating of the nano-suspension, low rotation speed should be applied. The optimization of spin coating recipe was carried out and 800 rpm was chosen in the high-speed rotation step. The material load of 8YSZ layers formed on FG31 substrates were generally higher than the layers formed on FG02 substrates under same spin coating parameters due to the difference in the porosity of the substrates. Gas-tight layers were prepared by sintering the 8YSZ layer at 1400 °C for 5 h.

4.3 Electrochemical characterization of single cells

The electrochemical performance, including current density, area specific resistance (ASR), impedance spectroscopy, of the prepared single cells with varied processing parameters and layer configurations is reported in the following sections. The preparation flow charts are shown in Figure 4.49. The acquired characterization results are compared with the state-of-the-art anode-supported SOFCs, which are also mentioned as "reference cells". Reference cells are prepared and provided by Dr. S. Uhlenbruck and W. Herzhof from IEF-1. The electrochemical data of reference cells is measured and provided by Dr. V.A.C. Haanappel from IEF-3.



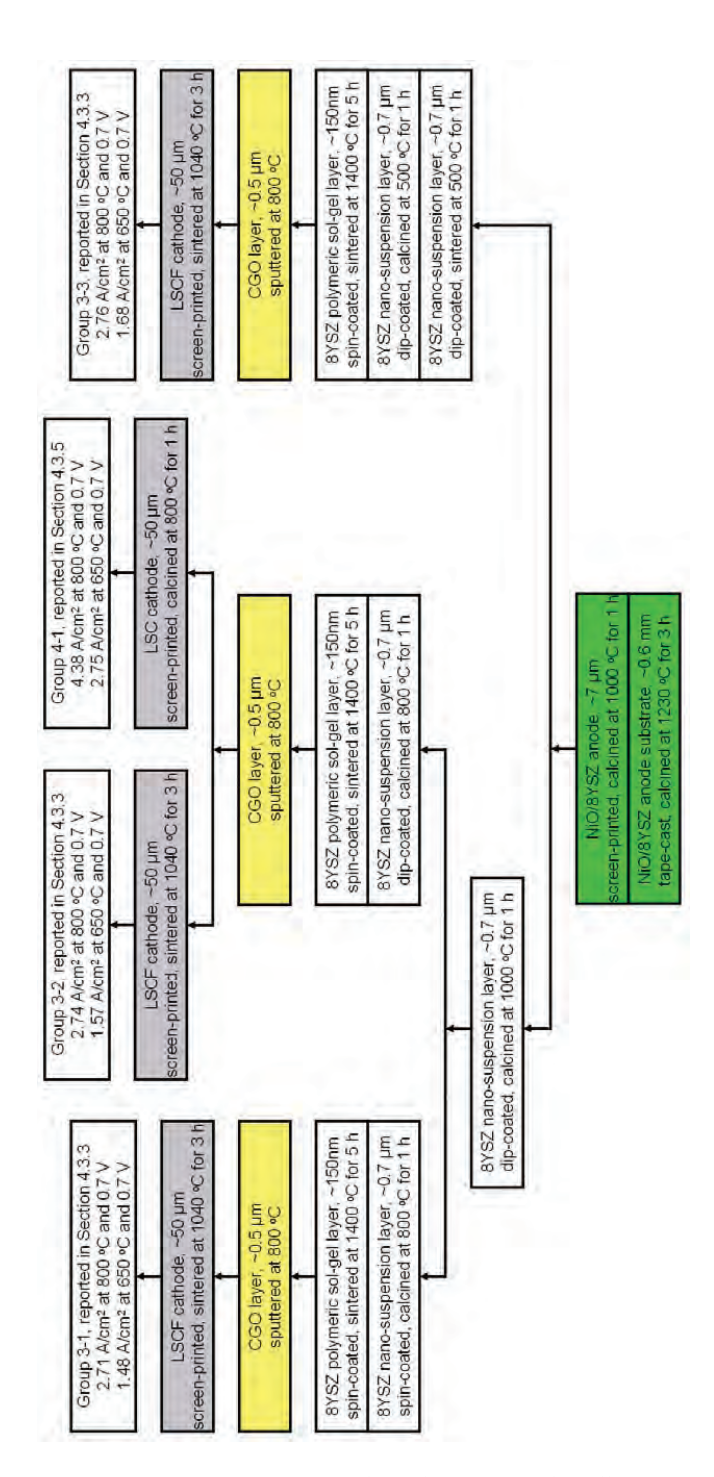


Figure 4.49 Preparation flow charts of single cells

4.3.1 Single cells with multi-layered electrolyte, without CGO layer and nonsintered LSCF cathode (Group 1-1)

In the fabrication process of single cells in Group 1-1, also seen in the flow chart of Figure 4.49, an aqueous 8YSZ suspension with average particle size ~120 nm was coated via vacuum slip casting method to form the first intermediate electrolyte layer on warm-pressed substrates. The second and third electrolyte layers were deposited with nano-suspension by spin coating. The primary particle size of the nanosuspension was less 10 nm, however, the average agglomerated particle size was approximately 40 nm. Then the first three layers were co-sintered at 1400 °C for 5 hours. Furthermore, the polymeric sol with average particle size less 10 nm was spincoated on the sintered electrolyte made from 8YSZ nano-suspension aiming to improve the gas-tightness of the electrolyte. In a calcination process at 600 °C for 1 h, the polymeric sol-gel precursor layer transformed into microporous ceramic layers. As shown in Figure 4.50, the total thickness of the homogeneous and dense multilayered 8YSZ electrolyte is approximately 2 μm thick. No Ce_{0.8}Gd_{0.2}O_{2-δ} (CGO) diffusion barrier layer was applied and a 50 μm thick La_{0.58}Sr_{0.40}Fe_{0.80}Co_{0.20}O_{3-δ} (LSCF) cathode layer was directly screen-printed on the as-deposited multi-layeredstructured electrolyte and dried at 60 °C. The samples were electrochemically tested without carrying out the sintering step for the cathode.

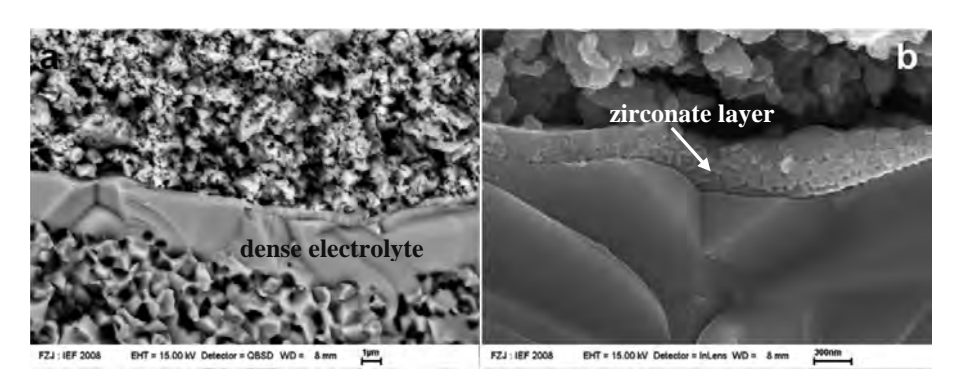


Figure 4.50 Fracture surface SEM images cell 11602-7 in Group 1-1 with multi-layered electrolyte and without CGO layer: (a) dense intermediate layer, (b) zirconate layer with poor cunductivity

The helium leak rate of the half-cells without deposition of polymeric sol-gel layers is in the range of 4.3×10^{-5} to 9.1×10^{-5} (hPa·dm³)/(s·cm²). After coating of the polymeric

sol-gel layer, the helium leak rate of the half-cells with multi-layered electrolyte is improved to the range of 1.2×10^{-5} to 2.9×10^{-5} (hPa·dm³)/(s·cm²). It is found in Figure **4.51** that the helium leak rate reduces steadily as the deposition of polymeric sol-gel layer was repeated. In other words, the gas-tightness improvement has a dependence on the thickness of the microporous top layer deposited with polymeric 8YSZ sol. In the process, the polymeric sol may infiltrate into the defects in the sintered electrolyte reducing the defect size and the leakage rate.

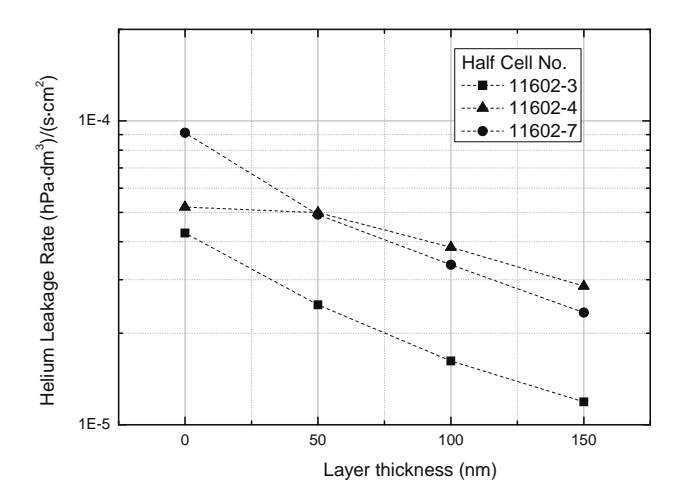


Figure 4.51 Dependance of improvement in helium leak rate on the thickness of deposited thin porous top layer by spin-coating the polymeric 8YSZ sol, the layers are calcined at 600 °C for 1 hour.

As shown in Figure 4.52, the measured open circuit voltage (OCV) of test cells in Group 1-1 is approximately 1.09V, which is in good agreement with the OCV of the reference cell, indicating that the as-prepared multi-layered electrolyte is dense and gas-tight. The current density of the cells is calculated by dividing the measured current by the cathode area of 16 cm². At a cell voltage of 0.7 V, the measured current densities of the tested cells in Group 1-1, which are without CGO layer and with non-sintered LSCF cathode, are 0.73 A/cm² at 800 °C and 0.11 A/cm² at 650 °C, which are significantly lower than the values of the reference cells with magnetron sputtered CGO layer and sintered LSCF cathode (1040 °C for 3 h), accordingly 2.09 A/cm² at 800 °C and 1.02 A/cm² at 650 °C. The average area specific resistance (ASR) of the

tested cells is 2 times higher at 800 °C and 14 times higher at 650 °C than the ASR of reference cells, as listed in Table 4.10.

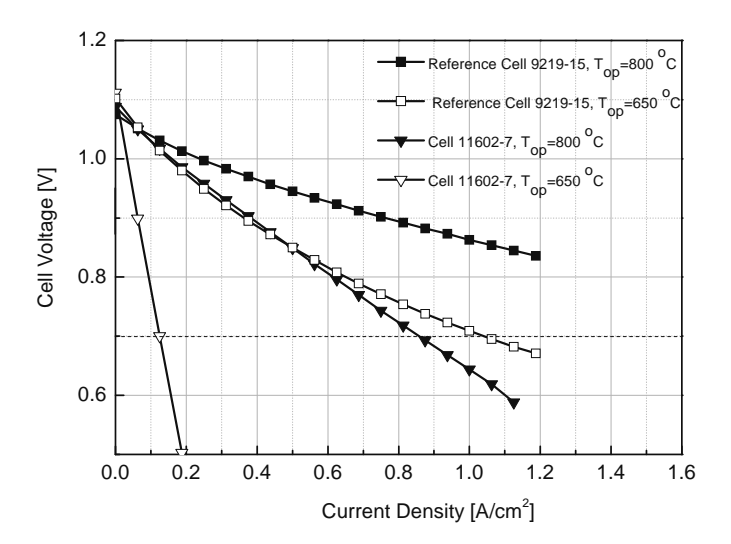


Figure 4.52 *i*-V curves of cell 11602-7 in Group 1-1 compared with reference cell 9219-15, operated at 650 and 800 °C, different from the tested cells, the reference cells are with vacuum-slip-cast electrolyte $(7\sim10~\mu\text{m})$, sputtered CGO layer $(1~\mu\text{m})$ for 3 h.

Temperature	ASR_{Tested}	ASR _{Reference}	ASR Difference
(°C)	$(m\Omega \cdot cm^2)$	$(m\Omega \cdot cm^2)$	$(m\Omega \cdot cm^2)/\%$
800	509	157	352 / +224%
750	908	160	748 / +468%
700	1944	199	1745 / +902%
650	3637	245	3392 / +1400%

Table 4.10 Average ASR of tested cells of Group 1-1 (cell 11602-3 and cell 11602-7 without CGO layer and with non-sintered LSCF cathode) compared with reference cells (cell 9219-11 and cell 9219-15, with magnetron sputtered CGO layer and sintered LSCF cathode)

The most important reason for the extremely poor electrochemical performance of the tested cells in Group 1-1 is the formation of insulating layers on the top of the electrolyte during the testing process at high temperature of 800 to 900 °C. Without the deposition of the CGO barrier layer, strontium diffused from the cathode reacted with the 8YSZ electrolyte and formed zirconate layer (Figure 4.50b), such as SrZrO₃ or La₂Zr₂O₇ [61]. The strontium mainly reacted with the 8YSZ top layer in the electrolyte due to the high reactivity of the nano-scaled particles and grains in the

porous 8YSZ top layers. As observed, the zirconate layer is 200 to 500 nm thick, which is comparable with the thickness of 8YSZ top layer made of polymeric 8YSZ sol. The second explanation for the poor performance of the cells is the delamination of the non-sintered cathode from the electrolyte surface (as shown in Figure 4.53). The total measured current during the test at varied temperature is remarkably low because the effective cathode/electrolyte contact interface area significantly reduced due to the delamination.

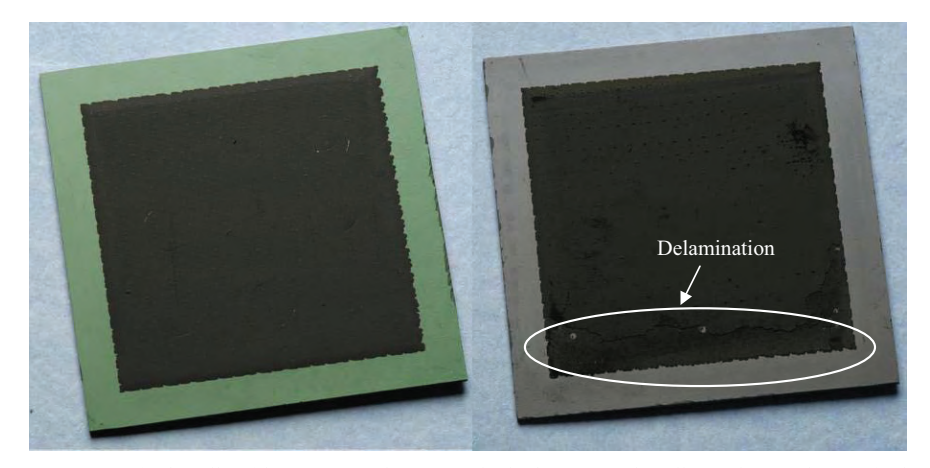


Figure 4.53 Single cells with non-sintered LSCF cathode: before single cell test (left) and after single cell test (right)

4.3.2 Single cells with multi-layered electrolyte, CGO layer and sintered LSCF cathode (Group 2-1 and Group 2-2)

In order to obtain satisfactory electrochemical cell performance, it is essential to deposit CGO barrier layer to avoid formation of zirconate layers and the LSCF cathode should be sintered in advance in a proper thermal treatment process to prevent the cathode delamination from the cells. Thus, the half-cells with multi-layered electrolytes were prepared in the same way as described in Section 4.3.1. Additionally, CGO barrier layers (~0.5 µm in thickness) were coated by magnetron sputtering at 800 °C. The LSCF cathode was screen-printed, dried at 60 °C and then sintered at 1040 °C for 3 hours. As shown in Figure 4.54, the sintered cathode shows good adhesion to the half-cells before and after the electrochemical test and the delamination of cathode is not observed. The helium leak rate of tested half-cells is in

the range of 1.6×10^{-5} to 3.7×10^{-5} (hPa·dm³)/(s·cm²), which is as good as the cells in Group 1-1 reported in Section 4.3.1.

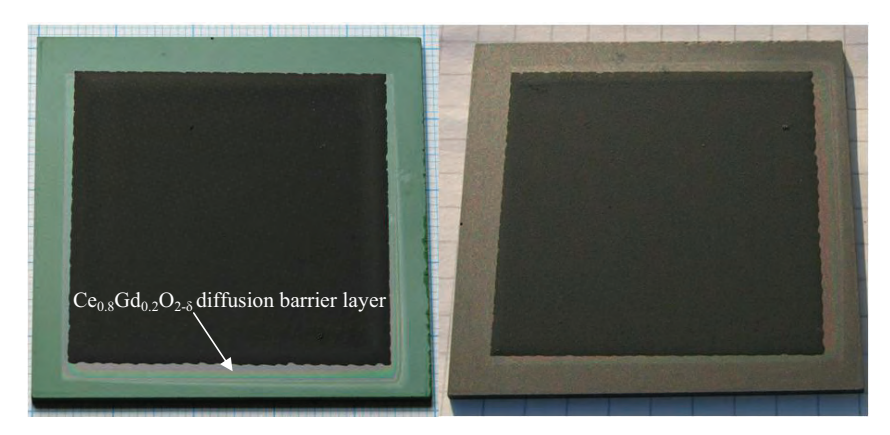


Figure 4.54 Single cells with magnetron sputtered CGO diffusion barrier layer and sintered LSCF cathode: before single cell test (left) and after single cell test (right)

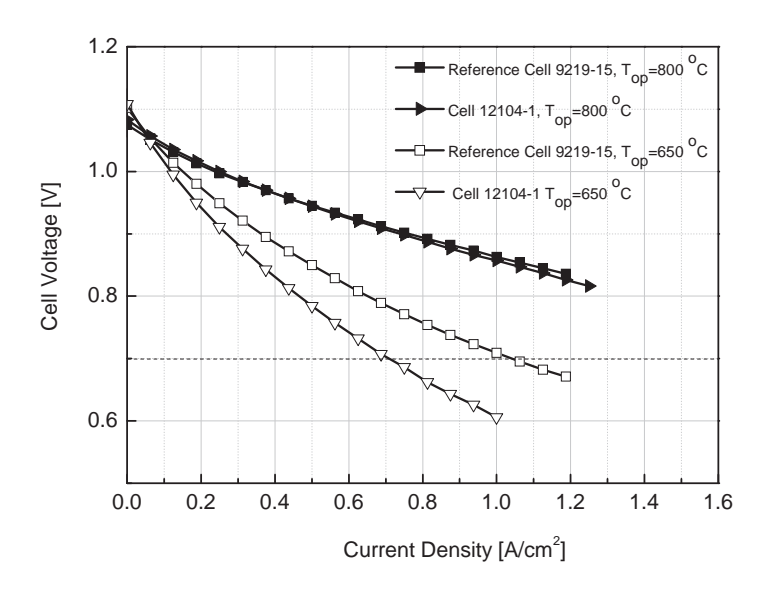


Figure 4.55 *i*-V curves of cell 12104-1 in Group 2-1 compared with reference cell 9219-15, operated at 650 and 800 °C, different from the tested cells, the reference cells are with vacuum-slip-cast electrolyte $(7\sim10~\mu\text{m})$, sputtered CGO layer $(1~\mu\text{m})$ for 3 h

As shown in Figure 4.55, the measured open circuit voltages (OCV) are 1.08 and 1.11 V at 800 and 650 °C, respectively. At operating temperature of 800 °C, the *i*-V curves showed no significant difference between the tested cells in Group 2-1 and the reference cell. The average current density (extrapolated) of three tested cells is

1.82 A/cm², generating the average power density of 1.27 W/cm² at a cell voltage of 0.7 V. At operating temperature of 650 °C, the average current density (measured) of the tested cells is 0.68 A/cm², 31% lower than then average current density of reference cells (0.99 A/cm²). The average area specific resistance (ASR) of test cells is 11% higher than the ASR of the reference cells at operating temperature above 700 °C and 56% higher than reference cells at 650 °C, as listed in Table 4.11. The thickness of the 8YSZ electrolyte is more influential on the ASR at low operating temperature than at high operating temperature.

Temperature	ASR_{Tested}	$ASR_{Reference}$	ASR Difference
(°C)	$(m\Omega \cdot cm^2)$	$(m\Omega \cdot cm^2)$	$(m\Omega \cdot cm^2) / \%$
800	173	157	16 / +11%
750	181	160	21 / +11%
700	223	199	24 / +11%
650	382	245	137 / +56%

Table 4.11 Average ASR of tested cells in Group 2-1 (cell 12104-1, cell 12104-2, and cell 12104-3, with magnetron sputtered CGO layer and sintered LSCF cathode) compared with reference cells (cell 9219-11 and cell 9219-15, with magnetron sputtered CGO layer and sintered LSCF cathode)

According to the observed i-V behaviors in Figure 4.55, it is concluded that the electrochemical performance of as-prepared single cells in Group 2-1 with a 2 μ m thick electrolyte are only as good as the state-of-the-art reference cells with 8 μ m thick electrolyte at operating temperature of 800 °C and performed worse than reference cells at operating temperature of 650 °C, with power output decrease of about 30%.

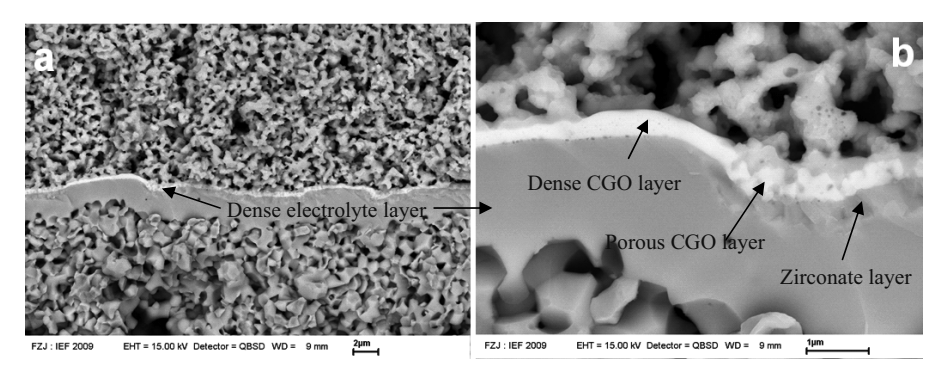


Figure 4.56 Fracture surface SEM of cell 12104-1 in Group 2-1 with multi-layered electrolyte, CGO layer and sintered LSCF cathode: (a) dense intermediate layer, (b) CGO layer and zirconate layer

The SEM fracture surface image of cell 12104-1 in Figure 4.56 confirmed that the as-

deposited electrolyte is dense and with average thickness about 2 μ m. Second phase of zirconate compound is found at some part of the 8YSZ/CGO interface. Apart from the cracks and pin-holes observed in the SEM surface images (Figure 4.57a, b), the polymeric-sol-derived electrolyte layer calcined at 1040 °C, the typical calcination temperature of the LSCF cathode in the cell manufacturing process, is found to be porous and with grain size of ~150 nm. As discussed in section 4.2.2, the additionally coated microporous layer made from polymeric 8YSZ sol is overly sintered and becomes macroporous in thermal treatment at 1040 °C. Large pores in the range of 50 to 150 nm in diameter scattered all over the surface of the top electrolyte layer, as observed in Figure 4.57b.

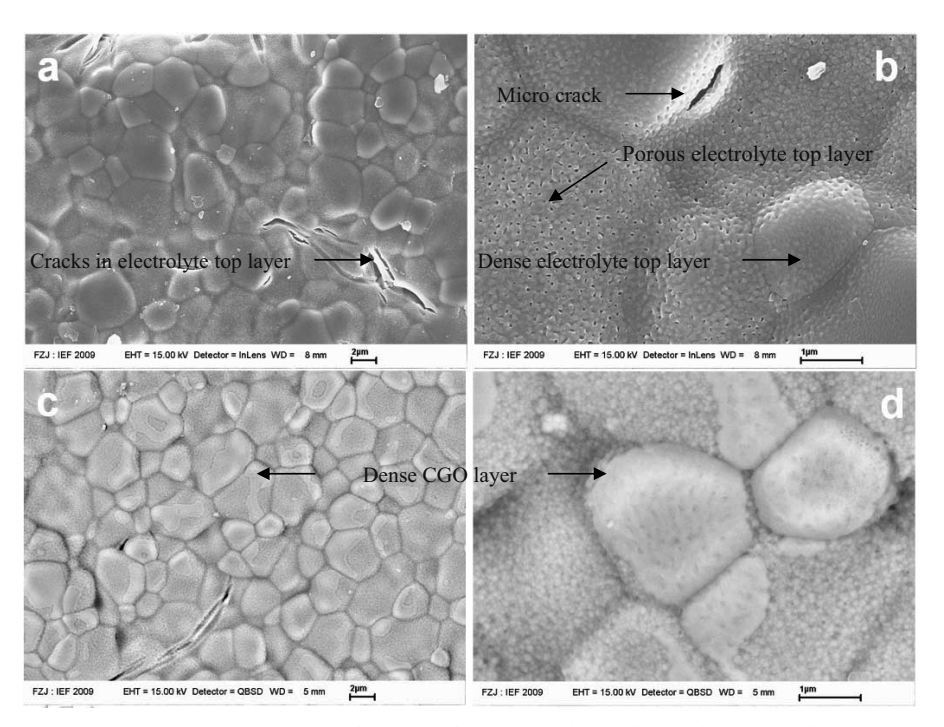


Figure 4.57 SEM surface images of the 8YSZ electrolyte and CGO barrier layers of cell 12104-1 in Group 2-1: (a), (b) surface of 8YSZ electrolyte; (c), (d) surface of CGO barrier layer

The CGO layer sputtered before the deposition of cathode also inherited the microstructure, such as grain size and porosity, of the top 8YSZ layer heated at 800 °C and might be further influenced by the microstructure change of the electrolyte surface as the single cells were exposed to a thermal treatment during the sintering of cathode layer at 1040 °C. The CGO layer sputtering process is demonstrated in the

schematic diagram in Figure 4.58. Dense CGO layers formed at the locations where the underlying mesoporous 8YSZ layer (thermally treated at 800 °C, typical substrate temperature for sputtering of CGO layers) is also dense or where the thickness of sputtered CGO layer is sufficient to fill the depth of the pores or to bridge the width of the pores. Grain boundary is not visible in the dense part of the barrier layer, however, the rest part of the CGO layer is not fully dense and mainly covered with small grains in size of about 150 nm (Figure 4.56b and Figure 4.57c, d).

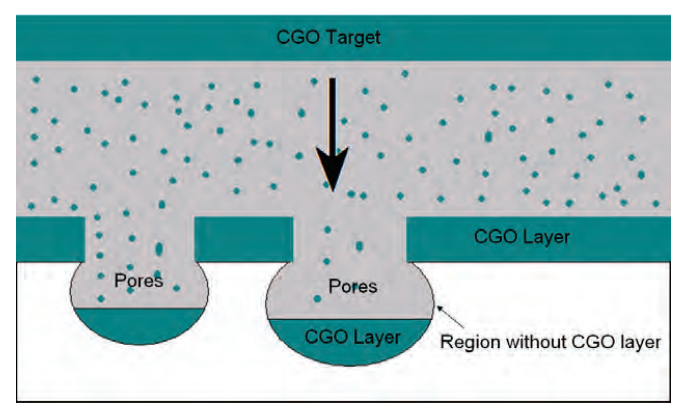


Figure 4.58 Diagram of CGO layer sputtering process

According to the microstructure morphology of the as-prepared single cells, the main reason for the ordinary cell performance still seems to be attributed to the formation of zirconate layers in the electrolyte during sintering the LSCF cathode at 1040 °C. In the process, strontium (Sr) diffused from the La_{0.58}Sr_{0.4}Fe_{0.2}Co_{0.8}O_{3-δ} cathode through the pores and cracks in the CGO layer to the 8YSZ/CGO interface, forming ionic insulating zirconate compounds such as SrZrO₃, which is observed in the material contrast SEM image in Figure 4.59 obtained by the back scattering detector. The accumulation of Sr in the secondary phase at 8YSZ/CGO interface is confirmed by EDX analysis. The formation of the insulating layers (normally 200~500 nm in thickness) could result in remarkable negative effects on the overall performance of the tested cells, which counteract the positive contributions brought by the electrolyte thickness reduction. No Sr is detected at point 3 in Figure 4.59 because dense CGO barrier layer at this region effectively prevented the Sr diffusion. As a result, the actual overall ionic conductivity of the as-prepared thin electrolyte was not improved due to the formation of insulating layers under the porous part of the CGO layer. The

electrical performance is still comparable with the performance of the reference cells at $800\,^{\circ}$ C. However, the cell performance became much worse as the conductivity of the as-prepared electrolyte dropped dramatically at cell operating temperature of $650\,^{\circ}$ C.

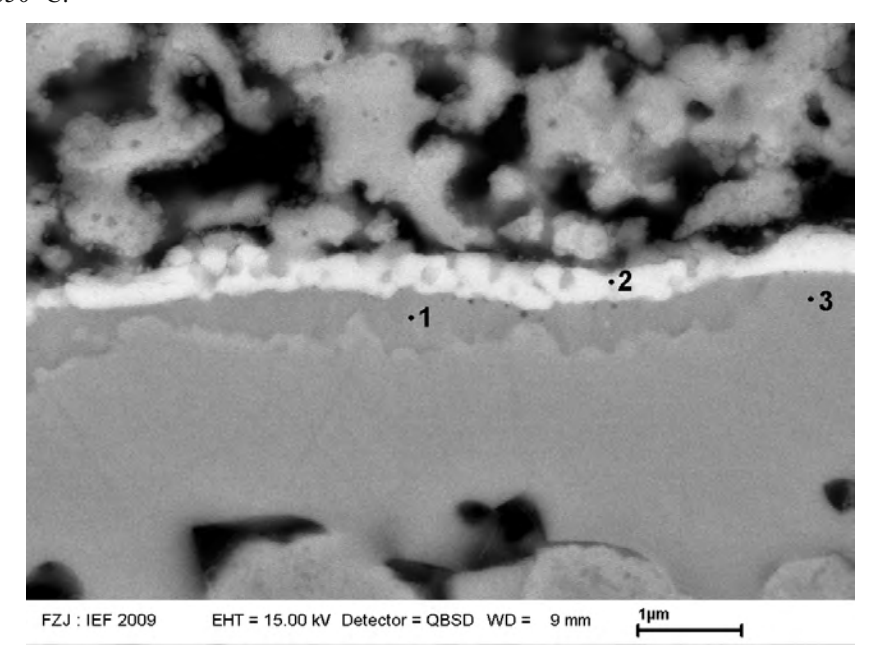


Figure 4.59 Polished cross section of tested single cell no. 12104-1 with multi-layered electrolyte, CGO layer and sintered LSCF cathode.

In the preparation of single cells of Group 2-2, deposition of aqueous 8YSZ suspension layers was not applied any more in order to simplify the electrolyte fabrication process and to reduce the electrolyte thickness to about 1 μ m. As demonstrated in Figure 4.49, the electrolyte is deposited by spin-coating of 8YSZ nano-suspension on the porous substrate with anode layer. Sintered at 1400 °C for 5 h, the electrolyte was additionally coated with polymeric-sol and calcined at 600 °C. CGO barrier layers (~0.5 μ m in thickness) were deposited by magnetron sputtering at 800 °C. The LSCF cathode was screen-printed, dried at 60 °C and then sintered at 1040 °C for 3 hours. The average helium leak rate of the half-cells prepared in this group of samples is 2.5×10^{-5} (hPa·dm³)/(s·cm²), proving that the gas-tightness of the 1 μ m thick multi-layered electrolyte is comparable to the 2 μ m thick electrolyte in Group 1-1, Group 2-1 and the 8 μ m thick electrolyte prepared by vacuum-slip-casting or screen-printing methods. The results confirm that the gas-tightness of the 1 μ m

thick electrolyte is technically acceptable without the deposition of the vacuum-slipcast suspension layers.

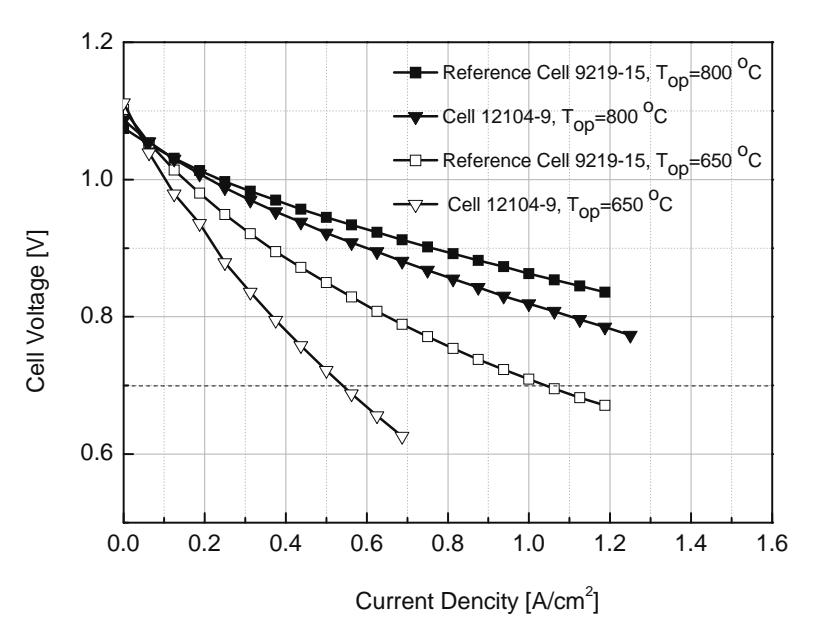


Figure 4.60 i-V curves of cell 12104-9 in Group 2-2 compared with reference cell 9219-15, operated at 650 and 800 $^{\circ}$ C

Temperature	ASR_{Tested}	ASR _{Reference}	ASR Difference	
(°C)	$(m\Omega \cdot cm^2)$	$(m\Omega \cdot cm^2)$	$(m\Omega \cdot cm^2) / \%$	
800	250	157	93 / +60%	
750	348	160	188 / +117%	
700	564	199	366 / +184%	
650	987	245	742 / +304%	

Table 4.12 Average ASR of tested cells in Group 2-2 compared with reference cells

As shown in Figure 4.60, the measured open circuit voltages (OCV) are 1.09 and 1.11 V at 800 and 650 °C, respectively. The *i*-V curves of the tested cells showed significant performance drop in comparison with the reference cells. At operating temperature of 800 °C, the average current density (extrapolated) of tested cells is 1.22 A/cm², generating the average power density of 0.85 W/cm² at a cell voltage of 0.7 V, 40% lower than then average current density of reference cells (2.04 A/cm²). At operating temperature of 650 °C, the average current density (measured) of the tested cells is 0.36 A/cm², 64% lower than the reference cells (0.99 A/cm²). The average area specific resistance (ASR) of the test cells is approximately 60% higher in

comparison with the ASR of the reference cells at operating temperature of 800 °C and dramatically increased to 3 times higher than the ASR of the reference cells at 650 °C, as listed in Table 4.12.

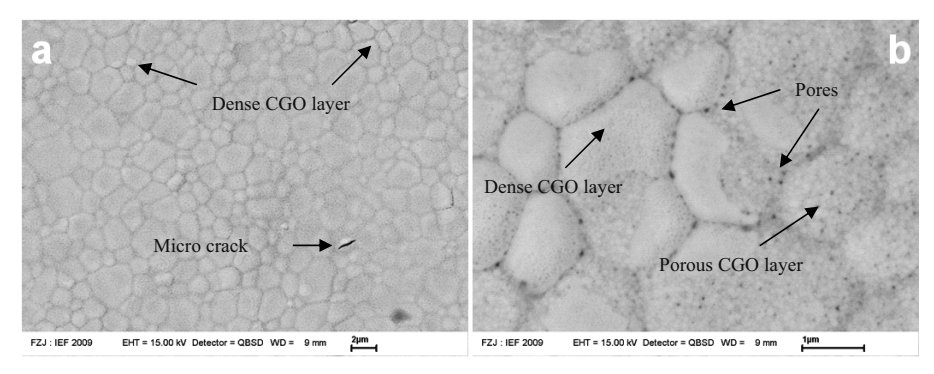


Figure 4.61 SEM surface image of magnetron sputtered CGO barrier layer on multi-layered electrolyte (cell no. 12104-9)

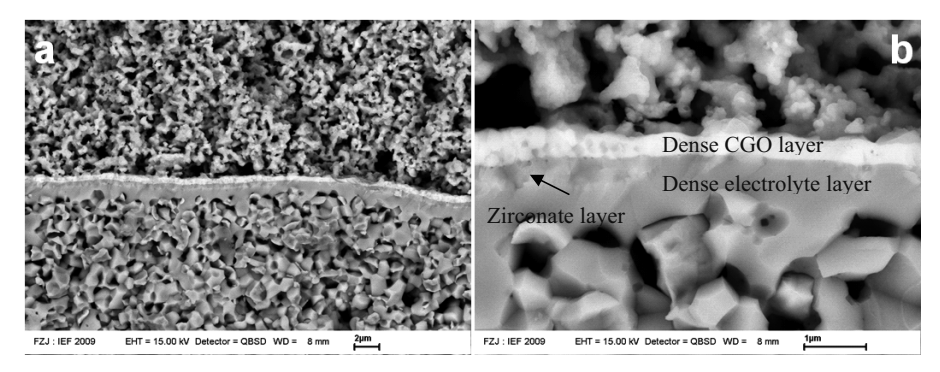


Figure 4.62 SEM fracture surface of cell 12104-9 with a multi-layered structured electrolyte and magnetron sputtered CGO barrier layer: (a) dense electrolyte, (b) zirconate layer and dense CGO layer

The electrochemical performance of the tested single cells in Group 2-2 with multilayered electrolyte is significantly lower than the reference cells. The reasons for the poor performance are also due to the formation of insulating layers, as discussed in section 4.3.2. The microstructure images demonstrated in Figure 4.61 and Figure 4.62 confirmed again that the calcined top electrolyte layers are overly sintered at higher thermal treatment temperature and the pores in the surface of the electrolyte resulted in a porous sputtered CGO layer. Strontium (Sr) diffusion from La_{0.58}Sr_{0.4}Fe_{0.2}Co_{0.8}O_{3-δ} cathode through the pores or defects in CGO layer to the surface of electrolyte is also confirmed by EDX analysis. The strontium is scarcely detectable at point 1 and 4 of Figure 4.63, where the analyzed region is near the interface of dense 8YSZ and CGO layers, indicating that no zirconate compound is formed at this region due to the effective protection of the dense CGO layer from strontium diffusion. The reason for the scattered poor electrochemical single cell performance results is that only a portion of the deposited CGO layer is dense, as observed in SEM surface images (Figure 4.61). In fact, the actual overall conductivity of the electrolyte is strongly dependant on the area of the dense CGO barrier layer in between the 8YSZ electrolyte and the LSCF cathode. In another word, the area of the dense CGO layer determines the area of the electrolyte free of zirconate layer and the overall ionic conductivity of the whole electrolyte. As the ratio between the dense CGO layer and the porous CGO layer varied, the overall ionic conductivity of the whole electrolyte layer and the electrochemical performance of the single cells were influenced to different extents. The negative effects on the single cell performance caused by the formation of the zirconate layers suppressed the positive contributions brought by the electrolyte thickness reduction. As a result, the performance of the as-prepared single cells with 1 µm electrolyte are definitely worse than the reference cells with 8 µm thick electrolyte.

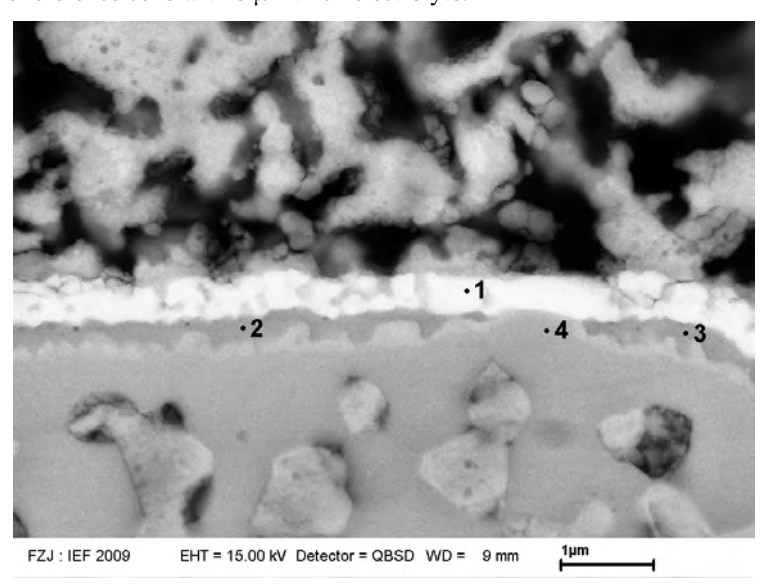


Figure 4.63 Polished cross section of single cell 12104-9 in Group 2-2 with multi-layered electrolyte, CGO layer and sintered LSCF cathode

4.3.3 Single cells with co-sintered multi-layered electrolyte, CGO layer and LSCF cathode (Group 3-1, Group 3-2 and Group 3-3)

In this section, three groups of single cells with co-sintered thin electrolytes are electrochemically tested. The preparation precedures of thin electrolyte layers are slightly different from each other. In the first group of single cells, Group 3-1, the first and second electrolyte layers were dip-coated and spin-coated with 8YSZ nanosuspension and calcined at 1000 °C and 800 °C, respectively, as illustrated in Figure 4.49. Polymeric sol was further spin coated and partly infiltrated into the first two 8YSZ layers made from nano-suspensions. The polymeric precursor layers transformed into microporous ceramic layers by a calcination process at 500 °C for 1 h. Aiming to avoid over-sintering of the electrolyte layers made from polymeric sol, all the 8YSZ layers were co-sintered together at 1400 °C for 5 h. The CGO barrier layer (~0.5 μm in thickness) was coated by magnetron sputtering at 800 °C. The LSCF cathode was screen-printed and dried at 60 °C, and finally sintered at 1040 °C, as described in section 4.3.2. The average helium leak rate of half-cells in the oxidized state in Group 3-1 was 1.2x10⁻⁵ (hPa·dm³)/(s·cm²)

Temperature	OCV _{tested cells}	OCV _{reference cells}	OCV _{Nernst equation}
(°C)	(V)	(V)	(V)
800	1.083	1.076	1.106
750	1.092	1.085	1.113
700	1.099	1.095	1.120
650	1.105	1.103	1.127

Table 4.13 Average open circuit voltage (OCV) of tested cells (cell 12625 and cell 12626) with cosintered multi-layered electrolyte in compare with reference cells (cell 9219-11 and cell 9219-15), and the theoretical value derived from Nernst equation

As summarized in Table 4.13, the open circuit voltage (OCV) of the tested cells with co-sintered multi-layered electrolyte in Group 3-1 are measured as 1.083, 1.092, 1.099 and 1.105 V at 800, 750, 700, and 650 °C, respectively. In comparison with the theoretical OCV values derived from the Nernst equation, the OCV loss of the reference cells with 7-10 μ m thick electrolytes increased from 24 to 30 mV as the operating temperature increased form 650 to 800 °C. In the case of the 1 μ m thick electrolyte prepared from the nano-suspension and polymeric sol, the OCV loss of the

tested cells remains 21 to 23 mV (\sim 2%) and is independent of the operating temperature. This phenomenon may indicate that the as-prepared electrolytes have fewer pin-holes and cracks, which normally influence the OCV loss at high temperature greatly due to more active gas diffusion behaviors.

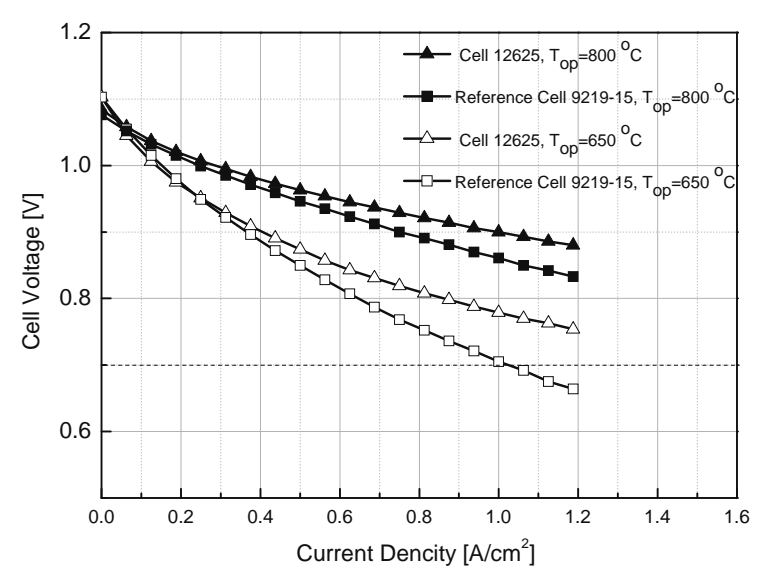


Figure 4.64 *i*-V curves of cell 12625 in Group 3-1 compared with reference cell 9219-15, operated at 650 and 800 °C, different from the tested cells, the reference cells are with vacuum-slip-cast electrolyte $(7\sim10~\mu\text{m})$, sputtered CGO layer $(1~\mu\text{m})$ for 3 h

As seen in Figure 4.64, the *i*-V curves of the tested single cells show excellent electrochemical performance and significant performance improvement is observed in comparison with the reference cells. The average extrapolated current density is 2.71 A/cm², generating the average power density of 1.90 W/cm² at a cell voltage of 0.7 V and operating temperature of 800 °C, which is more than 30% higher than the average current density of the reference cells (2.04 A/cm² and 1.42 W/cm²) operated under the same condition. At operating temperature of 650 °C, the average current density of the tested cells is 1.48 A/cm² and 50% higher than the values of the reference cells (0.99 A/cm²). The reduction in electrolyte thickness effectively improved the cell performances, especially at intermediate temperatures.

The average area specific resistances (ASR) of the test cells in Group 3-1 reduced to 115 and 158 m Ω ·cm² at operating temperature of 800 and 650 °C, approximately 27%

and 36% lower than the ASR of the reference cells, as listed in Table 4.14. The effects of electrolyte thickness reduction are more influential in minimizing the overall ASR of single cells at intermediate temperature than at the conventional SOFC operating temperature of 800 °C. The theoretically calculated ASR of 8 and 1 μ m thick 8YSZ electrolyte is also listed in Table 4.14. The contribution ratio of the electrolyte thickness reduction to the total single cell ASR reduction (Δ ASR_{cell})are calculated as 40%, 91%, 84% and 96% at 800, 750, 700 and 650 °C, respectively.

Temperature	ASR _{tested cell}	ASR _{reference cell}	ΔASR_{cell}	$ASR_{1\mu mEL}$	$ASR_{8\mu mEL}$	ΔASR_{EL}
(°C)	$(m\Omega \cdot cm^2)$	$(m\Omega \cdot cm^2)$	$(m\Omega \cdot cm^2)/\%$	$(m\Omega \cdot cm^2)$	$(m\Omega \cdot cm^2)$	$(m\Omega \cdot cm^2)$
800	115	157	-42 / -27%	2.4	19.2	-16.8
750	130	160	-30 / -19%	3.9	31.2	-27.3
700	144	199	-55 / -28%	6.6	53.0	-46.4
650	158	245	-87 / -36%	11.9	95.5	-83.6

Table 4.14 Average ASR of tested cells in Group 3-1 compared with reference cells

First of all, the achievement in the excellent cell performance resulted from the microstructure improvement of the 8YSZ electrolyte and CGO barrier layers. The formation of porous 8YSZ top layers was avoided by co-sintering all the layers in the multi-layered 8YSZ electrolyte. Pores can hardly be observed in the SEM surface image of sputtered CGO barrier layer on the co-sintered multi-layered electrolyte and the electrolyte showed a defect-free morphology in the SEM surface images (Figure 4.65). Instead of forming a porous top layer by thermally treated at 1040 °C for 3 h, the 8YSZ top layer made from polymeric sol was absorbed into the 8YSZ layer made from nano-suspension during the grain growth at co-sintering temperature of 1400 °C, as seen in Figure 4.65b. The electrolyte consists of large 8YSZ grains with size of ~4 μm and submicron-sized grains. Considering the electrolyte layer is only 1 to 2 μm thick, the large grain should be flat-shaped and the electrolyte surface is rugged and undulated. The difference in height at 8YSZ grain boundaries could be larger than 0.5 µm, which is comparable to the thickness of the sputtered CGO barrier layer. Therefore, pores and pin-holes are more easily formed near grain boundaries, as shown in Figure 4.65c and d. Although small amount of ionic insulating compounds, such as Sr-zirconate, may form in the electrolyte at some spots where the pores are located, these spots with ionic insulating compound are not a dominating factor to influence the overall single cell performance.

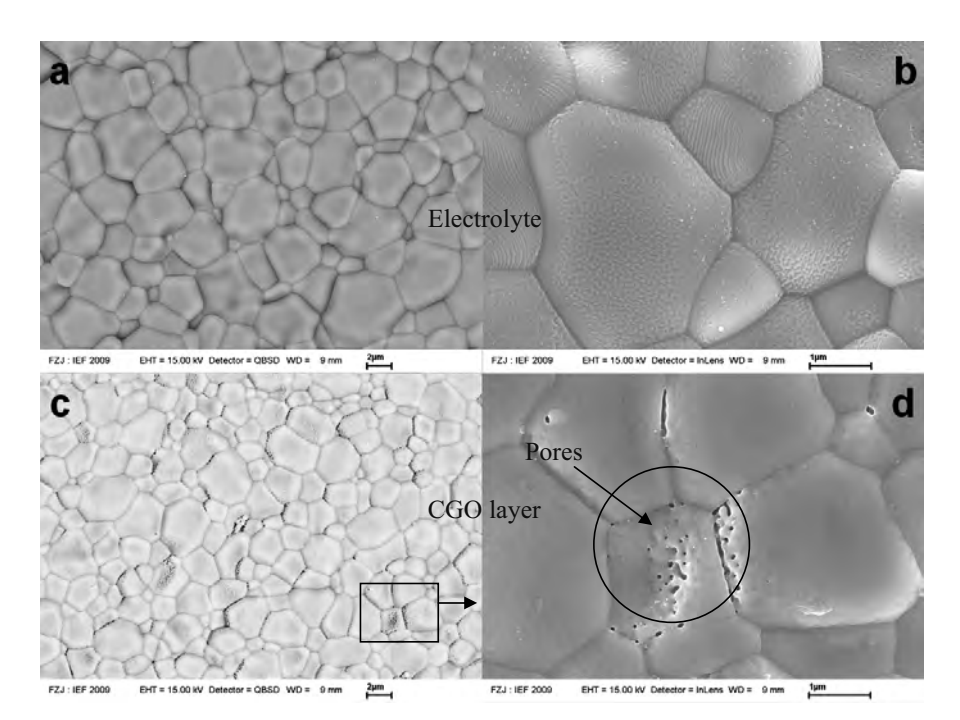


Figure 4.65 SEM surface images of the 8YSZ electrolyte and CGO barrier layers of the tested cell (cell no. 12625) in Group 3-1 with co-sintered multi-layered electrolyte: (a), (b) surface of 8YSZ electrolyte; (c), (d) surface of CGO barrier layer

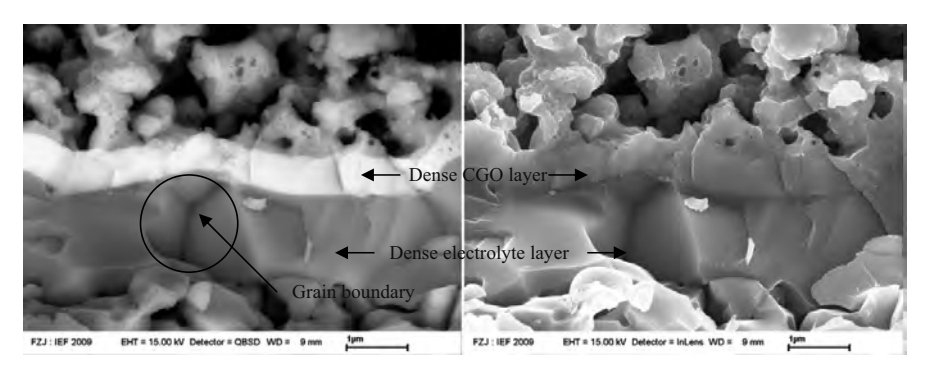


Figure 4.66 SEM fracture surface images of cell 12625 in Group 3-2 with co-sintered multilayered electrolyte

The change in the microstructure of the 8YSZ electrolyte surface is favourable for the formation of dense CGO layer by magnetron sputtering process, which effectively prevented the strontium diffusion from the $La_{0.58}Sr_{0.4}Fe_{0.2}Co_{0.8}O_{3-\delta}$ cathode to the 8YSZ electrolyte and ensured the contribution of the thickness-reduced electrolyte in

improving the overall single cell performance. No zirconate layers were formed any more and no secondary phase was observed at the 8YSZ/CGO interface, as shown in Figure 4.66. The YSZ/CGO interface is sharp and neat, indicating zirconate did not form due to the effective protection from the dense CGO layer coated on the top of the dense 8YSZ electrolyte.

In summary, the electrochemical performance of the tested single cells in Group 3-1 with co-sintered multi-layered electrolyte was significantly improved due to the electrolyte thickness reduction and effective protection form CGO diffusion barrier layer. The as-prepared electrolyte was approximately 1 µm thick, i.e. one order of magnitude thinner than the thickness of electrolyte in the conventional anode supported planar SOFCs. As no evidence of zirconate layer formation in the tested cells of Group 3-1, the positive contribution brought by the electrolyte thickness reduction was able to fully perform without counteraction from insulating layers.

As demonstrated in Figure 4.49, both of the nano-suspension-derived layers of the tested cells in Group 3-2 were deposited by dip-coating method and calcined at 1000 °C and 800 °C for 1 h, respectively. Polymeric sol was further spin coated and calcined at 500 °C for 1 h. All the layers of the electrolyte were co-sintered together in a sintering process carried out at 1400 °C for 5 h. The CGO barrier layer (~0.5 μm in thickness) was coated by magnetron sputtering at 800 °C. The LSCF cathode was screen-printed and dried at 60 °C, and finally sintered at 1040 °C for 3 h.

The helium leak rate of tested half-cells was in the range of 5.0×10^{-6} to 8.0×10^{-6} (hPa·dm³)/(s·cm²) in the oxidized state, which is slightly more gas-tight than the half-cells in the Group 3-1 with average helium leak rate of 1.2×10^{-5} (hPa·dm³)/(s·cm²). The slight improvement in the gas-tightness might be due to the fact that the dip-coated layers are normally thicker and more homogeneous than spin-coated layers by using the as-prepared nano-suspension as coating liquid.

The *i*-V curves of cell 12839 in Group 3-2 (Figure 4.67) showed the best performance among all the tested single cells using the LSCF cathode in this work. At a cell voltage of 0.7 V, the current densities of cell 12839 are 3.18, 2.77, 2.23, 1.73 and

 0.95 A/cm^2 , accordingly generating power density of 2.23, 1.94, 1.56 1.21 and 0.67 W/cm^2 , at 800, 750, 700, 650 and 600 °C, respectively. At operating temperature of 600 °C, the average current density of the tested cells is 0.94 A/cm^2 , which is as good as the reference cell operated at 650 °C, as shown in Figure 4.68.

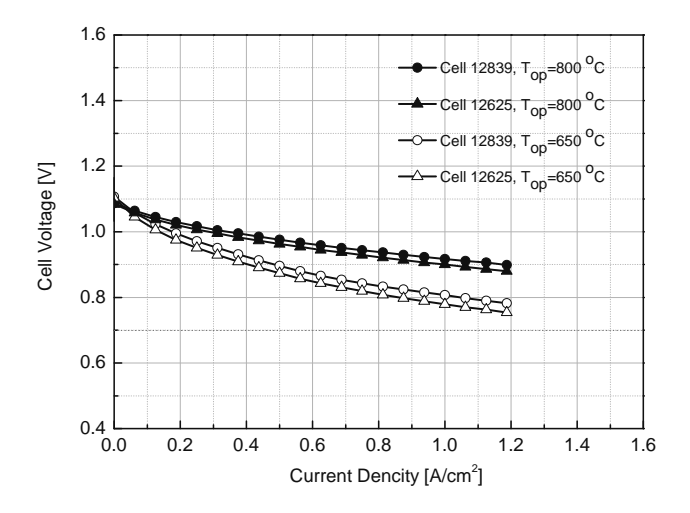


Figure 4.67 i-V curves of cell 12839 in Group 3-2 compared with cell 12625 in Group 3-1, operated at 650 and 800 $^{\circ}\mathrm{C}$

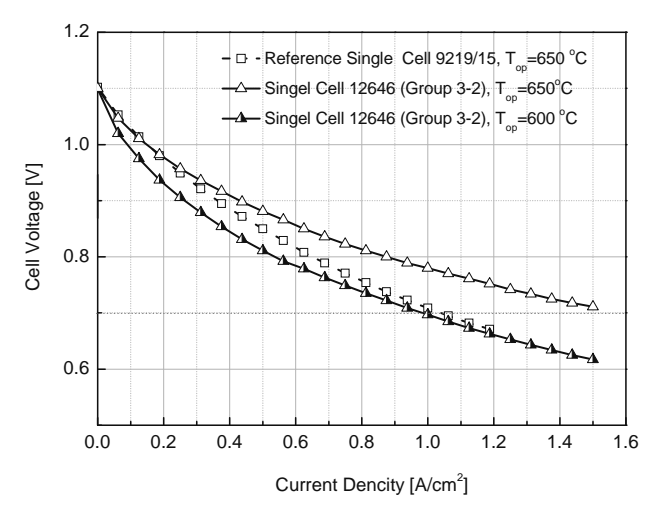


Figure 4.68 *i*-V curves of cell 12646 in Group 3-2 operated at 600 and 650 °C in comparison with reference cell 9219-15 operated at 650 °C, different from the tested cells, the reference cells are with vacuum-slip-cast electrolyte ($7\sim10~\mu m$), sputtered CGO layer (1 μm) for 3 h

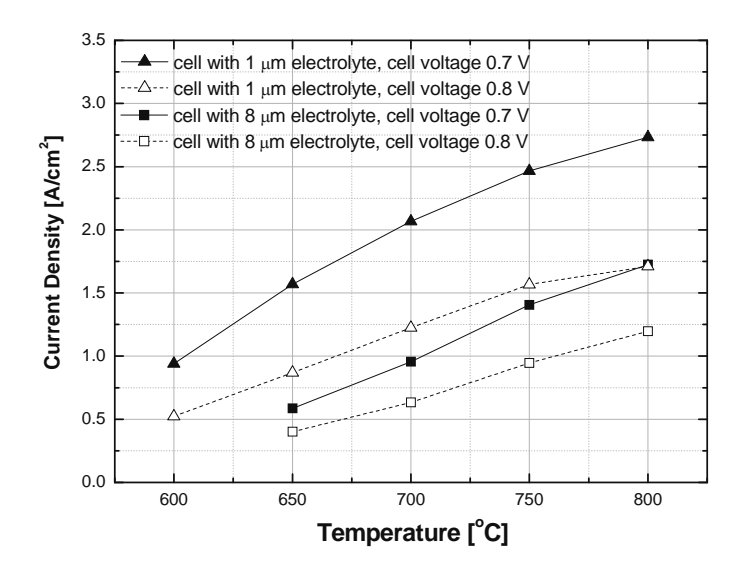


Figure 4.69 Average current density of single cells in Group 3-2 in comparison with reference cells with 8 μ m electrolyte, operated at different cell voltage and temperatures, based on data acquired in electrochemical single cell test on cells with active LSCF cathode size of 4x4 cm²

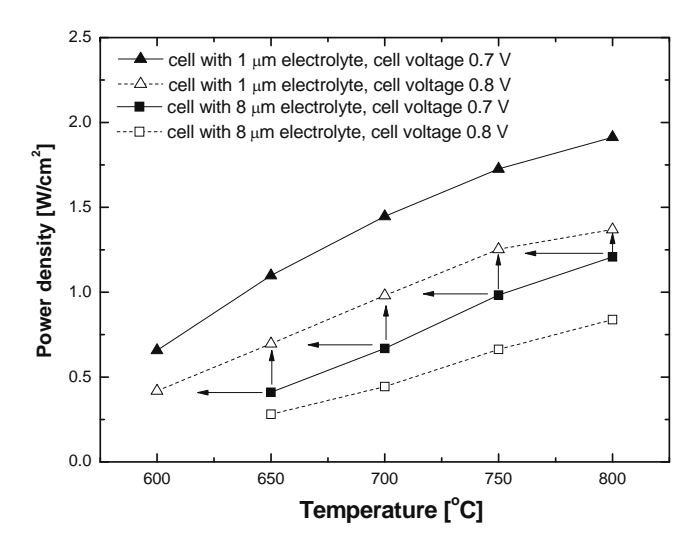


Figure 4.70 Average power density of single cells in Group 3-2 in comparison with reference cells with 8 μ m electrolyte, operated at different cell voltage and temperatures, based on data acquired in electrochemical single cell test on cells with active LSCF cathode size of 4x4 cm²

At a cell voltage of 0.8 V, the average current densities of the test cells with 1 μ m thick electrolyte are 1.71, 1.57, 1.23, 0.87 and 0.52 A/cm², accordingly generating

power density of 1.37, 1.25, 0.98 0.70 and 0.42 W/cm², at 800, 750, 700, 650 and 600 °C, respectively, as demonstrated in Figure 4.69 and Figure 4.70. These values are higher than the single cells with 8 μm thick electrolytes operated at a cell voltage of 0.7 V. The power density plot against temperature of the cells in Group 3-2 shifted to lower temperature range by 50 °C at higher operating a cell voltage of 0.8 V, marked by red arrows in Figure 4.70. Generating the same power density, the asprepared single cells with 1 μm electrolyte can be operated at a temperature 50 °C lower and a cell voltage 0.1 V higher. Due to this performance improvement, the life time of the SOFCs may be remarkably improved because the cells could be operated at less harsh conditions of lower temperature and higher cell voltage.

Temperature	ASR _{tested cell}	ASR _{reference cell}	∆ ASR _{cell}	$ASR_{1\mu mEL}$	$ASR_{8\mu mEL}$	\triangle ASR _{EL}
(°C)	$(m\Omega \cdot cm^2)$	$(m\Omega \cdot cm^2)$	$(m\Omega \cdot cm^2) / \%$	$(m\Omega \cdot cm^2)$	$(m\Omega \cdot cm^2)$	$(m\Omega \cdot cm^2)$
800	116	157	-41 / -26%	2.4	19.2	-16.8
750	126	160	-34 / -21%	3.9	31.2	-27.3
700	136	199	-63 / -32%	6.6	53.0	-46.4
650	150	245	-95 / -39%	11.9	95.5	-83.6

Table 4.15 Average ASR of tested cells in Group 3-2 compared with reference cells

As summarized in Table 4.15, the average area specific resistance (ASR) of test cells reduced to 116 and 150 m Ω ·cm² at operating temperature of 800 and 650 °C, approximately 26% and 39% lower than the ASR of the reference cells. The theoretically calculated ASR of 8 and 1 μ m thick 8YSZ electrolyte are also listed in Table 4.15. The contribution ratio of the electrolyte thickness reduction to the total single cell ASR reduction (Δ ASR_{electrolyte} / Δ ASR_{cell}) are calculated as 41%, 80%, 74% and 88% at 800, 750, 700 and 650 °C, respectively, which is in good agreement with the results of singles cells in Group 3-1. The results also proved that the electrolyte thickness played a dominating role in the reduction of the overall ASR of single cells at temperature below 750 °C. However, there might be additional effects also contributed to the total ASR reduction, such as the decrease in the number of the grain boundaries on the oxygen ion migration path and the increase of triple phase boundaries in the active part of anode layers resulted from the infiltration of the 8YSZ nano-suspension and polymeric sol with fine particles. The detailed discussion is done in the last part of this section.

The processing of electrolyte and layer structure of the single cells in Group 3-3 is demonstrated in Figure 4.49. To simplify the processing of the half-cells, the calcination of each coated 8YSZ layer was all separately carried out at 500 °C for 1 h instead of applying different temperatures. The fabrication of the CGO layer and LSCF cathode remained the same, i.e. the CGO barrier layer (\sim 0.5 μ m in thickness) was coated by magnetron sputtering at 800 °C and the LSCF cathode was screen-printed, dried at 60 °C, and sintered at 1040 °C for 3 h.

The helium leak rate of tested half-cells in Group 3-3 was in the range of $9.0x10^{-6}$ to $1.6x10^{-5}$ (hPa·dm³)/(s·cm²) in the oxidized state, which is as gas-tight as the half-cells in Group 3-2, thermally treated with the complex calcinations process and sintered at 1400 °C for 5 h.

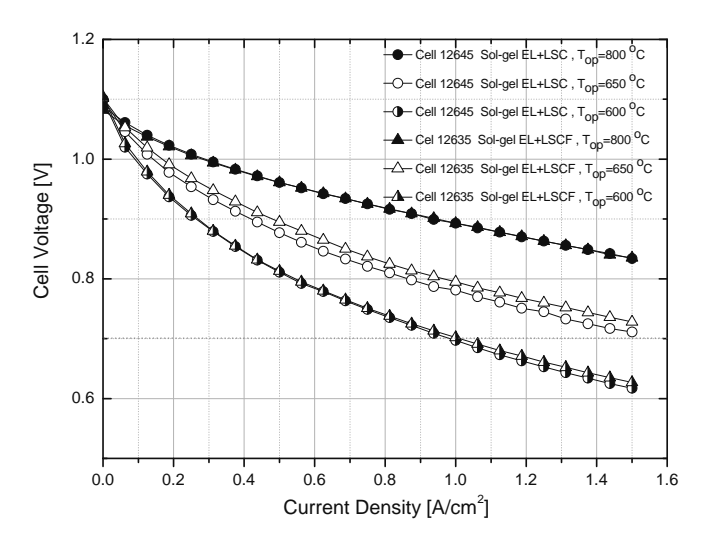


Figure 4.71 i-V curves of cell 12635 in Group 3-3 compared with cell 12645 in Group 3-2, operated at 600, 650 and 800 °C, different from the tested cells, the reference cells are with vacuum-slip-cast electrolyte (7~10 μ m), sputtered CGO layer (1 μ m

Compared with the single cells in Group 3-2, the *i*-V curves of the tested samples with 4x4 cm² active LSCF cathode in Group 3-3 (Figure 4.71) have shown no significant difference in the electrochemical performance, indicating that a simplified calcination program did not remarkably affect the cell performance. At a cell voltage of 0.7 V, the average current densities are 2.76, 2.49, 2.07, 1.68 and 0.88 A/cm², accordingly

generating power density of 1.93, 1.74, 1.45 1.18 and 0.61 $\rm W/cm^2$, at 800, 750, 700, 650 and 600 $\rm ^{\circ}C$, respectively.

Temperature	ASR _{tested cell}	ASR _{reference cell}	△ ASR _{cell}	$ASR_{1\mu mEL}$	$ASR_{8\mu mEL}$	\triangle ASR _{EL}
(°C)	$(m\Omega \cdot cm^2)$	$(m\Omega \cdot cm^2)$	$(m\Omega \cdot cm^2) / \%$	$(m\Omega \cdot cm^2)$	$(m\Omega \cdot cm^2)$	$(m\Omega \cdot cm^2)$
800	123.5	157	-33.5 / -21 %	2.4	19.2	-16.8
750	131.5	160	-28.5 / -18 %	3.9	31.2	-27.3
700	133	199	-66 / -33 %	6.6	53.0	-46.4
650	143	245	-102 / -42 %	11.9	95.5	-83.6

Table 4.16 Average ASR of tested cells in Group 3-3 compared with reference cells

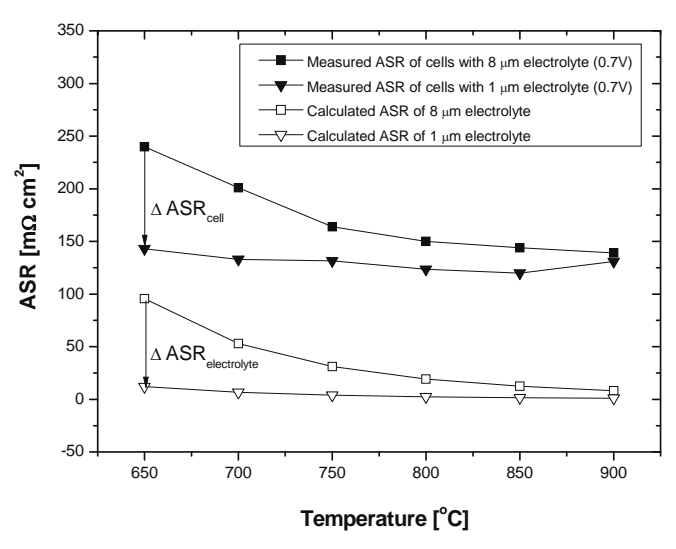


Figure 4.72 Temperature dependence of measured overall ASR of single cell and calculated ASR of 8YSZ electrolyte

As shown in Table 4.16, the average area specific resistance (ASR) of test cells in Group 3-3 is 123.5 and 143 m Ω ·cm² at operating temperature of 800 and 650 °C, approximately 21% and 42% lower than the ASR of the reference cells. As the operating temperature reduced from 800 to 650 °C, the ASR of the tested cells with 1 µm electrolyte only reduced 19.5 m Ω ·cm², while the ASR of reference cell with 8 µm electrolyte reduced 88 m Ω ·cm². The theoretically calculated ASR of 1 µm thick 8YSZ electrolyte is 16.8 and 83.6 m Ω ·cm² lower than the 8 µm thick 8YSZ electrolyte at 800 and 650 °C, respectively. The measured ASR of the tested cells and the theoretically calculated ASR of 8 and 1 µm thick 8YSZ electrolyte are plotted

over temperature Figure 4.72. The contribution of the electrolyte thickness reduction to the total single cell ASR reduction (Δ ASR_{electrolyte} / Δ ASR_{cell}) are calculated as 51%, 96%, 70% and 82% at 800, 750, 700 and 650 °C, which is in good agreement with the results of single cells in Group 3-1 and Group 3-2 and proved that the contribution of electrolyte thickness reduction is the dominating factor in the reduction of the overall ASR of single cells at temperature below 750 °C.

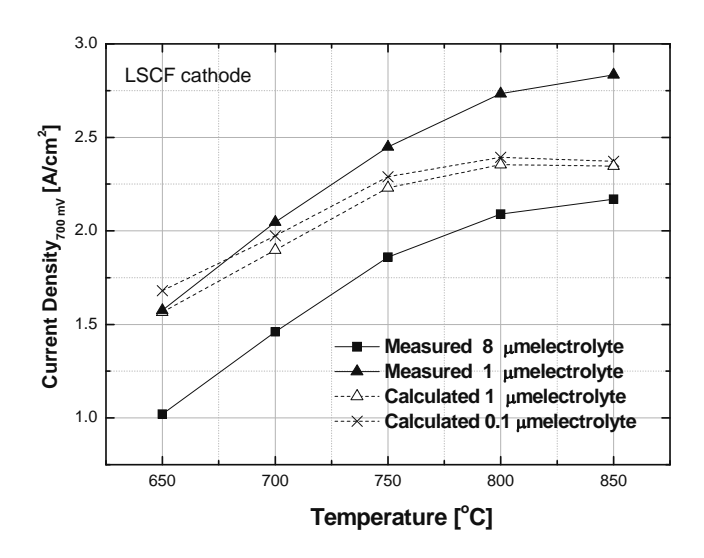


Figure 4.73 Comparison of measured and theoretically calculated current densities of the single cell with varied electrolyte thickness and $4x4 \text{ cm}^2 LSCF$ cathode

Temperature	Current density of single cells with $x \mu m$ thick electrolyte (A/cm ²)				
(°C)	<i>t</i> =8, measured	<i>t</i> =1, calculated	<i>t</i> =0.1, calculated	<i>t</i> =1, measured	
850	2.17	2.35	2.37	2.84	
800	2.09	2.35	2.39	2.73	
750	1.86	2.23	2.29	2.45	
700	1.46	1.90	1.97	2.05	
650	1.02	1.57	1.68	1.58	

Table 4.17 Comparison of measured and theoretically calculated current densities of the single cell with varied electrolyte thickness and $4x4 \text{ cm}^2 \text{LSCF}$ cathode, t is the thickness of the sintered electrolyte

Based on the measured electrochemical data of cells with 8 μ m thick electrolyte layers, the theoretical current density of single cell with 1 μ m and 0.1 μ m thick electrolyte layers were calculated and plotted over the operating temperature in Figure 4.73. Applying a linear extrapolation fitting method, the current densities of single cells with 1 μ m thick electrolyte derived from the actually electrochemical single cell test

are 1.58, 2.05, 2.45, 2.73 and 2.84 A/cm² at 650, 700, 750, 800 and 850°C, which was 0.6%, 7.9%, 9.8%, 16.1% and 20.8% higher than the theoretically calculated values. At operating temperature of 650 °C, the average current density of all the tested cells in this section with 1 µm electrolyte is 1.58 A/cm², which is in good agreement with the theoretically calculated value of 1.57 A/cm². As the operating temperature increases, the current density values are increasingly higher than the theoretically calculated values, also seen in Table 4.17. Apart from electrolyte thickness reduction, there should be other factors additionally contributing in reducing the overall ASR of the single cells and enhancing the cell performance.

First of all, the intrinsic influence of the grain boundary conductivity in 8YSZ electrolyte material may result in the difference between the measured and calculated current density values. From an electrical point of view, the grain boundary conductivity of 8YSZ is at least two orders of magnitude lower than the corresponding bulk conductivity, depending on temperature [114, 115]. A crystallographic grain boundary is normally 1 nm thick, while the electrical grain boundary can be quite large under certain conditions, e.g. a thickness of about 140 nm was determined for 0.016 wt.% Fe-doped SrTiO₃[116].

As the conductivity in the 8YSZ bulk is much higher than the conductivity at the 8YSZ/8YSZ grain boundary, the oxygen ions migrate more favourably in the bulk and cross the grain boundary, instead of migrate along the grain boundary. As a rough estimation, the grain boundary contribution to the overall resistance of a 10 µm thick 8YSZ electrolyte layer with an average grain size of 2 µm (the oxygen ions from the cathode side have to cross at least 4 grain boundaries in the electrolyte to reach the TPB reaction sites at the anode side) can be as high as 17 % by assuming a grain boundary thickness of 5 nm and two orders of magnitude in conductivity difference between bulk and grain boundaries. The estimation could be expressed by the following equation:

$$\eta = \frac{R_{gb}}{R_{bulk} + R_{gb}} = \frac{t_{gb}\rho_{gb}}{t_{bulk}\rho_{bulk} + t_{gb}\rho_{gb}} = \frac{\frac{t_{gb}}{\sigma_{gb}}}{\frac{t_{bulk}}{\sigma_{bulk}} + \frac{t_{gb}}{\sigma_{gb}}} = \frac{t_{gb}\sigma_{bulk}}{t_{bulk}\sigma_{gb} + t_{gb}\sigma_{bulk}}$$
Equation 4.2

where η is the grain boundary contribution to the overall resistance, t_{gb} is the total grain boundary thickness, t_{bulk} is the total bulk thickness, ρ_{bulk} is bulk resistivity, ρ_{gb} is grain boundary resistivity, σ_{bulk} and σ_{gb} are bulk conductivity and grain boundary conductivity, respectively.

As found in the SEM images of the as-prepared samples in this section, the sintered electrolyte layers are approximately 1 μ m (Figure 4.66) in thickness and mainly consist of grains larger than 1 μ m (Figure 4.65). The grains should be flat-shaped or partly inserted into the anode. In the case of thicker electrolyte (7 to 10 μ m) in conventional anode-supported SOFCs, the oxygen ions have to cross several grain boundaries inside the electrolyte before reaching the reaction active TPBs at the anode/electrolyte interface. In the case of the as-prepared thin electrolyte (approximately 1 μ m), the oxygen ions can migrate through the bulk 8YSZ electrolyte from the cathode to the anode without crossing more than one grain boundary. Thus, the conductivity of the electrolyte layers is additionally enhanced by removing the grain boundaries in the oxygen transportation path. In another word, large grain size could result in low amount of grain boundaries (low grain boundary resistivity) and high overall electrolyte conductivity in SOFCs.

Given 8YSZ as the electrolyte material and layer thickness, it is suggested that dense electrolyte with larger grain size and less grain boundaries should have higher ionic conductivity than the electrolyte with smaller grain size. Technically, the sintering temperature of electrolyte could be reduced down to 1000 °C by applying nanoprocessing technologies, such as sol-gel method. On one hand, this could bring many benefits, including lower fabrication cost, possibility to co-sinter 8YSZ electrolyte with CGO diffusion barrier layer without forming ionic insulating compound, and more material choices in developing metal porous substrate supported SOFCs. On the other hand, the grain size of the electrolyte sintered at reduced temperature (around 1000 °C) might be so small that large amount of grain boundaries may bring down the total conductivity of the electrolyte.

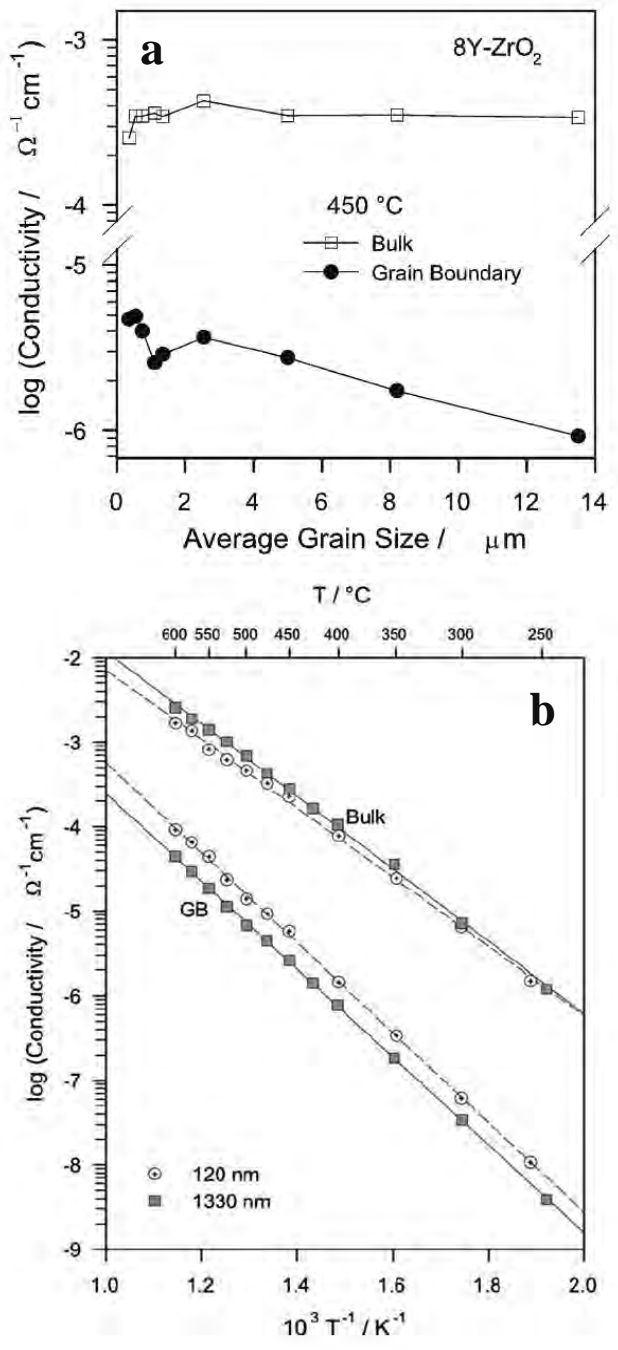


Figure 4.74 (a) Bulk conductivities and specific grain-boundary conductivities as a function of average grain size for 8.2 mol% YSZ at $450 \,^{\circ}$ C and the specific grain-boundary conductivities are re-calculated by assuming a grain-boundary thickness of $5.0 \, \text{nm} [117]$. (b) Temperature dependence of bulk conductivities and specific grain boundary conductivities for $3 \, \text{mol}\%$ YSZ samples with an average grain size of $120 \, \text{and} \, 1330 \, \text{nm}$, respectively [115].

Secondly, the heat generated by the cells at high operating temperature is the extrinsic factor, which may also contribute to the difference between the measured and calculated current density values. The total current generated by the cells with 4x4 cm² active cathode area is in the range of 30 to 45 A at operating temperature over 700 °C. Such high current generates enormous heat, which could significantly raise the actual temperature in the cells under operation and remarkably increase the migration rate of the oxygen ions in the electrolyte, as well as the measured current density, because the conductivity of 8YSZ electrolyte is temperature dependent. More detailed discussion on this issue is also presented in the corresponding part of section 4.3.5 and Figure 4.85.

Thirdly, the infiltration of nano-suspension and polymeric sol into the anode layer may change the microstructure near the electrolyte/anode interface and increase the total area of triple phase boundaries, which could result in a higher ionic conductivity, lower contact resistance and less activation polarization losses at the reaction active part of the anode layers. Although this assumption was not able to be resolved in the following section 4.3.4 on electrochemical impedance spectroscopy characterization of the as-prepared single cells, it could be experimentally verified in the future work by testing single cells with nano-suspension layer and polymeric sol-gel layer in between the conventionally deposited electrolyte layer and the anode, which should have the same overall thickness as the conventional screen-printed or vacuum-slip-cast electrolyte. If no performance enhancement could be observed on the specially prepared single cells, the contribution of electrolyte/anode interface modification due to the infiltration of the nano-suspension and polymeric sol could be neglected, otherwise, it should be taken into consideration for the explanation of the enhanced cell performance.

4.3.4 Electrochemical impedance spectroscopy (EIS)

Anode-supported cells with thin 8YSZ electrolyte (prepared as described in section 4.3.3, Group 3-2) and 1x1 cm² cathode with auxiliary (OCV probe) electrode (as illustrated in Figure 4.75) are characterized with electrochemical impedance spectroscopy. The characterization and data processing are carried out by the Institute

of Materials for Electrical and Electronic Engineering at Karlsruhe Institute of Technology.

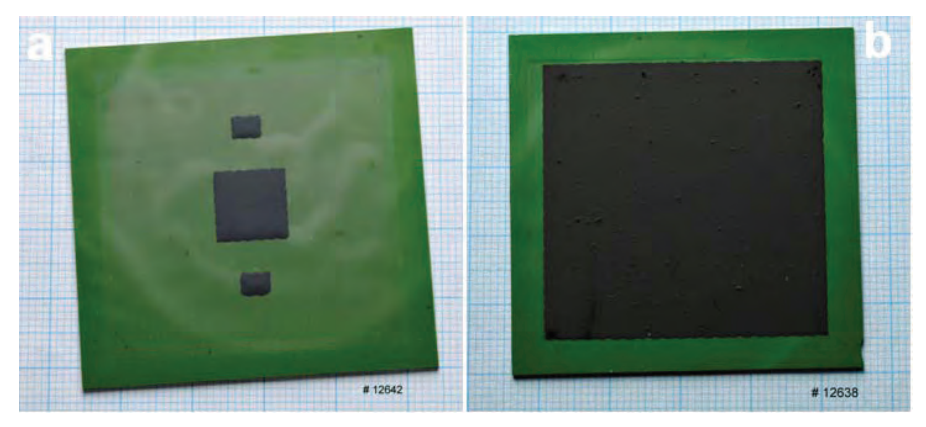


Figure 4.75 Picture of single cells: (a) coated with 1x1cm² cathode for electrochemical impedance microscopy characterization, (b) coated with 4x4cm² cathode for electrochemical single cell test

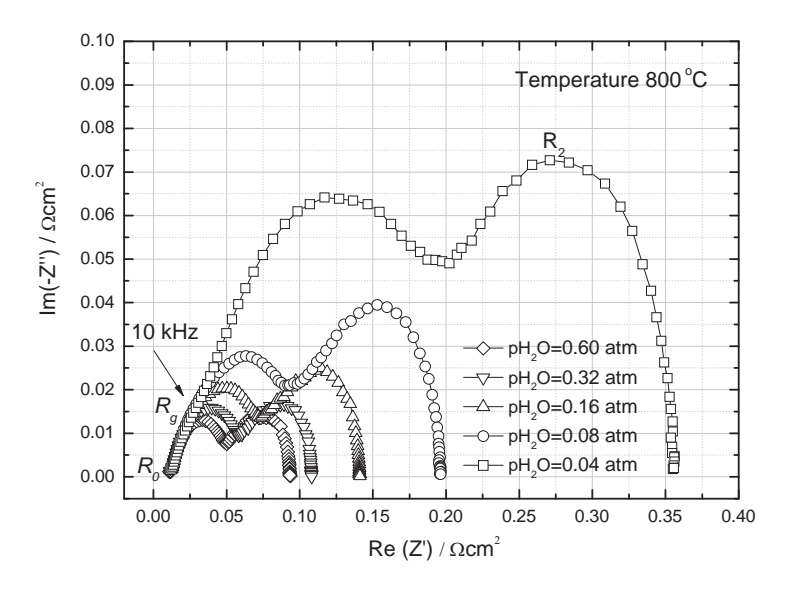


Figure 4.76 Impedance spectra of single cell tested at 800 $^{\circ}$ C under varied pH_2O

Figure 4.76 shows impedance spectra of tested cell under different pH_2O at the anode side. The high frequency intercept (R_0) of the real axis (Z') exhibited no dependence on pH_2O . R_0 represents the bulk resistance of the 8YSZ electrolyte layer [118]. The value R_g in the frequency range of around 10 kHz is also independent of p_{H2O} and can

be considered as the grain boundary resistance of the 8YSZ particles in the anode support. On the other hand R_g can also be considered as the part of anode polarization resistance which is independent of cathode polarization.

The impedance spectra are also obtained by testing the single cell at varied temperatures between 550 and 850 °C in steps of 10 K with H₂ (6.0-5.5 vol. % H₂O) as fuel gas, while the fuel gas utilization rate and other parameters remains constant. The Arrhenius plots of the ohmic resistance (R_{0}) and each single polarization resistance (R_{1A} , R_{2A} , R_{3A} , and R_{2C}), obtained by analyzing the impedance spectra with a complex nonlinear least-squares (CNLS) approximation [108], are represented in Figure 4.77 and Figure 4.78, respectively.

The high frequency intercept (R_θ) of the real axis (Z'), as the ohmic resistance of the electrolyte, exhibited temperature dependence. Under the given test condition, the measured R_θ are 12, 17, 25, 44, 77 and 167 m Ω at 800, 750, 700, 650, 600 and 550 °C, which is almost one order of magnitude lower than the corresponding values measure on the reference cells with conventional electrolyte (7 to 10 μ m thick) and screen printed CGO layer, as precisely observed in Figure 4.77.

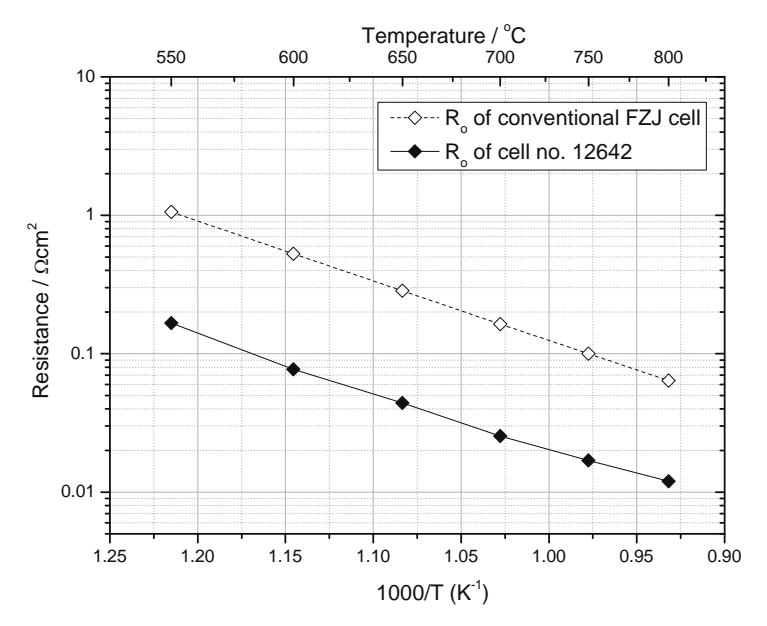


Figure 4.77 Temperature dependence of ohmic resistance

It is evident that the processes of oxygen surface exchange kinetics and O^{2-} diffusivity at the anode side (process P_{2A} and process P_{3A}) and the gas diffusion coupled with charge transfer reaction and ionic transport at the cathode side (process P_{2C}) are all characterized by a distinct thermal activation. Process of gas diffusion at anode side (process P_{1A}) shows a negligible dependency on the operating temperature. The resistances R_{2C} and $(R_{2A}+R_{3A})$ can be approximated well with a linear fit, demonstrating good Arrhenius behaviours.

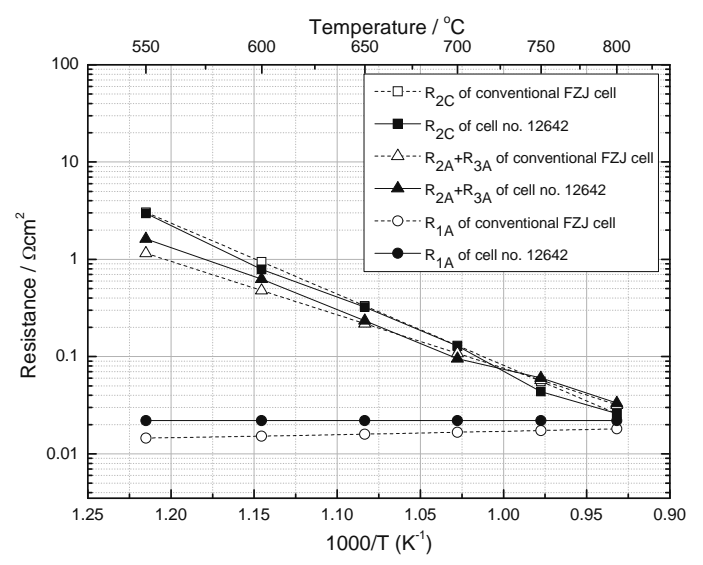


Figure 4.78 Temperature dependence of polarization resistance

As observed, the R_{2A} and R_{3A} in good agreement with the values of standard FZJ cells with screen-printed CGO barrier layer and cathode, whereas the resistances R_{2C} shows a same linear trend in the logarithmic plane with same slope. According to S. B, Adler's work [119], the high-frequency process of the cathode (process P_{2C}) is probably associated with the oxygen surface exchange kinetics of LSCF as well as the diffusivity of oxygen ions through the LSCF bulk. The low-frequency process of the cathode (process P_{1C}) probably reflects the mass-transfer resistance caused by the gasphase diffusion in the pores of the LSCF electrode.

In Figure 4.79, the polarization resistances of the anode obtained from the CNLS fit are plotted over the water partial pressure. During this fit procedure, the resistance

 $R_{\rm 2C}$ was kept fixed in order to ensure a stable fit. The polarization contribution caused by the gas-phase diffusion in the pores of the LSCF electrode can be neglected when air is used as cathode gas, then the resistance $R_{\rm 1C}$ was set constant to zero. $R_{\rm 1A}$ shows the higher dependence on changes in the water content than $(R_{\rm 2A} + R_{\rm 3A})$. The total resistances of $(R_{\rm 2A} + R_{\rm 3A})$ show an almost linear trend in the double-logarithmic plane with same slopes as the plot of the conventional FZJ cells.

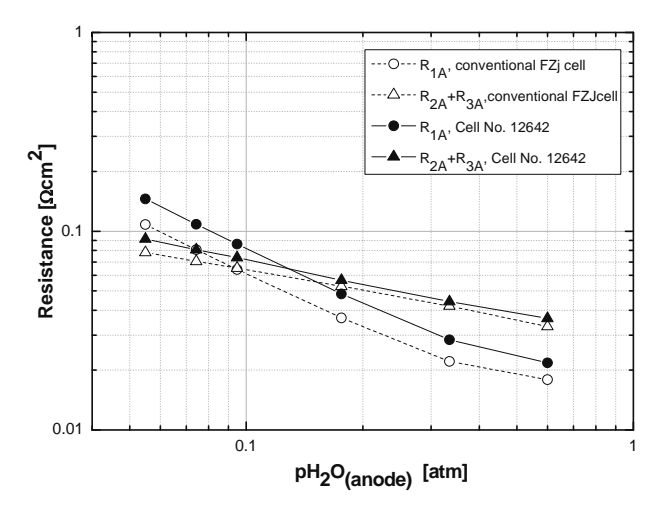


Figure 4.79 pH₂O-dependance of loss process on anode side

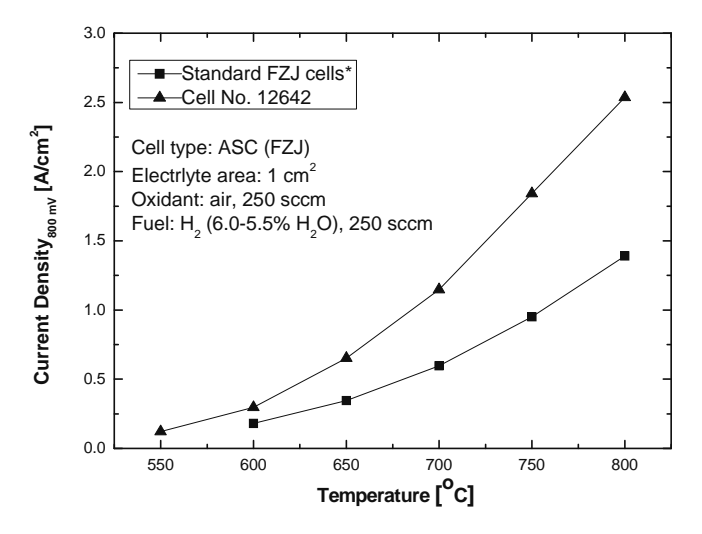


Figure 4.80 Current density of the single cell with 1x1 cm² LSCF cathode, operated at a cell voltage of 0.8 V and varied temperatures

During the EIS investigation, the power output is also tested and plotted over operating temperature in Figure 4.80. At a cell voltage of 0.8 V, the measured current densities are 2.54, 1.84, 1.15, 0.65, 0.30 and 0.12 A/cm², accordingly generating power density of 2.03, 1.47, 0.92, 0.52, 0.24 and 0.10 W/cm², at 800, 750, 700, 650, 600 and 550 °C, respectively. The fuel gas input are 250 sccm/cm² for single cells with 1x1 cm² cathode and 62.5 sccm/cm² for single cells with 4x4 cm² cathode, respectively. At high operating temperature (800 °C), the current density is relatively high and the fuel gas utilization may dominate the power output of the single cells. As a result, the cells with higher fuel gas input has higher power output, as compared in Table 4.18.

Operating temperature [°C]	Current density @ 0.8 V cell voltage [A/cm²]					
	Cathode size	ze 1x1 cm ²	Cathode size 4x4 cm ²			
	Fuel gas inp	ut 250 sccm	Fuel gas input 1000 sccm			
	1 μm electrolyte	8 μm electrolyte	1 μm electrolyte	8 μm electrolyte		
800	2.54	1.39	1.71	1.20		
750	1.84	0.95	1.57	0.95		
700	1.15	0.60	1.23	0.63		
650	0.65	0.35	0.87	0.40		
600	0.30	0.18	0.52	-		

Table 4.18 Comparison of measured and theoretically calculated current densities of the single cell with varied electrolyte thickness and cathode size

At low operating temperature (650 and 600 °C), the transportation rate of oxygen ions in electrolyte decreases exponentially and plays a more important role for the cell power output. The total current generated by the cell with 4x4 cm² cathodes is in the range of 8 to14 A, which is at least one order of magnitude higher than the total current generated by the cell with 1x1 cm² cathodes. The actual temperature in the cells with large cathode should be remarkably higher than in the cells with smaller cathode due to the heat generated by the high current, which could significantly increase the oxygen ionic conductivity of the electrolyte layers and result in current density enhancement.

4.3.5 Single cells with co-sintered multi-layered electrolyte, CGO layer and LSC cathode (Group 4-1)

The processing of electrolyte and layer structure of single cells in Group 4-1 with La $_{0.58}$ Sr $_{0.40}$ CoO $_{3-\delta}$ (LSC) cathode reported in this section is also demonstrated in Figure 4.49. The thin electrolyte was coated on tape-cast anode substrates in the same way as described with single cells of Group 3-2 in section 4.3.3. The first layer was dip-coated with 8YSZ nano-suspension and calcined at 1000 °C. The second layer was also dip-coated with 8YSZ nano-suspension, but calcined at 800 °C. Polymeric sol was further spin-coated and calcined at 500 °C. Finally all the calcined 8YSZ layers were co-sintered at 1400 °C for 5 h. The CGO barrier layer (~0.5 μ m in thickness) was coated by magnetron sputtering at 800 °C. The LSC cathode was screen-printed and dried at 60 °C, and finally sintered at 800 °C for 1 h.

The samples with active LSC cathode area of 4x4 cm² showed extremely good electrochemical performance, as seen in Figure 4.81 and Figure 4.82 and Table 4.19. The maximum current densities (extrapolated) are 4.62, 2.75, and 1.79 A/cm² at 800, 650 and 600 °C, respectively. By applying a 1 μm thick electrolyte instead of an 8 μm thick electrolyte, the current densities as well as power densities of the cells at 0.7 V increased 50%, 92% and 133% at 800, 650 and 600 °C, respectively. In comparison with the cells with 1 μm thick electrolyte and LSCF cathode, the performance of the as-prepared cells with LSC cathode increased 60%, 75% and 95% at 800, 650 and 600 °C, respectively. Obviously, the reduction of the electrolyte thickness is more effective than the replacement of the LSCF cathode material into LSC at lower operating temperature range. With the positive effects of both electrolyte thickness reduction and the application of high performance LSC cathode, the overall short-term electrochemical performance enhancement of the as-prepared cells, in comparison with state of the art cells with 8 μm thick electrolyte, sputtered CGO layer and LSCF cathode, are 115% and 170% at 800 and 650 °C, respectively.

In fact, the current density can hardly reach the extrapolated value partly due to the limitation of hydrogen transportation and fuel utilization rate under high current condition. The current collected from the single cell with an active cathode area of 4x4 cm² could exceed 25 A at 650 °C with both LSC and LSCF cathode and produce enormous heat, which the may melt the Pt wires of the circuit in the testing platform.

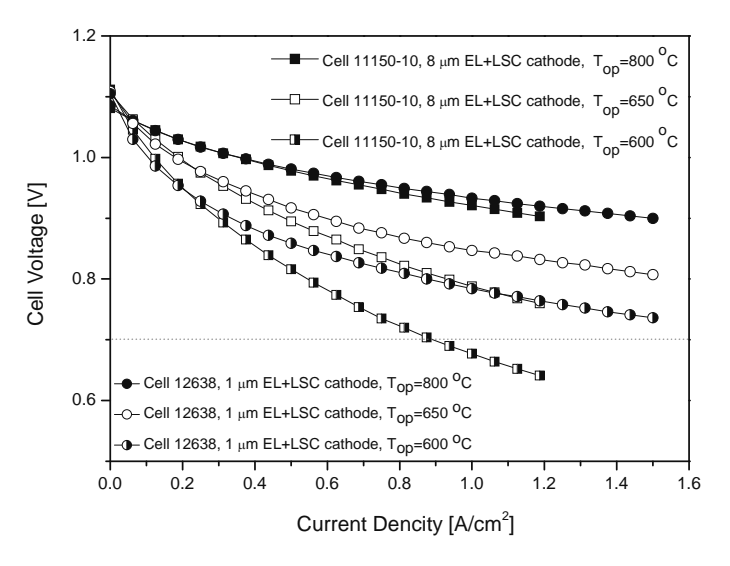


Figure 4.81 i-V curves of cell 12638 in Group 4-1 compared with cell 11150-10 with 8 μ m electrolyte, operated at 600, 650 and 800 °C, Different from the tested cells, the reference cells are with vacuum-slip-cast electrolyte (7~10 μ m), sputtered CGO layer (1 μ m), and the LSC cathode of reference cells is calcined at 850 °C for 3 h.

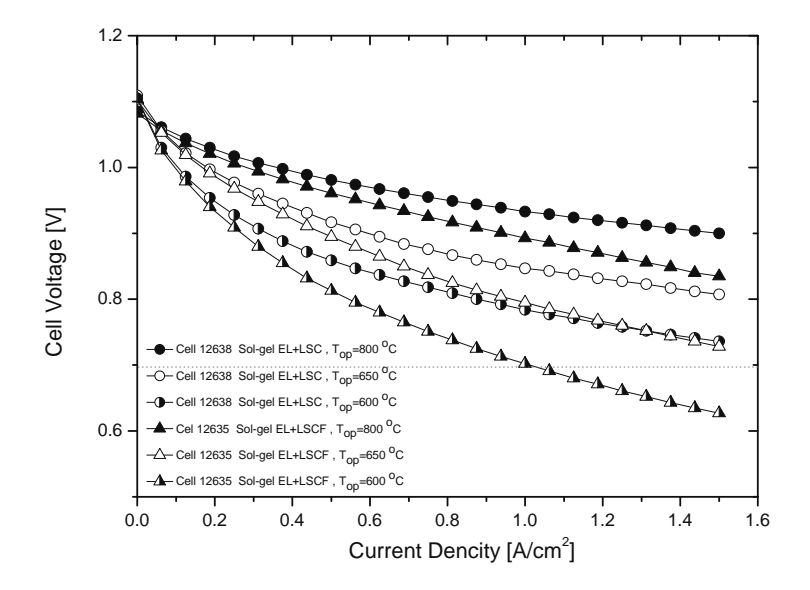


Figure 4.82 *i*-V curves of cell 12638 in Group 4-1 compared with cell 12625 in Group 3-3 with LSCF cathode, operated at 600, 650 and 800 °C, Different from the tested cells, the reference cells are with vacuum-slip-cast electrolyte ($7\sim10~\mu m$), sputtered CGO layer ($1~\mu m$)

		Cell information			
Substrate	~500 µm				
Anode	7 μm				
Electrolyte	1 µm 8 µm 1 µm 8 µг				
CGO Layer	0.5 μm	1 μm	0.5 μm	1 μm	
Cathode	LSC 50 μm LSCF 50 μm				
T (°C)	Extrapolated / measured average current density (A/cm²)				
900	4.42	3.40	2.63	1.99	
850	4.62	3.27	2.87	2.16	
800	4.39	2.92	2.73	2.04	
750	3.80	2.50	2.47	1.87	
700	3.37	2.10	2.07	1.46	
650	2.75	1.43	1.57	1.02	
600	1.86	0.80	0.96	-	

Table 4.19 Average current density of cells with different electrolyte and CGO layer thickness, cell size 5x5 cm², cathode size 4x4 cm²

Despite the excellent short-term electrochemical performance, the LSC cathode has compatibility problems with 8YSZ electrolyte due to its high thermal expansion coefficient ($17\sim20x10^{-6}~\text{K}^{-1}$ [120]) when compared to that of 8YSZ ($10.3x10^{-6}~\text{K}^{-1}$ [13]) and also due to it high degradation rate. In our experiment, the calcined LSC cathode is partly delaminated from the half-cells in the cooling-down step after the single cell test, as shown in Figure 4.83.



Figure 4.83 Pictures of an electrochemical tested single cell with 1 μm electrolyte and an LSC cathode

Based on the measured electrochemical results of cells with 8 µm thick electrolyte layer and LSC cathode, the theoretical current density of single cell with 1 and 0.1 µm electrolyte layers were calculated and plotted over the operating temperature in Figure 4.84 and listed in Table 4.19. The linearly extrapolated current densities derived from the actually tested results of cell with 1 µm electrolyte are 1.86, 2.75, 3.37, 3.80, 4.39 and 4.62 A/cm² at 600, 650, 700, 750, 800 and 850°C, which was 2.8%, 3.4%, 13.3%, 20.3%, 28.0% and 25.5% higher than the theoretically calculated values. At operating temperature of 600 °C and 650 °C, the average current density of the tested cells with 1 μm electrolyte is in good agreement with the theoretically calculated value. As the operating temperature increases, the extrapolated current density values based on measured i-V curves are increasingly higher than the theoretically calculated values. Apart from electrolyte thickness reduction, the intrinsic contribution from the reduced total grain boundary resistance in the electrolyte and the extrinsic contribution from the raised temperature in the tested cells due to high total current colleted from the cells with cathode area of 4x4 cm² might be important reasons for the additional increase of the current density.

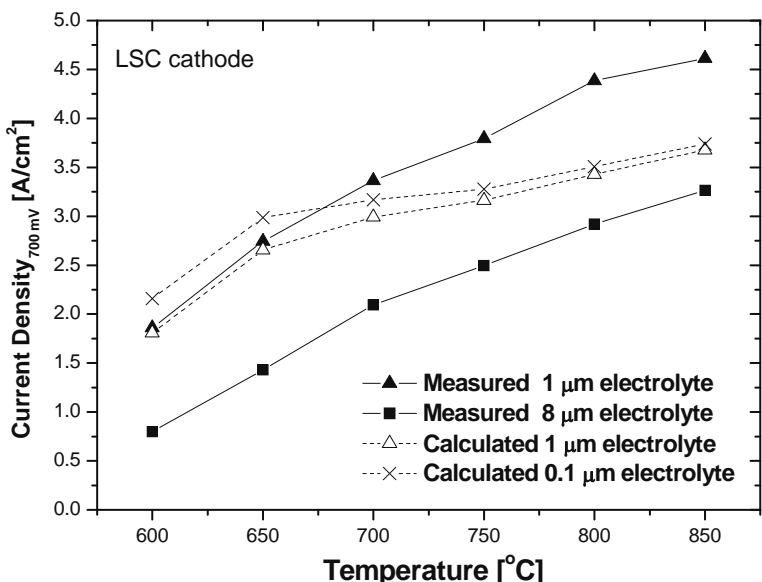
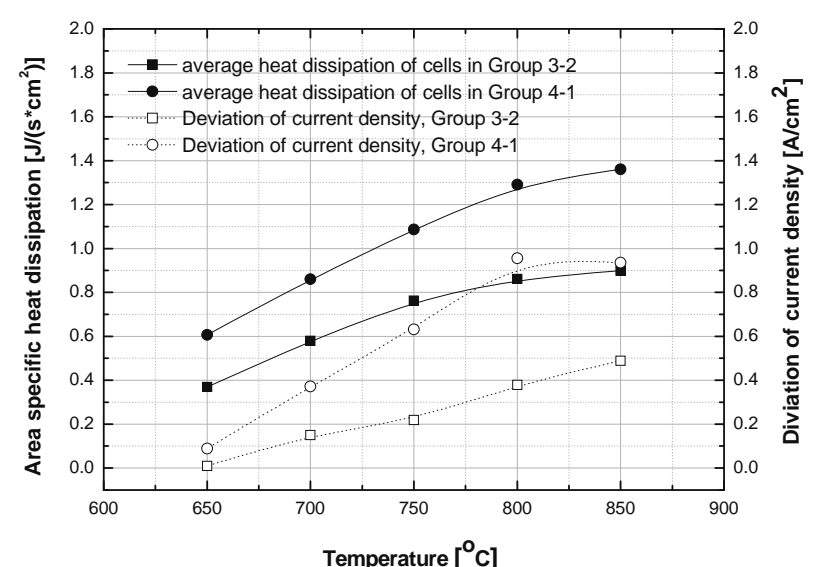


Figure 4.84 Comparison of measured and theoretically calculated current densities of the single cell with 4x4 cm² LSC cathode

Operating	Curren	Deviation	Deviation in	
temperature[°C]	Calculated [A/cm ²]	Measured [A/cm ²]	[A/cm ²]	percentage
850	3.68	4.62		25.5%
800	3.43	4.39	0.96	28.0%
750	3.16	3.80	0.64	20.3%
700	3.00	3.37	0.37	12.3%
650	2.66	2.75	0.09	3.4%
600	1.81	1.86	0.05	2.8%

Table 4.20 Comparison of measured and theoretically calculated current densities of the single cell with 1 μ m thick electrolyte



Temperature [$^{\circ}$ C] Figure 4.85 Solid line: average area specific heat dissipation rate of cells in Group 3-2 and Group 4-1; dot line: deviation between measured average current density of cells in Group 3-2 and Group 4-1 from the corresponding theoretically calculated average current density of cells with 1 μ m 8YSZ electrolyte layer

The average area specific heat dissipation rate $ASQ_{Heat-dissipation}$, in the unit of $J/(s \cdot cm^2)$ or W/cm^2 , of the cells is calculated by the following equation:

$$ASQ_{Heat-dissipation} = I^2 \bullet ASR$$
 Equation 4.3

Where I is the current density of the cell, ASR is the corresponding area specific resistance depending on operation conditions. As demonstrated in Figure 4.85, the

deviation between current density of cells in Group 3-2 and Group 4-1 from the corresponding theoretically calculated current density of cells with $1\,\mu m$ 8YSZ electrolyte layer increases in a similar way as the average area specific heat dissipation rate, which depends on the operating temperature of the cells. This observation may also serve as an important evidence for the positive influence of the heat dissipation on the electrolyte and cell performance.

4.3.6 Summary of electrochemical characterizations

The current density of all the tested cells and average current density of cells in each group are plotted over temperature in Figure 4.86 and Figure 4.87. As shown in Figure 4.86, the samples demonstrated good reproducibility except for the cells in Group 2-2. The samples in Group 3-1, 3-2, 3-3 and 4-1 have definitely better performance than the cells with conventionally deposited electrolyte layers.

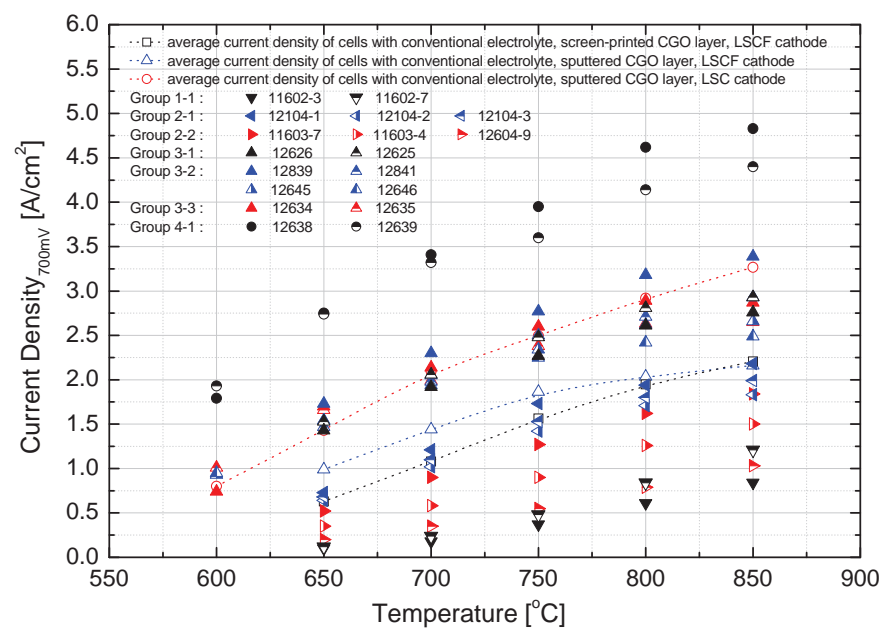


Figure 4.86 Current density values of all the tested samples over temperature in comparison with values obtained from state of the art FZJ cells, the detailed configurations of tested cells are presented in Figure 4.49. Different from the tested cells, the reference cells are with vacuum-slip-cast electrolyte (7~10 μ m), screen-printed CGO layer (10 μ m) or sputtered CGO layer (1 μ m), and the LSC cathode of reference cells is calcined at 850 °C for 3 h.

The as-prepared single cells showed excellent electrochemical performance. At a cell voltage of 0.7 V, the current density of the best performed cells (with LSCF cathode) reached 3.2, 1.7 and 1.0 A/cm² at 800, 650 and 600 °C, respectively. Generating the same power density, the as-prepared single cells can be operated at a temperature 50 °C lower and a cell voltage 0.1 V higher than the conventional cells manufactured in Forschungszentrum Jülich. By applying LSC cathode, the power output of the asprepared SOFCs is remarkably higher than the cells with LSCF cathode, and the maximum current density of such cells reached 4.6, 2.8 and 1.9 A/cm² at 800, 650 and

600 °C, respectively. However, the mismatch in expansion coefficients between the LSC cathode and the 8YSZ electrolyte remains an unsolved issue and caused delamination of the cathode.

Results of cells in Group 1-1 and 2-1 showed that a vacuum-slip-cast intermediate layer made from suspension is not necessary for the preparation of gas-tight thin electrolyte. By co-sintering the 8YSZ layers deposited with nano-suspension and polymeric sol at 1400 °C for 5 h, dense electrolytes are prepared. The OCV of the prepared cells are very close to the theoretical values derived from Nernst equation and slightly better than the conventional FZJ cells. The average current density of cells in Group 3-1, 3-2 and 3-3 are almost the same (seen in Figure 4.87), indicating that the variation with processing parameters in this work do not play a significant role on the cell performance.

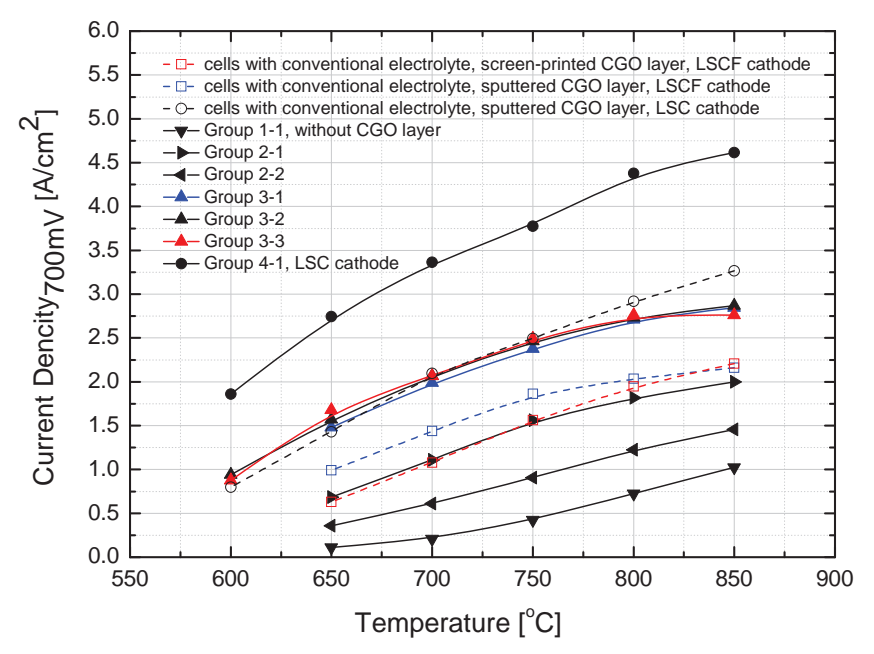


Figure 4.87 Average current density values over temperature in comparison with reference values obtained from state of the art FZJ cells, the detailed configurations of tested cells are presented in Figure 4.49. Different from the tested cells, the reference cells are with vacuum-slip-cast electrolyte (7~10 μm), screen-printed CGO layer (10 μm) or sputtered CGO layer (1 μm), and the LSC cathode of reference cells is calcined at 850 °C for 3 h

According to the EIS characterization of cells with 1x1 cm² cathode, the improvement

in the cell performance is mainly caused by an the enhanced oxygen ionic transportation through the thinner electrolyte, i.e. resulted from the decreased ohmic resistance of the electrolyte, while the polarization resistance of the as-prepared cells remained unchanged in comparison with the reference cells.

5 Summary

Solid oxide fuel cells (SOFC) are high efficiency energy converters for electricity generation. To realize a successful commercialization, goals for cost reduction and long term stability must be fulfilled. The reduction of operating temperature is one of the most promising solutions. However, the conductivity of the 8YSZ electrolyte decreases remarkably at low operating temperatures, resulting in poor cell performance. Solutions must be found in order to bring down the resistance of the cells and to achieve excellent cell performance. In this work, wet-chemical processing methods were applied to fabricate gas-tight thin electrolyte layers on planar anode substrates for SOFC applications.

First of all, sols and nano-suspensions with well-defined particle size distribution and graded mean particle size (d_{50}) in the range from 5 nm to 100 nm were successfully prepared via polymeric or colloidal sol-gel route, as well as via processing of commercial oxide particles.

Secondly, 8YSZ electrolyte layers with thickness 1 to 3 μ m were deposited on anode substrate with screen-printed anode layer via dip-coating and spin-coating procedures. Plenty of work has been done in order to optimize the layer deposition parameters. The as-prepared half-cells in this work are as gas-tight as the conventionally fabricated cells by Forschungszentrum Jülich, which have $7{\sim}10~\mu$ m thick electrolyte layers with average helium leak rates lower than $2.0 \times 10^{-5}~(hPa\cdot dm^3)/(s\cdot cm^2)$.

In the third part, single cells with varied layer configuration were prepared and comprehensive electrochemical characterizations were carried out on these cells. The as-prepared single cells showed excellent electrochemical performance. At a cell voltage of 0.7 V, the maximum extrapolated/measured current densities of the cells, with 1 µm 8YSZ electrolyte, 0.5 µm CGO diffusion barrier layer and LSCF cathode, are 3.2, 2.8, 2.3, 1.7 and 1.0 A/cm² at 800, 750 °C, 700 °C, 650 °C and 600 °C, respectively. Generating the same power density, the as-prepared single cells can be operated at temperature 50 °C lower and a cell voltage 0.1 V higher than the standard

cells manufactured in Forschungszentrum Jülich. By applying a LSC cathode, the power output of the as-prepared SOFCs is remarkably higher than those of the cells with LSCF cathode, and the maximum current density of such cells reached 4.6, 2.8 and 1.9 A/cm² at 800, 650 and 600 °C, respectively. However, the mismatch in expansion coefficients between the LSC cathode and the 8YSZ electrolyte remains an unsolved issue and caused delamination of the cathode.

The electrochemical impedance spectroscopy (EIS) confirmed that the improvement in the cell performance is mainly caused by decreased ohmic resistance of the electrolyte, while the polarization resistance of the as-prepared cells remained unchanged in comparison with standard reference cells. The area specific ohmic resistances of the single cells are 12 and 44 m Ω ·cm² at 800 and 650 °C, respectively, which is more than 80% lower than the conventional SOFCs with 10 μ m thick electrolyte manufactured by Forschungszentrum Jülich.

The cells developed in this work are the SOFCs with the highest power density ever since reported. Due to the excellent performance, the life time and stability of the SOFCs is expected to be improved by operating the cells at reduced temperature and increased cell voltage.

6 References

- [1] J. Tachtler, T. Zweimuller, and R. Hoppler, "Potentials of fuel cell APU for future power nets," *Innovative Power Trains Systems*, 1704, 375-391, 2002.
- [2] P. Lamp, J. Tachtler, O. Finkenwirth, S. Mukerjee, and S. Shaffer, "Development of an Auxiliary Power Unit with Solid Oxide Fuel Cells for Automotive Applications," *Fuel Cells*, 3, 146-152, 2003.
- [3] M. Dokiya, "SOFC system and technology," Solid State Ionics, 152, 383-392, 2002.
- [4] G. A. Tompsett, C. Finnerty, K. Kendall, T. Alston, and N. M. Sammes, "Novel applications for micro-SOFCs," *Journal of Power Sources*, 86, 376-382, 2000.
- [5] C. Peters, "Grain-size effects in nanoscaled electrolyte and cathode thin films for solid oxide fuel cells (SOFC)," in *Fakultät für Elektrotechnik und Informationstechnik*. Karlsruhe: Universität Karlsruhe (TH), 2008, 3.
- [6] A. Weber, B. Sauer, A. C. Muller, D. Herbstritt, and E. Ivers-Tiffee, "Oxidation of H₂, CO and methane in SOFCs with Ni/YSZ-cermet anodes," *Solid State Ionics*, 152, 543-550, 2002.
- [7] V. Alzate-Restrepo, and J. M. Hill, "Carbon deposition on Ni/YSZ anodes exposed to CO/H₂ feeds," *Journal of Power Sources*, 195, 1344-1351, 2010.
- [8] V. Alzate-Restrepo, and J. M. Hill, "Effect of anodic polarization on carbon deposition on Ni/YSZ anodes exposed to methane," *Applied Catalysis a-General*, 342, 49-55, 2008.
- [9] H. Kishimoto, T. Horita, K. Yamaji, Y. P. Xiong, N. Sakai, and H. Yokokawa, "Attempt of utilizing liquid fuels with Ni–ScSZ anode in SOFCs," *Solid State Ionics*, 175, 107-111, 2004.
- [10] H. Kishimoto, K. Yamaji, T. Horita, Y. P. Xiong, N. Sakai, M. E. Brito, and H. Yokokawa, "Reaction process in the Ni-ScSZ anode for hydrocarbon fueled SOFCs," *Journal of the Electrochemical Society*, 153, A982-A988, 2006.
- [11] J. M. Vohs, and R. J. Gorte, "High-Performance SOFC Cathodes Prepared by Infiltration," *Advanced Materials*, 21, 943-956, 2009.
- [12] J. M. Serra, and H. P. Buchkremer, "On the nanostructuring and catalytic promotion of intermediate temperature solid oxide fuel cell (IT-SOFC) cathodes," *Journal of Power Sources*, 172, 768-774, 2007.
- [13] N. Q. Minh, and T. Takahashi, Science and Technology of Ceramic Fuel Cells. Amsterdam: Elsevier, 1995.
- [14] L. Blum, H. P. Buchkremer, S. Gross, A. Gubner, L. G. J. de Haart, H. Nabielek, W. J. Quadakkers, U. Reisgen, M. J. Smith, R. Steinberger-Wilckens, R. W. Steinbrech, F. Tietz, and I. C. Vinke, "Solid oxide fuel cell development at Forschungszentrum Juelich," *Fuel Cells*, 7, 204-210, 2007.
- [15] E. Fontell, T. Kivisaari, N. Christiansen, J. B. Hansen, and J. Palsson, "Conceptual study of a 250 kW planar SOFC system for CHP application," *Journal of Power Sources*, 131, 49-56, 2004.
- [16] W. R. Grove, Philos. Mag. (III), 417, 1842.
- [17] B. Y. S. Lin, D. W. Kirk, and S. J. Thorpe, "Performance of alkaline fuel cells: A possible future energy system?," *Journal of Power Sources*, 161, 474-483, 2006.
- [18] S. I. Smedley, A. Gardiner, I. Brown, B. Childs, and T. Froebel, "Materials issues in the development of a long life alkaline fuel cell electrode," *Materials at High Temperatures*, 24, 205-209, 2007.
- [19] R. K. A. M. Mallant, "PEMFC systems: the need for high temperature polymers as a consequence of PEMFC water and heat management," *Journal of Power Sources*, 118, 424-429, 2003.

- [20] T. E. Lipman, J. L. Edwards, and D. M. Kammen, "Fuel cell system economics: comparing the costs of generating power with stationary and motor vehicle PEM fuel cell systems," *Energy Policy*, 32, 101-125, 2004.
- [21] J. C. Yang, Y. S. Park, S. H. Seo, H. J. Lee, and J. S. Noh, "Development of a 50 kW PAFC power generation system," *Journal of Power Sources*, 106, 68-75, 2002.
- [22] B. C. H. Steele, "Material science and engineering: The enabling technology for the commercialisation of fuel cell systems," *Journal of Materials Science*, 36, 1053-1068, 2001.
- [23] J. M. Feret, "Westinghouse air-cooled PAFC technology," *Journal of Power Sources*, 29, 59-69, 1990.
- [24] A. J. Appleby, "Issues in fuel cell commercialization," *Journal of Power Sources*, 58, 153-176, 1996.
- [25] R. Bove, and P. Lunghi, "Experimental comparison of MCFC performance using three different biogas types and methane," *Journal of Power Sources*, 145, 588-593, 2005.
- [26] A. J. Appleby, "Fuel cell technology: Status and future prospects," *Energy*, 21, 521-653, 1996.
- [27] R. Rashidi, P. Berg, and I. Dincer, "Performance investigation of a combined MCFC system," *International Journal of Hydrogen Energy 2nd World Hydrogen Technologies Convention*, 34, 4395-4405, 2009.
- [28] V. V. Kharton, F. M. B. Marques, and A. Atkinson, "Transport properties of solid oxide electrolyte ceramics: a brief review," *Solid State Ionics*, 174, 135-149, 2004.
- [29] D. Hassan, S. Janes, and R. Clasen, "Proton-conducting ceramics as electrode/electrolyte materials for SOFC's - part 1: preparation, mechanical and thermal properties of sintered bodies," *Journal of the European Ceramic Society*, 23, 221-228, 2003.
- [30] S. C. Singhal, and K. Kendall, High-temperature Solid Oxide Fuel Cells: Fundamentals, Design and Applications. Oxford, UK: Elsevier, 2003.
- [31] S. P. S. Badwal, and K. Foger, "Solid oxide electrolyte fuel cell review," Ceramics International, 22, 257-265, 1996.
- [32] N. Q. Minh, and T. Takahashi, "Science and Technology of Ceramic Fuel Cells," 16, 1995
- [33] R. Chiba, T. Ishii, and F. Yoshimura, "Temperature dependence of ionic conductivity in (1-x)ZrO_{2-(x-y)}Sc₂O_{3-y}Yb₂O₃ electrolyte material," *Solid State Ionics*, 91, 249-256, 1996.
- [34] J.-H. Lee, and M. Yoshimura, "Phase stability and electrical conductivity of the Zr_{0.5}Y_{0.5}Q_{1.75}-Y_{0.75}Nb_{0.25}Q_{1.75} system," Solid State Ionics, 124, 185-191, 1999.
- [35] M. Mori, T. Abe, H. Itoh, O. Yamamoto, Y. Takeda, and T. Kawahara, "Cubic-stabilized zirconia and alumina composites as electrolytes in planar type solid oxide fuel cells," *Solid State Ionics*, 74, 157-164, 1994.
- [36] O. Yamamoto, Y. Arati, Y. Takeda, N. Imanishi, Y. Mizutani, M. Kawai, and Y. Nakamura, "Electrical conductivity of stabilized zirconia with ytterbia and scandia," Solid State Ionics, 79, 137-142, 1995.
- [37] T. H. Etsell, and S. N. Flengas, "Electrical properties of solid oxide electrolytes," *Chemical Reviews*, 70, 339-376, 1970.
- [38] V. V. Kharton, E. N. Naumovich, and A. A. Vecher, "Research on the electrochemistry of oxygen ion conductors in the former Soviet Union. I. ZrO2-based ceramic materials," *Journal of Solid State Electrochemistry*, 3, 61-81, 1999.
- [39] S. P. S. Badwal, "Zirconia-based solid electrolytes microstructure, stability and Ionic-conductivity," *Solid State Ionics*, 52, 23-32, 1992.
- [40] V. V. Kharton, F. M. Figueiredo, L. Navarro, E. N. Naumovich, A. V. Kovalevsky, A. A. Yaremchenko, A. P. Viskup, A. Carneiro, F. M. B. Marques, and J. R. Frade, "Ceria-based materials for solid oxide fuel cells," *Journal of Materials Science*, 36, 1105-1117, 2001.

- [41] H. Yahiro, K. Eguchi, and H. Arai, "Electrical properties and reducibilities of ceria-rare earth oxide systems and their application to solid oxide fuel cell," *Solid State Ionics*, 36, 71-75, 1989.
- [42] M. Mogensen, N. M. Sammes, and G. A. Tompsett, "Physical, chemical and electrochemical properties of pure and doped ceria," *Solid State Ionics*, 129, 63-94, 2000
- [43] B. C. H. Steele, "Appraisal of Ce_{1-y}Gd_yO_{2-y/2} electrolytes for IT-SOFC operation at 500 °C," *Solid State Ionics*, 129, 95-110, 2000.
- [44] M. Godickemeier, and L. J. Gauckler, "Engineering of solid oxide fuel cells with ceria-based electrolytes," *Journal of the Electrochemical Society*, 145, 414-421, 1998.
- [45] A. Atkinson, "Chemically-induced stresses in gadolinium-doped ceria solid oxide fuel cell electrolytes," *Solid State Ionics*, 95, 249-258, 1997.
- [46] V. V. Kharton, A. L. Shaula, N. P. Vyshatko, and F. M. B. Marques, "Electron-hole transport in (La_{0.9}Sr_{0.1})_{0.98}Ga_{0.8}Mg_{0.2}O_{3.δ} electrolyte: effects of ceramic microstructure," *Electrochimica Acta*, 48, 1817-1828, 2003.
- [47] T. Ishihara, H. Matsuda, and Y. Takita, "Doped LaGaO₃ perovskite-type oxide as a new oxide ionic conductor," *Journal of the American Chemical Society*, 116, 3801-3803, 1994
- [48] K. Q. Huang, R. S. Tichy, and J. B. Goodenough, "Superior perovskite oxide-ion conductor; strontium- and magnesium-doped LaGaO₃: I, phase relationships and electrical properties," *Journal of the American Ceramic Society*, 81, 2565-2575, 1998.
- [49] K. Q. Huang, M. Feng, J. B. Goodenough, and C. Milliken, "Electrode performance test on single ceramic fuel cells using as electrolyte Sr- and Mg-doped LaGaO₃," *Journal of the Electrochemical Society*, 144, 3620-3624, 1997.
- [50] T. Ishihara, J. Tabuchi, S. Ishikawa, J. Yan, M. Enoki, and H. Matsumoto, "Recent progress in LaGaO₃ based solid electrolyte for intermediate temperature SOFCs," *Solid State Ionics*, 177, 1949-1953, 2006.
- [51] K. Q. Huang, R. S. Tichy, and J. B. Goodenough, "Superior perovskite oxide-ion conductor; strontium- and magnesium-doped LaGaO₃: II, AC impedance spectroscopy," *Journal of the American Ceramic Society*, 81, 2576-2580, 1998.
- [52] J. W. Stevenson, T. R. Armstrong, L. R. Pederson, J. Li, C. A. Lewinsohn, and S. Baskaran, "Effect of A-site cation nonstoichiometry on the properties of doped lanthanum gallate," *Solid State Ionics*, 115, 571-583, 1998.
- [53] A. Ahmad-Khanlou, F. Tietz, and D. Stover, "Material properties of $La_{0.8}Sr_{0.2}Ga_{9+x}Mg_{0.1}O_{3-\delta}$ as a function of Ga content," *Solid State Ionics*, 135, 543-547, 2000.
- [54] K. D. Kreuer, "Proton-conducting oxides," Annual Review of Materials Research, 33, 333-359, 2003.
- [55] V. V. Kharton, F. M. B. Marques, and A. Atkinson, "Transport properties of solid oxide electrolyte ceramics: a brief review," *Solid State Ionics Dokiya Memorial Special Issue*, 174, 135-149, 2004.
- [56] N. M. Sammes, G. A. Tompsett, H. Näfe, and F. Aldinger, "Bismuth based oxide electrolytes-Structure and ionic conductivity," *Journal of the European Ceramic Society*, 19, 1801-1826, 1999.
- [57] N. Jiang, E. D. Wachsman, and S.-H. Jung, "A higher conductivity Bi₂O₃ based electrolyte," *Solid State Ionics*, 150, 347-353, 2002.
- [58] K. R. Kendall, J. K. Thomas, and H.-C. zur Loye, "Oxygen ion conductivity in a new class of layered bismuth oxides," *Solid State Ionics*, 70-71, 221-224, 1994.
- [59] C. E. Hatchwell, N. M. Sammes, and K. Kendall, "Cathode current-collectors for a novel tubular SOFC design," *Journal of Power Sources*, 70, 85-90, 1998.
- [60] V. V. Kharton, A. A. Yaremchenko, and E. N. Naumovich, "Research on the electrochemistry of oxygen ion conductors in the former Soviet Union. II. Perovskiterelated oxides," *Journal of Solid State Electrochemistry*, 3, 303-326, 1999.

- [61] O. Yamamoto, Y. Takeda, R. Kanno, and M. Noda, "Perovskite-Type Oxides as Oxygen Electrodes for High-Temperature Oxide Fuel-Cells," *Solid State Ionics*, 22, 241-246, 1987.
- [62] Y. Ohno, S. Nagata, and H. Sato, "Properties of oxides for high-temperature solid electrolyte fuel-cell," *Solid State Ionics*, 9-10, 1001-1007, 1983.
- [63] S. B. Adler, "Mechanism and kinetics of oxygen reduction on porous La_{1-x}Sr_xCoO_{3-δ} electrodes," *Solid State Ionics*, 111, 125-134, 1998.
- [64] H. Uchida, S. Arisaka, and M. Watanabe, "High performance electrode for medium-temperature solid oxide fuel cells La(Sr)CoO₃ cathode with ceria interlayer on zirconia electrolyte," *Electrochemical and Solid State Letters*, 2, 428-430, 1999.
- [65] T. Kawada, K. Masuda, J. Suzuki, A. Kaimai, K. Kawamura, Y. Nigara, J. Mizusaki, H. Yugami, H. Arashi, N. Sakai, and H. Yokokawa, "Oxygen isotope exchange with a dense La_{0.6}Sr_{0.4}CoO_{3-δ} electrode on a Ce_{0.9}Ca_{0.1}O_{1.9} electrolyte," *Solid State Ionics*, 121, 271-279, 1999.
- [66] V. V. Srdic, R. P. Omorjan, and J. Seydel, "Electrochemical performances of (La,Sr)CoO3 cathode for zirconia-based solid oxide fuel cells," *Materials Science and Engineering B-Solid State Materials for Advanced Technology*, 116, 119-124, 2005.
- [67] N. Q. Minh, "Ceramic Fuel-Cells," Journal of the American Ceramic Society, 76, 563-588, 1993.
- [68] J. Malzbender, E. Wessel, R. W. Steinbrech, and L. Singheiser, "Reduction and reoxidation of anodes for Solid Oxide Fuel Cells (SOFC)," presented at Ceram. Eng. & Sci. Proc, 2004.
- [69] D. Stöver, H.-P. Buchkremer, and J. P. P. Huijsmans, "Handbook of Fuel Cells: Fundamentals, Technology and Applications," vol. 4, W. Vielstich, A. Lamm, and H. A. Gasteiger (Eds.), Eds., Auflage. Chichester, U.K.: John Wiley & Sons, 2003, 1015-1031.
- [70] S. C. Singhal, presented at Proc. 4th Int. Symp. Solid Oxide Fuel Cells (SOFC IV), Pennington, NJ, PV95-1, 1995.
- [71] R. A. George, "Status of tubular SOFC field unit demonstrations," *Journal of Power Sources*, 86, 134-139, 2000.
- [72] T. Yamaguchi, S. Shimizu, T. Suzuki, Y. Fujishiro, and M. Awano, "Fabrication and characterization of high performance cathode supported small-scale SOFC for intermediate temperature operation," *Electrochemistry Communications*, 10, 1381-1383, 2008.
- [73] S. C. Singhal, "Science and technology of solid-oxide fuel cells," MRS Bulletin, 25, 16-21, 2000
- [74] K. Mehta, R. Xu, and A. V. Virkar, "Two-layer fuel cell electrolyte structure by sol-gel processing," *Journal of Sol-Gel Science and Technology*, 11, 203-207, 1998.
- [75] P. Lenormand, M. Rieu, R. F. Cienfuegos, A. Julbe, S. Castillo, and F. Ansart, "Potentialities of the sol-gel route to develop cathode and electrolyte thick layers Application to SOFC systems," *Surface & Coatings Technology*, 203, 901-904, 2008.
- [76] M. L. Fontaine, C. Laberty-Robert, F. Ansart, and P. Tailhades, "Composition and porosity graded $La_{2-x}NiO_{4+\delta}$ ($x \ge 0$) interlayers for SOFC: Control of the microstructure via a sol-gel process," *Journal of Power Sources*, 156, 33-38, 2006.
- [77] P. G. Keech, D. E. Trifan, and V. I. Birss, "Synthesis and performance of sol-gel prepared Ni-YSZ cermet SOFC anodes," *Journal of the Electrochemical Society*, 152, A645-A651, 2005.
- [78] P. Egger, G. D. Soraru, and S. Dire, "Sol-gel synthesis of polymer-YSZ hybrid materials for SOFC technology," *Journal of the European Ceramic Society*, 24, 1371-1374, 2004.
- [79] W. S. Jang, S. H. Hyun, and S. G. Kim, "Preparation of YSZ/YDC and YSZ/GDC composite electrolytes by the tape casting and sol-gel dip-drawing coating method for low-temperature SOFC," *Journal of Materials Science*, 37, 2535-2541, 2002.
- [80] R. Chiba, F. Yoshimura, and J. Yamaki, "A composite electrolyte for an SOFC consisting of a ceria sheet and a zirconia film deposited by the sol-gel method,"

- Materials for Electrochemical Energy Storage and Conversion Ii-Batteries, Capacitors and Fuel Cells, 496, 185-191, 1998.
- [81] B. G. Prevo, D. M. Kuncicky, and O. D. Velev, "Engineered deposition of coatings from nano- and micro-particles: A brief review of convective assembly at high volume fraction," *Colloids and Surfaces a-Physicochemical and Engineering Aspects*, 311, 2-10, 2007.
- [82] C. J. Brinker, and G. W. Scherer, Sol-gel science: the physics and chemistry of sol-gel processing. London: Academic Press Limited, 1990.
- [83] C. Guizard, "Sol-Gel chemistry and its application to porous membrane processing," in Fundamentals of inorganic membrane science and technology, A. J. Burggraaf and L. Cot, Eds., Auflage. Amsterdam: Elsevier, 1996, 227-258.
- [84] B. Derjaguin, and L. Landau, "Theory of the stability of strongly charged lyophobic sols and of the adhesion of strongly charged particles in solutions of electrolytes," *Acta Physico chemica URSS*, 14, 633, 1941.
- [85] E. J. W. Verwey, and J. T. G. Overbeek, Theory of the stability of lyophobic colloids. Amsterdam: Elsevier, 1948.
- [86] L. Cot, A. Ayral, J. Durand, C. Guizard, N. Hovnanian, A. Julbe, and A. Larbot, "Inorganic membranes and solid state sciences," *Solid State Sciences*, 2, 313-334, 2000.
- [87] C. Sanchez, J. Livage, M. Henry, and F. Babonneau, "Chemical Modification of Alkoxide Precursors," *Journal of Non-Crystalline Solids*, 100, 65-76, 1988.
- [88] D. E. Bornside, C. W. Macosko, and L. E. Scriven, "On the modeling of spin coating," *Journal of Imaging Technology*, 13, 122-130, 1987.
- [89] L. E. Scriven, Better Ceramics Through Chemistry III. Pittsburg: Mat. Res. Soc., 1988.
- [90] J. A. Aksay, and C. H. Shilling, "Colloidal Filtration Route to Uniform Microstructure," in *Ultrastructure processing of ceramics, glasses, and composites*, L. L. Hench and D. R. Ulrich, Eds., Auflage. New York: John Wiley & Sons, 1984, 439-448
- [91] H. Dislich, and E. Hussmann, "Amorphous and crystalline dip coatings obtained from organometallic solutions - procedures, chemical processes and products," *Thin Solid Films*, 77, 129-139, 1981.
- [92] G. W. Scherer, "Drying gels VII. diffusion during drying," *Journal of Non-Crystalline Solids*, 107, 135-148, 1989.
- [93] G. W. Scherer, "Drying gels I. general-theory," Journal of Non-Crystalline Solids, 87, 199-225, 1986.
- [94] G. W. Scherer, "Recent progress in drying of gels," *Journal of Non-Crystalline Solids*, 147, 363-374, 1992.
- [95] G. W. Scherer, "Stress and fracture during drying of gels," *Journal of Non-Crystalline Solids*, 121, 104-109, 1990.
- [96] L. Landau, and B. Levich, "Dragging of a liquid by a moving plate," Acta Physicochimica Urss, 17, 42-54, 1942.
- [97] C. J. Brinker, A. J. Hurd, P. R. Schunk, G. C. Frye, and C. S. Ashley, "Review of sol-gel thin-film formation," *Journal of Non-Crystalline Solids*, 147, 424-436, 1992.
- [98] S. F. Kistler, and P. M. Schweizer, *Liquid Film Coating*. London: Chapman. & Hal, 1997.
- [99] C. J. Brinker, and S. P. Mukherjee, "Comparisons of sol-gel-derived thin-films with monoliths in a multicomponent silicate glass system," *Thin Solid Films*, 77, 141-148, 1981.
- [100] D. Simwonis, A. Naoumidis, F. J. Dias, J. Linke, and A. Moropoulou, "Material characterization in support of the development of an anode substrate for solid oxide fuel cells," *Journal of Materials Research*, 12, 1508-1518, 1997.
- [101] F. C. M. Woudenberg, "Nanostructred oxide coatings via emulsion precipitaton." Enshede: University of Twente, 2001, 9-10.
- [102] D. Stöver, H. P. Buchkremer, and J. P. P. Huijsmans, Handbook of Fuel Cells, 4. Chichester: John Wiley and Sons Inc., 2003.

- [103] R. Mücke, "Sinterung von zirkoniumdioxid-elektrolyten im mehrlagenverbund der oxidkeramischen brennstoffzelle (SOFC)," in *Institute for Energy Research (IEF-1)*. Jülich: Forschungszentrum Juelich, 2007, 32.
- [104] P. Kontouros, R. Fo"rthmann, A. Naoumidis, G. Stochniol, and E. Syskakis, "Synthesis, forming and characterization of ceramic materials for the planar solid oxide fuel cell (SOFC)," *Ionics*, 1, 40–50, 1995.
- [105] R. Mucke, N. H. Menzler, H. P. Buchkremer, and D. Stover, "Cofiring of Thin Zirconia Films During SOFC Manufacturing," *Journal of the American Ceramic Society*, 92, S95-S102, 2009.
- [106] R. Jenkins, and R. Snyder, "Introduction to X-ray Powder Diffractometry," *Chemical Analysis*, 138, 90, 1996.
- [107] D. Stöver, H. P. Buchkremer, F. Tietz, and N. H. Menzler, "Proceedings of the 5th European Solid Oxide Fuel Cell Forum," presented at European Fuel Cell Forum 2002, Lucerne, Switzerland, 2002.
- [108] A. Leonide, V. Sonn, A. Weber, and E. Ivers-Tiffee, "Evaluation and modeling of the cell resistance in anode-supported solid oxide fuel cells," *Journal of the Electrochemical Society*, 155, B36-B41, 2008.
- [109] V. A. C. Haanappel, and M. J. Smith, "A review of standardising SOFC measurement and quality assurance at FZJ," *Journal of Power Sources*, 171, 169-178, 2007.
- [110] V. A. C. Haanappel, A. Mai, and J. Mertens, "Electrode activation of anode-supported SOFCs with LSM- or LSCF-type cathodes," *Solid State Ionics*, 177, 2033-2037, 2006.
- [111] V. A. C. Haanappel, J. Mertens, and A. Mai, "Performance improvement of (La, Sr)MnO₃ and (La, Sr)_x (Co, Fe)O₃-type anode-supported SOFCs," *Journal of Fuel Cell Science and Technology*, 3, 263-270, 2006.
- [112] T. A. Peters, C. H. S. Poeth, N. E. Benes, H. C. W. M. Buijs, F. F. Vercauteren, and J. T. F. Keurentjes, "Ceramic-supported thin PVA pervaporation membranes combining high flux and high selectivity; contradicting the flux-selectivity paradigm," *Journal of Membrane Science*, 276, 42-50, 2006.
- [113] G. Carcano, M. Ceriani, and F. Soglio, "Spin coating with high viscosity photoresist on square substrates," *Hybrid Circuits*, 32, 12, 1993.
- [114] X. Guo, and R. Waser, "Electrical properties of the grain boundaries of oxygen ion conductors: Acceptor-doped zirconia and ceria," *Progress in Materials Science*, 51, 151-210, 2006.
- [115] X. Guo, and Z. L. Zhang, "Grain size dependent grain boundary defect structure: case of doped zirconia," *Acta Materialia*, 51, 2539-2547, 2003.
- [116] X. Guo, J. Fleig, and J. Maier, "Separation of electronic and ionic contributions to the gain boundary conductivity in acceptor-doped SrTiO₃," *Journal of the Electrochemical Society*, 148, J50-J53, 2001.
- [117] M. J. Verkerk, B. J. Middelhuis, and A. J. Burggraaf, "Effect of Grain-Boundaries on the Conductivity of High-Purity ZrO₂-Y₂O₃ Ceramics," *Solid State Ionics*, 6, 159-170, 1982.
- [118] J. E. Bauerle, "Study of Solid Electrolyte Polarization by a Complex Admittance Method," *Journal of Physics and Chemistry of Solids*, 30, 2657-&, 1969.
- [119] S. B. Adler, J. A. Lane, and B. C. H. Steele, "Electrode kinetics of porous mixed-conducting oxygen electrodes," *Journal of the Electrochemical Society*, 143, 3554-3564, 1996.
- [120] P. Hjalmarsson, M. Sogaard, and M. Mogensen, "Electrochemical performance and degradation of (La_{0.6}Sr_{0.4})_{0.99}CoO_{3-δ} as porous SOFC-cathode," *Solid State Ionics*, 179, 1422-1426, 2008.

7 Acknowledgements

I would like to express my deep appreciation to Professor Dr. Deltev Stöver for being my "Doktorvater", to Prof. Dr. Lorenz Singheiser for his work in evaluating the dissertation and being my co-referee, as well as to Prof. Dr. Marcus Petermann for the chairmanship during the examination.

I am most grateful to Dr. Hans Peter Buchkremer for his kindness, persistent motivation and endless support on me. I also appreciate my co-supervisors, Dr. Robert Mücke, Dr. Tim Van Gestel, and Dr. Norbert Menzler for their excellent supervisions, guidance, expertise, generosity with knowledge and interactive discussions in the process for accomplishing of my PhD work.

I would like to thank the German Academic Exchange Service (DAAD), the Helmholtz Association of National Research Centers (HFG), and Institute of Energy Research (IEF-1) in Forschungszentrum Jülich (FZJ) for funding and supporting my work. Especially, I thank Ms. Irmgard Kasperek from DAAD and Ms. Roswitha Bley for their excellent coordination work for my stay in Germany.

Many thanks to Dr. Werner Fischer, Dr. Doris Sebold, Dr. Vincent Haanappel, Mr. Volker Bader, Mr. Werner Herzhof, Ms. Kiki Portulidou, Mr. Frank Vondahlen, Ms. Hiltrud Moitroux, Mr. Mark Kappertz, Mr. Marian Kampel, Mr. Gert Mattonette, Mr. Fried Oellers, Mr. Tobias Offermanns, Mr. Stefan Giesen, Ms. Sigrid Schwartz-Lückge, Ms. Andrea Hilgers and Mr. Josef Mertens, whose efficient work ensured my work to be carried out.

I thank Mr. André Leonide from Institute of Materials for Electrical and Electronic Engineering (IWE) of Karlsruhe Institute of Technology (KIT), for the EIS measurement and data processing, Dr. Stefan Roitsch from Ernst Ruska Center for TEM characterization.

I thank Dr. André Weber from Institute of Materials for Electrical and Electronic Engineering (IWE) of Karlsruhe Institute of Technology (KIT), Dr. L.G.J. de Haart from Institute of Energy Research (IEF-3), Dr. Guo Xin from Institute of Solid State Research (IFF), Dr. Stefan Baumann, Dr. Qingxi Fu, Dr. Ophelia Jarligo, Dr. Qianli Ma, Dr. Frank Tietz and Dr. Sven Uhlenbruck for the helpful and instructive discussions.

I am grateful to Ms. Marlene Pionke, Ms. Marianne Meyer, Ms. Vicky Rostin, Ms. Hannelore Rüther, Ms. Brigit Stäbler and Mr. Stefan Weitz for the organization and administrative support.

Furthermore, I would like take this opportunity to express thanks to my friends: Rafael Berhane, Michael Betz, Katarina Brands, Dr. Luru Dai, Dr. Manuel Ettler, Dr. Oskar Hassan, Felix Hauler, Kamran Karim, Yang Lei, Dr. Manuel Köhl, Falk Schülze-Küppers, Meng Li, Hyo-Joeng Moon, Dr. Wolfgang Schafbauer, Dr. Keke Tian, Ye Xing,

Most important, I would like to convey my appreciation and love to my family, especially to my father, my grandmother and my wife, for their year-long support and sacrifice. This dissertation is dedicated to them.

Curriculum Vitae

Personal details:

Name: Feng HAN

Date of Birth: Nov. 26th, 1979 Place of Birth: Jinan, China

Marital Status: Married Nationality: Chinese

Education:

09/2006-05/2010: Ph.D candidate

Institute of Energy Research (IEF-1), Forschungszentrum Jülich GmbH

Department of Mechanical Engineering, Ruhr-University Bochum

Doctoral dissertation: Sol-gel and nano-suspension electrolyte layers for high

performance solid oxide fuel cells

07/2003-06/2006: Master of Engineer

National Laboratory of Crystal Materials, Shandong University

Master thesis: Hydrothermal synthesis of several low-dimensional thermoelectric

materials: LiFeP, PbTe and PbSe

07/1999-06/2003: Bachelor of Engineer

Department of Material Science and Engineering, Shandong University Bachelor thesis: *Microwave assisted synthesis of YAG ceramic powder*

Occupational Experience:

02/2010-06/2011: Research Fellow

Institute of Energy Research (IEF-1), Forschungszentrum Jülich GmbH

07/2003-06/2006: Research Assistant

National Laboratory of Crystal Materials, Shandong University

 Einsatz von multispektralen Satellitenbilddaten in der Wasserhaushaltsund Stoffstrommodellierung – dargestellt am Beispiel des Rureinzugsgebietes

von C. Montzka (2008), XX, 238 Seiten

ISBN: 978-3-89336-508-1

2. Ozone Production in the Atmosphere Simulation Chamber SAPHIR

by C. A. Richter (2008), XIV, 147 pages

ISBN: 978-3-89336-513-5

3. Entwicklung neuer Schutz- und Kontaktierungsschichten für Hochtemperatur-Brennstoffzellen

von T. Kiefer (2008), 138 Seiten

ISBN: 978-3-89336-514-2

4. Optimierung der Reflektivität keramischer Wärmedämmschichten aus Yttrium-teilstabilisiertem Zirkoniumdioxid für den Einsatz auf metallischen Komponenten in Gasturbinen

von A. Stuke (2008), X, 201 Seiten

ISBN: 978-3-89336-515-9

5. Lichtstreuende Oberflächen, Schichten und Schichtsysteme zur Verbesserung der Lichteinkopplung in Silizium-Dünnschichtsolarzellen

von M. Berginski (2008), XV, 171 Seiten

ISBN: 978-3-89336-516-6

6. Politikszenarien für den Klimaschutz IV – Szenarien bis 2030

hrsg.von P. Markewitz, F. Chr. Matthes (2008), 376 Seiten

ISBN 978-3-89336-518-0

7. Untersuchungen zum Verschmutzungsverhalten rheinischer Braunkohlen in Kohledampferzeugern

von A. Schlüter (2008), 164 Seiten

ISBN 978-3-89336-524-1

8. Inorganic Microporous Membranes for Gas Separation in Fossil Fuel Power Plants

by G. van der Donk (2008), VI, 120 pages

ISBN: 978-3-89336-525-8

 Sinterung von Zirkoniumdioxid-Elektrolyten im Mehrlagenverbund der oxidkeramischen Brennstoffzelle (SOFC)

von R. Mücke (2008), VI, 165 Seiten

ISBN: 978-3-89336-529-6

10. Safety Considerations on Liquid Hydrogen

by K. Verfondern (2008), VIII, 167 pages

ISBN: 978-3-89336-530-2

11. Kerosinreformierung für Luftfahrtanwendungen

von R. C. Samsun (2008), VII, 218 Seiten

ISBN: 978-3-89336-531-9

12. Der 4. Deutsche Wasserstoff Congress 2008 – Tagungsband

hrsg. von D. Stolten, B. Emonts, Th. Grube (2008), 269 Seiten

ISBN: 978-3-89336-533-3

13. Organic matter in Late Devonian sediments as an indicator for environmental changes

by M. Kloppisch (2008), XII, 188 pages

ISBN: 978-3-89336-534-0

14. Entschwefelung von Mitteldestillaten für die Anwendung in mobilen Brennstoffzellen-Systemen

von J. Latz (2008), XII, 215 Seiten

ISBN: 978-3-89336-535-7

15. **RED-IMPACT**

Impact of Partitioning, Transmutation and Waste Reduction Technologies on the Final Nuclear Waste Disposal

SYNTHESIS REPORT

ed. by W. von Lensa, R. Nabbi, M. Rossbach (2008), 178 pages

ISBN 978-3-89336-538-8

16. Ferritic Steel Interconnectors and their Interactions with Ni Base Anodes in Solid Oxide Fuel Cells (SOFC)

by J. H. Froitzheim (2008), 169 pages

ISBN: 978-3-89336-540-1

17. Integrated Modelling of Nutrients in Selected River Basins of Turkey

Results of a bilateral German-Turkish Research Project project coord. M. Karpuzcu, F. Wendland (2008), XVI, 183 pages

ISBN: 978-3-89336-541-8

18. Isotopengeochemische Studien zur klimatischen Ausprägung der Jüngeren Dryas in terrestrischen Archiven Eurasiens

von J. Parplies (2008), XI, 155 Seiten, Anh.

ISBN: 978-3-89336-542-5

19. Untersuchungen zur Klimavariabilität auf dem Tibetischen Plateau -Ein Beitrag auf der Basis stabiler Kohlenstoff- und Sauerstoffisotope in Jahrringen von Bäumen waldgrenznaher Standorte

von J. Griessinger (2008), XIII, 172 Seiten

ISBN: 978-3-89336-544-9

20. Neutron-Irradiation + Helium Hardening & Embrittlement Modeling of 9%Cr-Steels in an Engineering Perspective (HELENA)

by R. Chaouadi (2008), VIII, 139 pages

ISBN: 978-3-89336-545-6

21. in Bearbeitung

22. Verbundvorhaben APAWAGS (AOEV und Wassergenerierung) – Teilprojekt: Brennstoffreformierung – Schlussbericht

von R. Peters, R. C. Samsun, J. Pasel, Z. Porš, D. Stolten (2008), VI, 106 Seiton

ISBN: 978-3-89336-547-0

23. FREEVAL

Evaluation of a Fire Radiative Power Product derived from Meteosat 8/9 and Identification of Operational User Needs

Final Report

project coord. M. Schultz, M. Wooster (2008), 139 pages

ISBN: 978-3-89336-549-4

24. Untersuchungen zum Alkaliverhalten unter Oxycoal-Bedingungen

von C. Weber (2008), VII, 143, XII Seiten ISBN: 978-3-89336-551-7

25. Grundlegende Untersuchungen zur Freisetzung von Spurstoffen, Heißgaschemie, Korrosionsbeständigkeit keramischer Werkstoffe und Alkalirückhaltung in der Druckkohlenstaubfeuerung

von M. Müller (2008), 207 Seiten

ISBN: 978-3-89336-552-4

26. Analytik von ozoninduzierten phenolischen Sekundärmetaboliten in Nicotiana tabacum L. cv Bel W3 mittels LC-MS

von I. Koch (2008), III, V, 153 Seiten ISBN 978-3-89336-553-1

27. IEF-3 Report 2009. Grundlagenforschung für die Anwendung

(2009), ca. 230 Seiten ISBN: 978-3-89336-554-8

28. Influence of Composition and Processing in the Oxidation Behavior of MCrAlY-Coatings for TBC Applications

by J. Toscano (2009), 168 pages

ISBN: 978-3-89336-556-2

29. Modellgestützte Analyse signifikanter Phosphorbelastungen in hessischen Oberflächengewässern aus diffusen und punktuellen Quellen

von B. Tetzlaff (2009), 149 Seiten

ISBN: 978-3-89336-557-9

30. Nickelreaktivlot / Oxidkeramik – Fügungen als elektrisch isolierende Dichtungskonzepte für Hochtemperatur-Brennstoffzellen-Stacks

von S. Zügner (2009), 136 Seiten

ISBN: 978-3-89336-558-6

31. Langzeitbeobachtung der Dosisbelastung der Bevölkerung in radioaktiv kontaminierten Gebieten Weißrusslands – Korma-Studie

von H. Dederichs, J. Pillath, B. Heuel-Fabianek, P. Hill, R. Lennartz (2009),

Getr. Pag.

ISBN: 978-3-89336-532-3

32. Herstellung von Hochtemperatur-Brennstoffzellen über physikalische Gasphasenabscheidung

von N. Jordán Escalona (2009), 148 Seiten

ISBN: 978-3-89336-532-3

33. Real-time Digital Control of Plasma Position and Shape on the TEXTOR Tokamak

by M. Mitri (2009), IV, 128 pages

ISBN: 978-3-89336-567-8

34. Freisetzung und Einbindung von Alkalimetallverbindungen in kohlebefeuerten Kombikraftwerken

von M. Müller (2009), 155 Seiten

ISBN: 978-3-89336-568-5

35. Kosten von Brennstoffzellensystemen auf Massenbasis in Abhängigkeit von der Absatzmenge

von J. Werhahn (2009), 242 Seiten

ISBN: 978-3-89336-569-2

36. Einfluss von Reoxidationszyklen auf die Betriebsfestigkeit von anodengestützten Festoxid-Brennstoffzellen

von M. Ettler (2009), 138 Seiten

ISBN: 978-3-89336-570-8

37. Großflächige Plasmaabscheidung von mikrokristallinem Silizium für mikromorphe Dünnschichtsolarmodule

von T. Kilper (2009), XVII, 154 Seiten

ISBN: 978-3-89336-572-2

38. Generalized detailed balance theory of solar cells

by T. Kirchartz (2009), IV, 198 pages

ISBN: 978-3-89336-573-9

39. The Influence of the Dynamic Ergodic Divertor on the Radial Electric Field at the Tokamak TEXTOR

von J. W. Coenen (2009), xii, 122, XXVI pages

ISBN: 978-3-89336-574-6

40. Sicherheitstechnik im Wandel Nuklearer Systeme

von K. Nünighoff (2009), viii, 215 Seiten

ISBN: 978-3-89336-578-4

41. Pulvermetallurgie hochporöser NiTi-Legierungen für Implanat- und Dämpfungsanwendungen

von M. Köhl (2009), XVII, 199 Seiten

ISBN: 978-3-89336-580-7

42. Einfluss der Bondcoatzusammensetzung und Herstellungsparameter auf die Lebensdauer von Wärmedämmschichten bei zyklischer Temperaturbelastung

von M. Subanovic (2009), 188, VI Seiten

ISBN: 978-3-89336-582-1

43. Oxygen Permeation and Thermo-Chemical Stability of Oxygen Permeation Membrane Materials for the Oxyfuel Process

by A. J. Ellett (2009), 176 pages ISBN: 978-3-89336-581-4

44. Korrosion von polykristallinem Aluminiumoxid (PCA) durch Metalljodidschmelzen sowie deren Benetzungseigenschaften

von S. C. Fischer (2009), 148 Seiten

ISBN: 978-3-89336-584-5

45. IEF-3 Report 2009. Basic Research for Applications

(2009), 217 Seiten

ISBN: 978-3-89336-585-2

46. Verbundvorhaben ELBASYS (Elektrische Basissysteme in einem CFK-Rumpf) - Teilprojekt: Brennstoffzellenabgase zur Tankinertisierung -Schlussbericht

von R. Peters, J. Latz, J. Pasel, R. C. Samsun, D. Stolten

(2009), xi, 202 Seiten ISBN: 978-3-89336-587-6

47. Aging of ¹⁴C-labeled Atrazine Residues in Soil: Location, Characterization and Biological Accessibility

by N. D. Jablonowski (2009), IX, 104 pages

ISBN: 978-3-89336-588-3

48. Entwicklung eines energetischen Sanierungsmodells für den europäischen Wohngebäudesektor unter dem Aspekt der Erstellung von Szenarien für Energie- und CO₂ - Einsparpotenziale bis 2030

von P. Hansen (2009), XXII, 281 Seiten

ISBN: 978-3-89336-590-6

49. Reduktion der Chromfreisetzung aus metallischen Interkonnektoren für Hochtemperaturbrennstofzellen durch Schutzschichtsysteme

von R. Trebbels (2009), iii, 135 Seiten

ISBN: 978-3-89336-591-3

50. Bruchmechanische Untersuchung von Metall / Keramik-Verbundsystemen für die Anwendung in der Hochtemperaturbrennstoffzelle

von B. Kuhn (2009), 118 Seiten

ISBN: 978-3-89336-592-0

51. Wasserstoff-Emissionen und ihre Auswirkungen auf den arktischen Ozonverlust

Risikoanalyse einer globalen Wasserstoffwirtschaft

von T. Feck (2009), 180 Seiten ISBN: 978-3-89336-593-7

Development of a new Online Method for Compound Specific Measurements of Organic Aerosols

by T. Hohaus (2009), 156 pages

ISBN: 978-3-89336-596-8

53. Entwicklung einer FPGA basierten Ansteuerungselektronik für Justageeinheiten im Michelson Interferometer

von H. Nöldgen (2009), 121 Seiten

ISBN: 978-3-89336-599-9

54. Observation – and model – based study of the extratropical UT/LS

by A. Kunz (2010), xii, 120, xii pages

ISBN: 978-3-89336-603-3

55. Herstellung polykristalliner Szintillatoren für die Positronen-Emissions-Tomographie (PET)

von S. K. Karim (2010), VIII, 154 Seiten

ISBN: 978-3-89336-610-1

56. Kombination eines Gebäudekondensators mit H2-Rekombinatorelementen in Leichwasserreaktoren

von S. Kelm (2010), vii, 119 Seiten

ISBN: 978-3-89336-611-8

57. Plant Leaf Motion Estimation Using A 5D Affine Optical Flow Model

by T. Schuchert (2010), X, 143 pages

ISBN: 978-3-89336-613-2

58. Tracer-tracer relations as a tool for research on polar ozone loss

by R. Müller (2010), 116 pages

ISBN: 978-3-89336-614-9

59. Sorption of polycyclic aromatic hydrocarbon (PAH) to Yangtze River sediments and their components

by J. Zhang (2010), X, 109 pages

ISBN: 978-3-89336-616-3

60. Weltweite Innovationen bei der Entwicklung von CCS-Technologien und Möglichkeiten der Nutzung und des Recyclings von CO₂

Studie im Auftrag des BMWi

von W. Kuckshinrichs et al. (2010), X, 139 Seiten

ISBN: 978-3-89336-617-0

61. Herstellung und Charakterisierung von sauerstoffionenleitenden Dünnschichtmembranstrukturen

von M. Betz (2010). XII. 112 Seiten

ISBN: 978-3-89336-618-7

62. Politikszenarien für den Klimaschutz V – auf dem Weg zum Strukturwandel, Treibhausgas-Emissionsszenarien bis zum Jahr 2030

hrsg. von P. Hansen, F. Chr. Matthes (2010), 276 Seiten

ISBN: 978-3-89336-619-4

63. Charakterisierung Biogener Sekundärer Organischer Aerosole mit Statistischen Methoden

von C. Spindler (2010), iv, 163 Seiten

ISBN: 978-3-89336-622-4

64. Stabile Algorithmen für die Magnetotomographie an Brennstoffzellen

von M. Wannert (2010), ix, 119 Seiten

ISBN: 978-3-89336-623-1

65. Sauerstofftransport und Degradationsverhalten von Hochtemperaturmembranen für CO2-freie Kraftwerke

von D. Schlehuber (2010), VII, 139 Seiten

ISBN: 978-3-89336-630-9

66. Entwicklung und Herstellung von foliengegossenen, anodengestützten Festoxidbrennstoffzellen

von W. Schafbauer (2010), VI, 164 Seiten

ISBN: 978-3-89336-631-6

67. Disposal strategy of proton irradiated mercury from high power spallation sources

by S. Chiriki (2010), xiv, 124 pages

ISBN: 978-3-89336-632-3

68. Oxides with polyatomic anions considered as new electrolyte materials for solid oxide fuel cells (SOFCs)

by O. H. Bin Hassan (2010), vii, 121 pages

ISBN: 978-3-89336-633-0

69. Von der Komponente zum Stack: Entwicklung und Auslegung von HT-PEFC-Stacks der 5 kW-Klasse

von A. Bendzulla (2010), IX, 203 Seiten

ISBN: 978-3-89336-634-7

70. Satellitengestützte Schwerewellenmessungen in der Atmosphäre und Perspektiven einer zukünftigen ESA Mission (PREMIER)

von S. Höfer (2010), 81 Seiten ISBN: 978-3-89336-637-8

71. Untersuchungen der Verhältnisse stabiler Kohlenstoffisotope in atmosphärisch relevanten VOC in Simulations- und Feldexperimenten

von H. Spahn (2010), IV, 210 Seiten

ISBN: 978-3-89336-638-5

72. Entwicklung und Charakterisierung eines metallischen Substrats für nanostrukturierte keramische Gastrennmembranen

von K. Brands (2010), vii, 137 Seiten

ISBN: 978-3-89336-640-8

73. Hybridisierung und Regelung eines mobilen Direktmethanol-Brennstoffzellen-Systems

von J. Chr. Wilhelm (2010), 220 Seiten

ISBN: 978-3-89336-642-2

74. Charakterisierung perowskitischer Hochtemperaturmembranen zur Sauerstoffbereitstellung für fossil gefeuerte Kraftwerksprozesse

von S.A. Möbius (2010) III, 208 Seiten

ISBN: 978-3-89336-643-9

75. Characterization of natural porous media by NMR and MRI techniques: High and low magnetic field studies for estimation of hydraulic properties

by L.-R. Stingaciu (2010), 96 pages

ISBN: 978-3-89336-645-3

76. Hydrological Characterization of a Forest Soil Using Electrical Resistivity Tomography

by Chr. Oberdörster (2010), XXI, 151 pages

ISBN: 978-3-89336-647-7

77. Ableitung von atomarem Sauerstoff und Wasserstoff aus Satellitendaten und deren Abhängigkeit vom solaren Zyklus

von C. Lehmann (2010), 127 Seiten

ISBN: 978-3-89336-649-1

78. **18th World Hydrogen Energy Conference 2010 – WHEC2010 Proceedings**

Speeches and Plenary Talks

ed. by D. Stolten, B. Emonts (2010)

ISBN: 978-3-89336-658-3

78-1. 18th World Hydrogen Energy Conference 2010 – WHEC2010 Proceedings

Parallel Sessions Book 1:

Fuel Cell Basics / Fuel Infrastructures

ed. by D. Stolten, T. Grube (2010), ca. 460 pages

ISBN: 978-3-89336-651-4

78-2. 18th World Hydrogen Energy Conference 2010 – WHEC2010 Proceedings

Parallel Sessions Book 2:

Hydrogen Production Technologies - Part 1

ed. by D. Stolten, T. Grube (2010), ca. 400 pages

ISBN: 978-3-89336-652-1

78-3. 18th World Hydrogen Energy Conference 2010 – WHEC2010 Proceedings

Parallel Sessions Book 3:

Hydrogen Production Technologies - Part 2

ed. by D. Stolten, T. Grube (2010), ca. 640 pages

ISBN: 978-3-89336-653-8

78-4. 18th World Hydrogen Energy Conference 2010 – WHEC2010 Proceedings

Parallel Sessions Book 4:

Storage Systems / Policy Perspectives, Initiatives and Cooperations

ed. by D. Stolten, T. Grube (2010), ca. 500 pages

ISBN: 978-3-89336-654-5

78-5. 18th World Hydrogen Energy Conference 2010 – WHEC2010 Proceedings

Parallel Sessions Book 5:

Stategic Analysis / Safety Issues / Existing and Emerging Markets

ed. by D. Stolten, T. Grube (2010), ca. 530 pages

ISBN: 978-3-89336-655-2

78-6. 18th World Hydrogen Energy Conference 2010 – WHEC2010 Proceedings

Parallel Sessions Book 6:

Stationary Applications / Transportation Applications

ed. by D. Stolten, T. Grube (2010), ca. 330 pages

ISBN: 978-3-89336-656-9

78 Set (complete book series)

18th World Hydrogen Energy Conference 2010 – WHEC2010 Proceedings

ed. by D. Stolten, T. Grube, B. Emonts (2010)

ISBN: 978-3-89336-657-6

79. Ultrafast voltex core dynamics investigated by finite-element micromagnetic simulations

by S. Gliga (2010), vi, 144 pages

ISBN: 978-3-89336-660-6

80. Herstellung und Charakterisierung von keramik- und metallgestützten Membranschichten für die CO₂-Abtrennung in fossilen Kraftwerken

von F. Hauler (2010), XVIII, 178 Seiten

ISBN: 978-3-89336-662-0

81. Experiments and numerical studies on transport of sulfadiazine in soil columns

by M. Unold (2010), xvi, 115 pages

ISBN: 978-3-89336-663-7

82. Prompt-Gamma-Neutronen-Aktivierungs-Analyse zur zerstörungsfreien Charakterisierung radioaktiver Abfälle

von J.P.H. Kettler (2010), iv. 205 Seiten

ISBN: 978-3-89336-665-1

83. Transportparameter dünner geträgerter Kathodenschichten der oxidkeramischen Brennstoffzelle

von C. Wedershoven (2010), vi, 137 Seiten

ISBN: 978-3-89336-666-8

84. Charakterisierung der Quellverteilung von Feinstaub und Stickoxiden in ländlichem und städtischem Gebiet

von S. Urban (2010), vi, 211 Seiten

ISBN: 978-3-89336-669-9

85. Optics of Nanostructured Thin-Film Silicon Solar Cells

by C. Haase (2010), 150 pages

ISBN: 978-3-89336-671-2

86. Entwicklung einer Isolationsschicht für einen Leichtbau-SOFC-Stack

von R. Berhane (2010), X, 162 Seiten

ISBN: 978-3-89336-672-9

87. Hydrogen recycling and transport in the helical divertor of TEXTOR

by M. Clever (2010), x, 172 pages

ISBN: 978-3-89336-673-6

88. Räumlich differenzierte Quantifizierung der N- und P-Einträge in Grundwasser und Oberflächengewässer in Nordrhein-Westfalen unter besonderer Berücksichtigung diffuser landwirtschaftlicher Quellen

von F. Wendland et. al. (2010), xii, 216 Seiten

ISBN: 978-3-89336-674-3

89. Oxidationskinetik innovativer Kohlenstoffmaterialien hinsichtlich schwerer Lufteinbruchstörfälle in HTR's und Graphitentsorgung oder Aufarbeitung

von B. Schlögl (2010), ix, 117 Seiten

ISBN: 978-3-89336-676-7

90. Chemische Heißgasreinigung bei Biomassenvergasungsprozessen

von M. Stemmler (2010), xv. 196 Seiten

ISBN: 978-3-89336-678-1

91. Untersuchung und Optimierung der Serienverschaltung von Silizium-Dünnschicht-Solarmodulen

von S. Haas (2010), ii, 202 Seiten

ISBN: 978-3-89336-680-4

92. Non-invasive monitoring of water and solute fluxes in a cropped soil

by S. Garré (2010), xxiv, 133 pages

ISBN: 978-3-89336-681-1

93. Improved hydrogen sorption kinetics in wet ball milled Mg hydrides

by L. Meng (2011), II, 119 pages

ISBN: 978-3-89336-687-3

94. Materials for Advanced Power Engineering 2010

ed. by J. Lecomte-Beckers, Q. Contrepois, T. Beck and B. Kuhn (2010), 1327 pages

ISBN: 978-3-89336-685-9

95. 2D cross-hole MMR – Survey design and sensitivity analysis for crosshole applications of the magnetometric resistivity

by D. Fielitz (2011), xvi, 123 pages

ISBN: 978-3-89336-689-7

96. Untersuchungen zur Oberflächenspannung von Kohleschlacken unter Vergasungsbedingungen

von T. Melchior (2011), xvii, 270 Seiten

ISBN: 978-3-89336-690-3

97. Secondary Organic Aerosols: Chemical Aging, Hygroscopicity, and Cloud Droplet Activation

by A. Buchholz (2011), xiv, 134 pages

ISBN: 978-3-89336-691-0

98. Chrom-bezogene Degradation von Festoxid-Brennstoffzellen

von A. Neumann (2011), xvi, 218 Seiten

ISBN: 978-3-89336-692-7

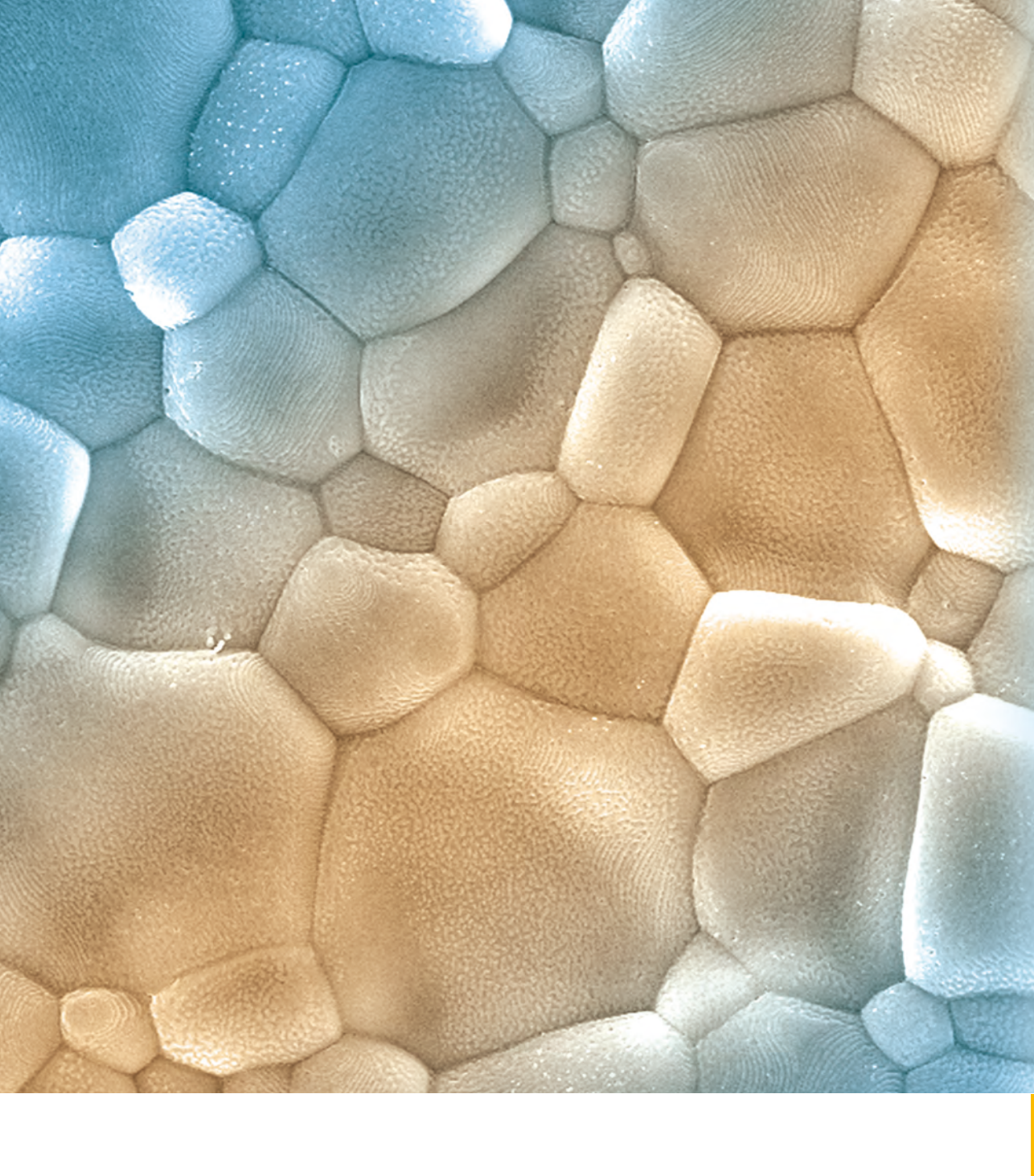
99. Amorphous and microcrystalline silicon applied in very thin tandem solar cells

by S. Schicho (2011), XII, 190 pages

ISBN: 978-3-89336-693-4

100. Sol-gel and nano-suspension electrolyte layers for high performance solid oxide fuel cells

by F. Han (2011), iv, 131 pages ISBN: 978-3-89336-694-1



Energie & Umwelt / Energy & Environment Band / Volume 100 ISBN 978-3-89336-694-1

